NASA TECHNICAL TRANSLATION NASA TT F-16,070

# COMPUTATION OF THREE-DIMENSIONAL FIELD OF MOTION IN CANALS AND BASINS USING HYDRODYNAMIC NUMERICAL METHODS

J. Sündermann

(NASA-TT-F-16070) COMPUTATION OF THREE DIMENSIONAL FIELD OF MOTION IN CANALS AND BASINS USING HYDRODYNAMIC NUMERICAL METHODS (Kanner (Leo) Associates) 95 p HC CSCL 20D G3/34 N75-13196 Unclas 04978

Translation of "Die hydrodynamisch-numerische Berechnung der Vertikalstruktur von Bewegungsvorgängen in Kanälen und Becken," Mitteilungen des Instituts für Meereskunde der Universität Hamburg, No. 19, Hamburg, Germany, October 1971, 97 pp

JAN 1975
RECEIVED
NASA STI FACILITY
INPUT BRANCH

Reproduced by
NATIONAL TECHNICAL INFORMATION SERVICE
US Department of Commerce
Springfield, VA. 22151

PRICES SUBJECT TO CHANGE

NATIONAL AERONAUTICS AND SPACE ADMINISTRATION
WASHINGTON, D.C. 20546 DECEMBER 1974

STANDARD TITLE PAGE

| | | |
|---|---|---|
| 1. Report No. NASA TT F-16,070 | 2. Government Accession No. | 3. Recipient's Catalog No. |
| 4. Title and Subtitle COMPUTATION OF THREE-DIMENSIONAL FIELD OF MOTION IN CANALS AND BASINS USING HYDRODYNAMIC NUMERICAL METHODS | | 5. Report Date December 1974 |
| | | 6. Performing Organization Code |
| 7. Author(s) J. Sündermann | | 8. Performing Organization Report No. |
| | | 10. Work Unit No. |
| 9. Performing Organization Name and Address Leo Kanner Associates Redwood City, California 94063 | | 11. Contract or Grant No. NASw-2481 |
| | | 13. Type of Report and Period Covered Translation |
| 12. Sponsoring Agency Name and Address National Aeronautics and Space Administration, Washington, D.C. 20546 | | 14. Sponsoring Agency Code |

15. Supplementary Notes

Translation of "Die hydrodynamisch-numerische Berechnung der Vertikalstruktur von Bewegungsvorgängen in Kanälen und Becken," Mitteilungen des Instituts für Meereskunde der Universität Hamburg, No. 19, Hamburg, Germany, October 1971, 97 pp

16. Abstract The treatment of hydrodynamic problems by numerical methods is extended to three dimensions. The models, based on the method of Hansen, can be used to obtain detailed information on the vertical structure of the velocity fields. The examples presented are restricted to wind-induced and tide-induced processes in schematic canals and basins, mostly of constant depth. For these relatively simple models, the numerical questions involved with extending the method to three dimensions can be seen very clearly. Two essential steps have been taken to make the models conform well to natural conditions: allowing for an arbitrary depth profile, and incorporating a boundary layer near the bottom.

| | | | |
|---|---|---|---|
| 17. Key Words (Selected by Author(s)) | 18. Distribution Statement Unclassified-Unlimited | | |
| 19. Security Classif. (of this report) Unclassified | 20. Security Classif. (of this page) Unclassified | 21. No. of Pages 93 | 22. Price |

NASA-HQ

TABLE OF CONTENTS


| | Page |
|---|---|
| I. Statement of Problem and Summary | 1 |
| II. Three-Dimensional Extension of the Hydrodynamic Numerical Method | 2 |
| 1. The Basic Hydrodynamic Equations | 2 |
| 2. The Two-Dimensional HN Method | 5 |
| 3. The Three-Dimensional HN Method | 15 |
| 3.1. The Foundations of the Three-Dimensional HN Model | 15 |
| 3.2. Canal of Constant Depth with Constant Vertical Spacing | 19 |
| 3.3. Canal of Constant Depth with Variable Spacing | 25 |
| 3.4. Canal of Variable Depth with Variable Vertical Spacing | 26 |
| 3.5. Basin of Constant Depth with Constant Vertical Spacing | 27 |
| 4. Explicit and Implicit Difference Methods. Numerical Stability | 30 |
| 4.1. Numerical Stability of Explicit Method with Constant Vertical Spacing | 30 |
| 4.2. Numerical Stability of Explicit Method with Variable Vertical Spacing | 42 |
| 4.3. An Implicit Difference Method | 44 |
| 4.4. Numerical Stability of the Implicit Method | 48 |
| 5. Simulation of a Boundary Layer Near the Bottom in the HN Model | 52 |
| III. Selected Examples | 56 |
| 1. Tides in Canal of Constant Depth | 56 |
| 2. Tide in Canal of Variable Depth | 58 |
| 3. Wind in Canal of Constant Depth | 65 |
| 4. Tide in Basin of Constant Depth | 68 |
| 5. Wind in Basin of Constant Depth | 71 |
| 6. Stability of the Explicit Method | 76 |
| 7. Comparison Between Explicit and Implicit Methods | 78 |
| 8. Vertical Profiles | 80 |
| IV. Concluding Remark | 89 |
| References | 91 |


PRECEDING PAGE BLANK NOT FILMED

# COMPUTATION OF THREE-DIMENSIONAL FIELD OF MOTION IN CANALS AND BASINS USING HYDRODYNAMIC NUMERICAL METHODS

Jürgen Sündermann

## I. Statement of Problem and Summary /1*

In the last two decades, hydrodynamic numerical methods have been increasingly employed in studies of motion processes not only in natural marine areas, rivers, and river mouths, but also in model basins and canals. One of the primary goals was to study first the horizontal component of the flows, which dominates due to the natural geometry. Accordingly, the mathematical models employed were generally based on the vertically integrated hydrodynamic differential equations. Machine capacity considerations also played a role in this decision. With the aid of such models, a large amount of fundamental new information in dynamic oceanography has been acquired since the ends of the '40s. The HN method developed by Hansen has contributed greatly to this effort.

Once it became evident that the two-dimensional methods were working well in practice, it became more and more desirable to include the vertical dimension as well -- which is very important for many marine processes -- in the mathematical models. Because of the rapid development of electronic computers as well, the present appears to be the right time to deal with more and more hydrodynamic problems in three-dimensional terms.

The present work makes a contribution to this development by generalizing the HN method worked out by Hansen for the three-dimensional treatment of motion processes in water. The relevant considerations are presented in Chapter II; once the spatial HN model has been constructed, particular attention is given to questions of numerical stability. In Chapter III, some selected examples are given for the application of the method developed here.

In many cases, the studies can be restricted to canal models with one horizontal and one vertical dimension, since the fundamental problems of the "vertical expansion" of the HN method can already be fully analyzed in these models as well. Extension to /2
genuinely spatial conditions with two horizontal dimensions is then chiefly a technical problem, and has also been undertaken.

---

* Numbers in the margin indicate pagination in the foreign text.

The results presented here assist in a numerical study of the vertical structure of motion processes in canals and basins. Of course, there must be a great deal more work in this field in order to match the three-dimensional HN models better to the natural situations, and in order to clarify the related mathematical questions.

I am indebted to Prof. W. Hansen for many useful suggestions and discussions. I would also like to thank R. Krautwald and S. Weiland for the careful preparation of the drawings.

## II. Three-Dimensional Extension of the Hydrodynamic Numerical Method /3

### 1. The Basic Hydrodynamic Equations

The starting point for all subsequent considerations is the set of general hydrodynamic differential equations, which, in cartesian form, read (see e.g. Sündermann [1]):

Equations of motion

$$\frac{\partial u}{\partial t} + u\frac{\partial u}{\partial x} + v\frac{\partial u}{\partial y} + w\frac{\partial u}{\partial z} - fv + \bar{f}w - A_H \Delta u - \frac{\partial}{\partial z} A_V \frac{\partial u}{\partial z} + \frac{1}{\rho}\frac{\partial p}{\partial x} = X \qquad (1.1)$$

$$\frac{\partial v}{\partial t} + u\frac{\partial v}{\partial x} + v\frac{\partial v}{\partial y} + w\frac{\partial v}{\partial z} + fu - A_H \Delta v - \frac{\partial}{\partial z} A_V \frac{\partial v}{\partial z} + \frac{1}{\rho}\frac{\partial p}{\partial y} = Y \qquad (1.2)$$

$$\frac{\partial w}{\partial t} + u\frac{\partial w}{\partial x} + v\frac{\partial w}{\partial y} + w\frac{\partial w}{\partial z} - \bar{f}u - A_H \Delta w - \frac{\partial}{\partial z} A_V \frac{\partial w}{\partial z} + \frac{1}{\rho}\frac{\partial p}{\partial z} = Z \qquad (1.3)$$

Continuity equation (for an incompressible medium)

$$\frac{\partial u}{\partial x} + \frac{\partial v}{\partial y} + \frac{\partial w}{\partial z} = 0 \qquad (1.4)$$

The cartesian coordinate system is to be oriented so that the x-axis points to the east, the y-axis to the north, and the z-axis vertically upward. The origin is located at unperturbed sea level (cf. Fig. 1). Additional definition:

| | |
|---|---|
| u, v, w | Components of flow velocity |
| p | Pressure |
| X, Y, Z | Components of external force (relative to unit of mass) |

| | |
|---|---|
| $\rho$ | Density |
| $A_H$, $A_V$ | Horizontal and vertical exchange coefficients |
| $f$, $\bar{f}$ | Coriolis parameter with $f = 2\omega\sin\phi$, $\bar{f} = 2\omega\cos\phi$ ($\omega$ = angular velocity of Earth) |
| $t$ | Time |
| $\Delta$ | Two-dimensional Laplace operator: $\Delta = \partial^2/\partial x^2 + \partial^2/\partial y^2$ |

These four equations describe the dynamics of the water. If the field of external forces is known, the oceanographic problem of determining the motion processes in the sea can be replaced by the equivalent mathematical problem, that of integrating the system of partial differential equations (1) with certain initial and boundary conditions. Mathematically, the problem can be solved, if the problem is properly formulated (in the sense of Courant-Hilbert [2]). /4

In general, the system (1) cannot be solved in analytic closed form because of its nonlinearity. In applications to motion processes in natural marine areas, the complicated geometry, which cannot be described analytically, presents a further obstacle. What can be done? First, in many practical cases, it is not at all necessary to take into account all terms of the system (1), since some of them are negligible. For instance, the following assumptions are often permissible (cf. e.g. Brettschneider [3]):

(1) The convective terms are negligibly small.

(2) The Coriolis terms with $\bar{f}$ are negligibly small.

(3) In the third equation of motion, the terms with $\partial w/\partial t$, $\Delta w$, and $\partial^2 w/\partial z^2$ can be dropped in comparison with the other terms.

(4) Horizontal exchange can be neglected.

(5) The vertical exchange coefficient is constant.

(6) The external forces X and Y are negligibly small, and $Z = -g$.

(7) $\rho = 1\,g/cm^3$.

Of course, the legitimacy of these assumptions must be verified in each individual case. If they are valid, then (1) acquires the following form:

$$\frac{\partial u}{\partial t} - fv - A_v \frac{\partial^2 u}{\partial z^2} + \frac{\partial p}{\partial x} = 0 \qquad (2.1)$$

$$\frac{\partial v}{\partial t} + fu - A_v \frac{\partial^2 v}{\partial z^2} + \frac{\partial p}{\partial y} = 0 \qquad (2.2)$$

$$\frac{\partial p}{\partial z} = -g \qquad (2.3)$$

/5

$$\frac{\partial u}{\partial x} + \frac{\partial v}{\partial y} + \frac{\partial w}{\partial z} = 0 \qquad (2.4)$$

For motions in horizontal, one-dimensional channels (rivers, canals), (2) simplifies, since in general no crosscurrents have to be taken into account, so that the x-axis can be placed along the axis of the canal without loss of generality. The motions are then described by the following system of equations:

$$\frac{\partial u}{\partial t} - A_v \frac{\partial^2 u}{\partial z^2} + \frac{\partial p}{\partial x} = 0 \qquad (3.1)$$

$$\frac{\partial p}{\partial z} = -g \qquad (3.2)$$

$$\frac{\partial u}{\partial x} + \frac{\partial w}{\partial z} = 0 \qquad (3.3)$$

Since the convective terms have been neglected, the systems (2) and (3) are quasi-linear; nevertheless, they can be substantially influenced by nonlinearities -- as will be found later in the vertical integration.

This circumstance, and the fact that the complicated geometrical structure of natural marine areas cannot be represented analytically require the use of numerical methods, but these are currently quite feasible due to the existence of electronic computers. These methods have the crucial advantage that in principle, any suitably formulated problem can be solved. However, there are also drawbacks, in particular:

(1) numerical difficulties not related to the problem appear;

(2) the deep understanding provided by analytical relations cannot be completely replaced by a large quantity of numerical values;

(3) frequently, a large amount of numerical data must be stored, and even the storage of electronic computers cannot cope with this information.

Therefore, in the historical development, horizontal motions /6
have been treated first in the overwhelming majority of cases. Because of the dimensions of natural formations, horizontal motions are generally the most important as well. In spite of the restriction to two-dimensional areas, many valuable results have been obtained and deep insights have been achieved into the internal dynamic relationships in this fashion. For many problems, considering just horizontal motions is completely sufficient.

## 2. The Two-Dimensional HN Method

The dimension is reduced by one by integrating the equations vertically. Instead of the velocity u and v, we use mean velocities $\bar{u}$ and $\bar{v}$, which at a point (x,y) apply for the entire vertical direction; vertical velocities are not calculated. The limits of integration are given by the actual surface $\zeta$ of the sea, i.e. the perturbation from the undisturbed level, and the bottom of the sea (Fig. 1). The mean horizontal velocities are then defined by

$$\bar{u} = \frac{1}{h+\zeta}\int_{-h}^{\zeta} u\,dz$$

$$\bar{v} = \frac{1}{h+\zeta}\int_{-h}^{\zeta} v\,dz$$

In the integration, the usual boundary-surface conditions (see e.g. [1]) are employed (S = surface, B = bottom):

(a)

$$\frac{\partial \zeta}{\partial t} + u_S \frac{\partial \zeta}{\partial x} + v_S \frac{\partial \zeta}{\partial y} - w_S = 0 \qquad (4.1)$$ /7

$$u_B \frac{\partial h}{\partial x} + v_B \frac{\partial h}{\partial y} + w_B = 0 \qquad (4.2)$$

(b) Newton-Taylor shear stress formulation

$$A_V \frac{\partial u}{\partial z}\Big|_B = \tau_B^{(x)} = r\sqrt{\bar{u}^2 + \bar{v}^2}\,\bar{u} \qquad (5.1)$$

$$\frac{\partial \bar{u}}{\partial t} + \frac{r}{h+\zeta}|\bar{u}|\,\bar{u} + g\frac{\partial \zeta}{\partial x} = \frac{\lambda}{h+\zeta}|U|\,U$$

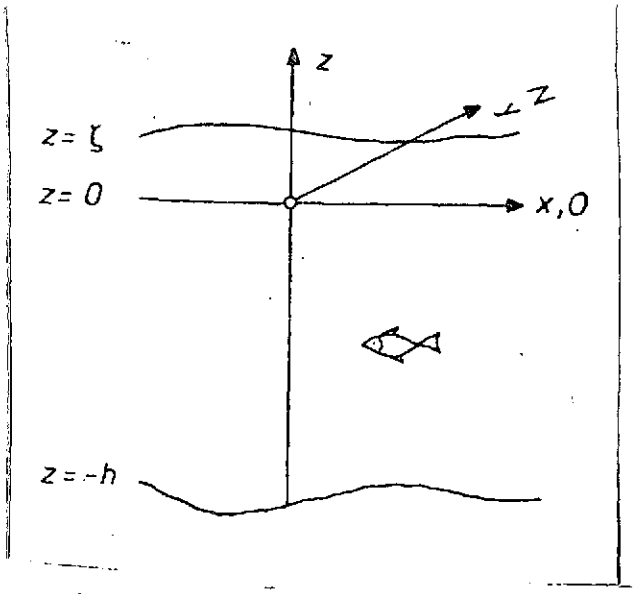


Fig. 1. Three-dimensional Cartesian coordinate system.

$$A_v \frac{\partial v}{\partial z}\Big|_B = \tau_B^{(y)} = r\sqrt{\bar{u}^2 + \bar{v}^2}\,\bar{v} \tag{5.2}$$

$$A_v \frac{\partial u}{\partial z}\Big|_S = \tau_S^{(x)} = \lambda\sqrt{U^2 + V^2}\,U \tag{5.3}$$

$$A_v \frac{\partial v}{\partial z}\Big|_S = \tau_S^{(y)} = \lambda\sqrt{U^2 + V^2}\,V \tag{5.4}$$

In these equations, $\tau^{(x)}$ and $\tau^{(y)}$ are the components of the shear stress vector at the boundary surfaces, and U and V are the components of the air velocity at the surface. r and λ are dimensionless constant friction parameters.

If it is further assumed that:

(c) $P_S$ = constant, and

(d)
$$\frac{1}{h+\zeta}(\bar{u} - u_{OL})\frac{\partial \zeta}{\partial t} \ll \frac{\partial \bar{u}}{\partial t}$$
$$\frac{1}{h+\zeta}(\bar{v} - v_{OL})\frac{\partial \zeta}{\partial t} \ll \frac{\partial \bar{v}}{\partial t}$$

which are often well satisfied (Hansen [4]), one obtains:

$$\frac{\partial \bar{u}}{\partial t} - f\bar{v} + \frac{r}{h+\zeta}\sqrt{\bar{u}^2+\bar{v}^2}\,\bar{u} + g\frac{\partial \zeta}{\partial x} = \frac{\lambda}{h+\zeta}\sqrt{U^2+V^2}\,U \tag{6.1}$$

$$\frac{\partial \bar{v}}{\partial t} + f\bar{u} + \frac{r}{h+\zeta}\sqrt{\bar{u}^2+\bar{v}^2}\,\bar{v} + g\frac{\partial \zeta}{\partial y} = \frac{\lambda}{h+\zeta}\sqrt{U^2+V^2}\,V \tag{6.2}$$

$$\frac{\partial \zeta}{\partial t} + \frac{\partial}{\partial x}\left((h+\zeta)\bar{u}\right) + \frac{\partial}{\partial y}\left((h+\zeta)\bar{v}\right) = 0 \tag{6.3.}$$

The system (3) can be integrated analogously to obtain:

(7.1)

$$\frac{\partial \zeta}{\partial t} + \frac{\partial}{\partial x}\left((h+\zeta)\bar{u}\right) = 0 \qquad (7.2)$$

The starting equations (6) and (7) have been utilized in numerous studies of the Hamburg Institute for Marine Science (IfM) and have worked very well. /8

To integrate (6) and (7), one must know the wind, the topography of the region (depth distribution, configuration of the coasts) and suitable initial and boundary conditions. In many cases, the boundary conditions can be formulated in the form (8):

(1) The normal component of the velocity at the coast is zero. (8.1)

(2) Water levels are prescribed at boundaries running through the open sea. (8.2)

The initial conditions can be chosen arbitrarily. In general, the system is presumed to be at rest at the outset:

$$u = v = 0; \quad \zeta = 0.$$

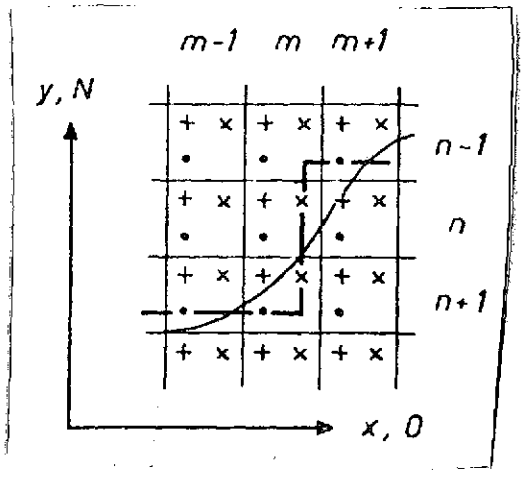


Fig. 2. Two-dimensional HN grid, after Hansen (with indexing). The smooth curve represents the natural coastline, and the heavy lines with right-angle corners is its approximation in the model. The symbols mean:
+ $\zeta$-computing point,
x u-computing point,
· v-computing point.

(see Hansen [5], Brettschneider [3], Sündermann [1], Röber [6]). In solving the systems (6) and (7) numerically, the hydrodynamic numerical (HN) method developed by Hansen [4], an explicit difference method, has worked particularly well. The method does not have to be discussed here in detail -- it has already been done in a number of works (Hanse [4], Fischer [7], Brettschneider [3], Sündermann [1]).

In the two-dimensional Cartesian case (i.e. a marine area very small in comparison with the surface of the Earth), which is to be investigated here, the HN method employs a rectangular grid, superimposed on the marine area to be studied (Fig. 2). The arrangement of the points at which water level and velocity components are calculated is that depicted in Fig. 2. This grid is particularly well suited to the

Fig. 3: $\zeta, u, v$ in space and time. After Hansen [5].

The differential equations associated with (6) are:

structure of the hydrodynamic differential equations. The spatial differential quotients in (6) can be represented very simply by using central differences. The boundary conditions (8) can be applied just as easily by having the schematic boundaries of the /9 mathematical models pass just through points at which u and v are calculated when the boundary is a coast, and through $\zeta$-points for open boundaries. The natural depths are likewise specified at u- and v-points. If the grid is chosen sufficiently fine, the numerical model can be largely matched to natural conditions.

Forward differences are employed to approximate the time derivatives. The numerical solution must be imagined as a finite collection of computing planes of the type shown in Fig. 2 at successive instance of time (Fig. 3). The mathematical model formulated in this way to simulate the natural motions in the sea is /10 is designated the hydrodynamic numerical (HN) model.

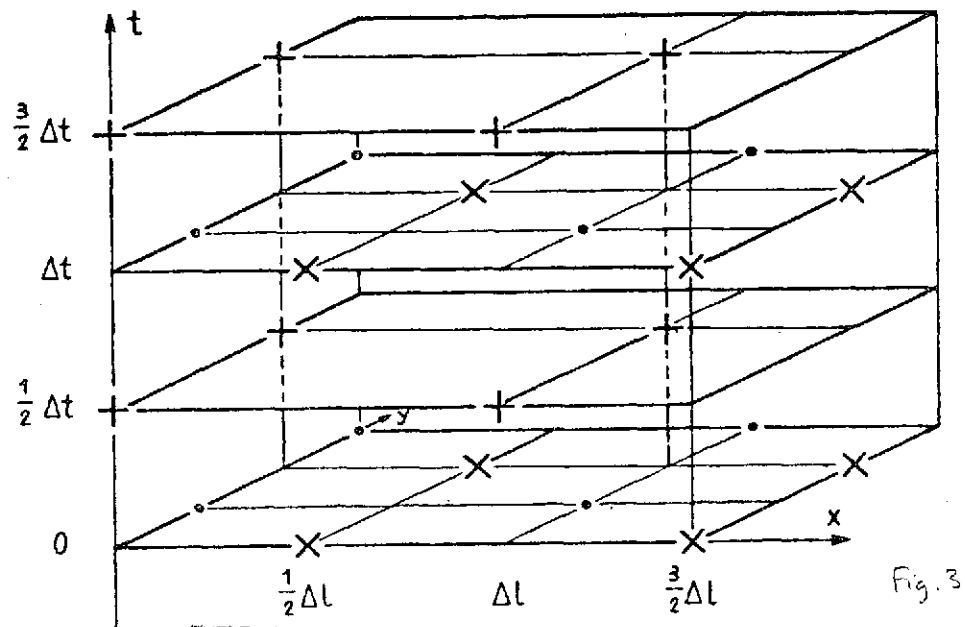


Fig. 3

Caption

Fig. 3. $\zeta, u, v$ in space and time. After Hansen [5].

The differential equations associated with (6) are:

The ....

$$\bar{u}^{(t+\Delta t)}(n,m) = \left(1 - \frac{\Delta t\, r}{H_u^{(t+\Delta t)}(n,m)} \sqrt{\bar{u}^{(t)2}(n,m) + \bar{\bar{v}}^{(t)2}(n,m)}\right) \bar{u}^{(t)}(n,m)$$

9.1

$$+ \Delta t f \bar{\bar{v}}^{(t)}(n,m) - \frac{\Delta t}{\Delta l} g \left(\zeta^{(t+\frac{\Delta t}{2})}(n,m+1) - \zeta^{(t+\frac{\Delta t}{2})}(n,m)\right) \qquad (9.1)$$

$$+ \frac{\Delta t\, l}{H_u^{(t+\Delta t)}(n,m)} \sqrt{U_u^{(t+\Delta t)2}(n,m) + V_u^{(t+\Delta t)2}(n,m)}\; U_u^{(t+\Delta t)}(n,m)$$

$$\bar{v}^{(t+\Delta t)}(n,m) = \left(1 - \frac{\Delta t\, r}{H_v^{(t+\Delta t)}(n,m)}\sqrt{\bar{\bar{u}}^{(t)\,2}(n,m) + \bar{v}^{(t)\,2}(n,m)}\right)\bar{v}^{(t)}(n,m) - \Delta t f\, \bar{\bar{u}}^{(t)}(n,m)$$
$$- \frac{\Delta t}{\Delta \ell} g\left(\zeta^{(t+\frac{\Delta t}{2})}(n-1,m) - \zeta^{(t+\frac{\Delta t}{2})}(n,m)\right) + \frac{\Delta t\, \lambda}{H_v^{(t+\Delta t)}(n,m)}\sqrt{U_v^{(t+\Delta t)\,2}(n,m) + V_v^{(t+\Delta t)\,2}(n,m)}\; V_v^{(t+\Delta t)}(n,m) \tag{9.2}$$

$$\zeta^{(t+\frac{\Delta t}{2})}(n,m) = \zeta^{(t-\frac{\Delta t}{2})}(n,m) - \frac{\Delta t}{\Delta \ell}\Big(H_u^{(t)}(n,m)\,\bar{u}^{(t)}(n,m) - H_u^{(t)}(n,m-1)\,\bar{u}^{(t)}(n,m-1)$$
$$+ H_v^{(t)}(n-1,m)\,\bar{v}^{(t)}(n-1,m) - H_v^{(t)}(n,m)\,\bar{v}^{(t)}(n,m)\Big) \tag{9.3}$$

with

$$H_u^{(t)}(n,m) = h_u(n,m) + \frac{1}{2}\left(\zeta^{(t-\frac{\Delta t}{2})}(n,m) + \zeta^{(t-\frac{\Delta t}{2})}(n,m+1)\right) \tag{10.1}$$

$$H_v^{(t)}(n,m) = h_v(n,m) + \frac{1}{2}\left(\zeta^{(t-\frac{\Delta t}{2})}(n,m) + \zeta^{(t-\frac{\Delta t}{2})}(n+1,m)\right) \tag{10.2}$$

$$\bar{\bar{u}}^{(t)}(n,m) = \frac{1}{4}\left(\bar{u}^{(t)}(n,m-1) + \bar{u}^{(t)}(n,m) + \bar{u}^{(t)}(n+1,m-1) + \bar{u}^{(t)}(n+1,m)\right) \tag{10.3}$$

$$\bar{\bar{v}}^{(t)}(n,m) = \frac{1}{4}\left(\bar{v}^{(t)}(n,m+1) + \bar{v}^{(t)}(n,m) + \bar{v}^{(t)}(n-1,m+1) + \bar{v}^{(t)}(n-1,m)\right) \tag{10.4}$$

In these equations, the following symbols are used:

| | |
|---|---|
| $h_u(n,m)$ | Constant natural depth at u-point (n,m) |
| $h_v(n,m)$ | Constant natural depth at v-point (n,m) (because of the structure of (6), it is not necessary to define the depth at $\zeta$-points) |
| $H_u(n,m)$ | Current depth of water at u-point (n,m) |
| $H_v(n,m)$ | Current depth of water at v-point (n,m) |
| $U_u$, $V_u$ | Components of vector of wind velocity at u-point /11 |
| $U_v$, $V_v$ | Components of vector of wind velocity at v-point |
| $\Delta t$ | Time increment |
| $\Delta \ell$ | Distance increment |

The equations in (10) are to be averaged arithmetically, since the unknowns are calculated at different points.

In difference forms, the boundary conditions (8) read:

$$\bar{u}(n,m) = 0 \text{ or } \bar{v}(n,m) = 0, \text{ if } (n,m) \in \text{boundary} \tag{11.1}$$

$$\zeta(n,m) = \zeta_0(n,m), \text{ if } (n,m) \in \text{boundary} \tag{11.2}$$

In the one-dimensional case, the method just explained must be merely restricted in an appropriate sense (Hansen [5], Rose [8], Ramming [9]). The differential equations then read (see (Fig. 4):

$$\bar{u}^{(t+\Delta t)}(m) = \left(1 - \frac{\Delta t\, r}{H_u^{(t+\Delta t)}(m)} \left|\bar{u}^{(t)}(m)\right|\right) \bar{u}^{(t)}(m) - \frac{\Delta t}{\Delta \ell} g\left(\zeta^{(t+\frac{\Delta t}{2})}(m+1) - \zeta^{(t+\frac{\Delta t}{2})}(m)\right) + \frac{\Delta t\, \lambda}{H_u^{(t+\Delta t)}(m)} \left|U_u^{(t+\Delta t)}(m)\right| U_u^{(t+\Delta t)}(m) \tag{12.1}$$

$$\zeta^{(t+\frac{\Delta t}{2})}(m) = \zeta^{(t-\frac{\Delta t}{2})}(m) - \frac{\Delta t}{\Delta \ell}\left(H_u^{(t)}(m)\, \bar{u}^{(t)}(m) - H_u^{(t)}(m-1)\, \bar{u}^{(t)}(m-1)\right) \tag{12.2}$$

with $$H_u^{(t)}(m) = h_u(m) + \frac{1}{2}\left(\zeta^{(t-\frac{\Delta t}{2})}(m) + \zeta^{(t-\frac{\Delta t}{2})}(m+1)\right).$$ /12

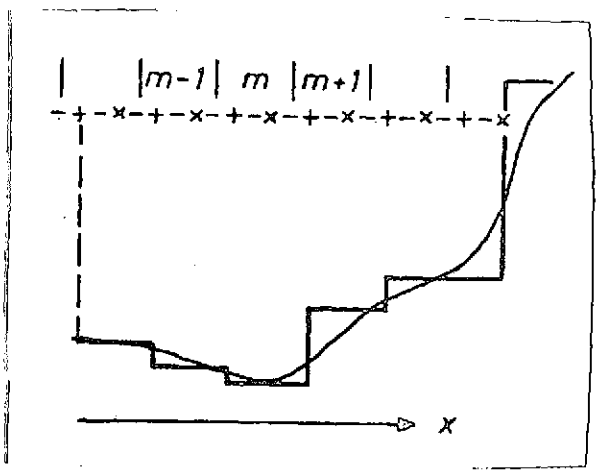


Fig. 4. One-dimensional HN grid, after Hansen (with indexing). The right-angled line is the model's approximation of the natural bottom profile.

Boundary conditions (11) can also be directly applied.

As previously mentioned, going over to a numerical method creates new problems, which originate in numerical aspects, i.e. in the closeness of a differential approximation or in the precision of a computer. Typical problems are whether

(1) the solution is numerically stable, or whether

(2) the numerical solution approximates the analytical one, and if so, how well.

These questions have been discussed many times for HN methods, and the reader should consult the relevant literature (Sündermann, Schmitz [10], Schäfer [11]).

These studies are based on the works of Courant, Friedrichs and Lewy [12], and Lax and Richtmyer [13], which give necessary and sufficient stability criteria for systems of linear differential equations. There is no complete theory for the present quasi-linear differential equations (6) and (7), but experience has shown that the criteria which can be derived for the associated systems of linear differential equations also work well in the quasi-linear case. The Courant-Friedrichs-Lewy (CFL) criterion in the case of (6) is:

$$\Delta t \leqq \frac{\Delta \ell}{\sqrt{2gh}} \tag{13.1}$$

and in the case of (7);

$$\Delta t \leqq \frac{\Delta \ell}{\sqrt{gh}} \tag{13.2}$$

These conditions are necessary, but not sufficient for stability. If (13) is not satisfied, sometimes even with too-strict approximations instabilities appear. In many cases (e.g. in the HN model of the North Sea), however, (13) has proved to be adequate. In general, one prerequisite is the occurrence of sufficiently large velocities and flat sea surfaces, which can nullify the kinetic energy of the water (and rounding errors as well) via bottom friction (cf. (5)). Experience has taught that if there are little motion and great depths, particularly with steep depth gradients, the numerical method is particularly vulnerable with respect to stability. In this case, it is convenient to introduce an artificial viscosity term, the so-called α-averaging, which is sufficient for stability according to Lax-Richtmyer [13] (cf. [1]).

Nevertheless, this method is problematic, since it changes the system of differential equations (6) and therefore describes a new physical situation. It seems more logical to work from the outset with a horizontal momentum transfer $A_H\Delta(u,v)$ in the sea (cf. Equations (1)), which, physically, smooths out the motion processes and is therefore suitable for cancelling out perturbations.[1] Hansen (personal communication) has expressed doubt about the necessity of horizontal momentum transfer for suppressing energy in the ocean (supported e.g. by the virtually undamped propagation of long waves across the entire Pacific demonstrated by Munk [14]), and considers energy dissipation in shelf regions to be crucial. However, because of the excessively large grid spacing, this can only be partially analyzed in many HN models.

[1] Incidentally, the difference approximation (10) has already undergone a smoothing, and this has a stabilizing effect.

The problem has not been conclusively resolved. However, we will not go into it further here. Later on, when the vertical dimension is included, new numerical questions will arise. At that point, the stability problem will be discussed in somewhat more detail.

Despite the vertically integrated equations, the HN method which has been sketched briefly here has worked well in a large number of specific studies on natural marine areas and mathematical /14 models (cf. [15]). Lastly, two further examples of the successful application of the method should be mentioned:

-- a tide calculation for the River Tyne (example A) and

-- a study of tide-induced waves in a canal, undertaken simultaneously with the HN method and a hydraulic model (example B).

Example A

This calculation was based on the IfM HN-model of the North Sea. Fig. 5, which was taken from [15], and which was derived from investigations of Brettschneider, shows the calculated tidal curve for the mouth of the River Tyne on the English coast (solid curve) for the period from October 13-20, 1965. As a comparison, values calculated with the aid of the classical harmonic method and other points derived from the English Admiralty Tables and from figures of Rossiter are also marked. As a whole, there is very good agreement. This becomes even more important when it is realized that this tide curve is just a small fractional result of the associated North Sea model, since tidal water levels and flows are calculated simultaneously at about 500 other points.

Example B

Tides in some simple one-dimensional canals (closed at one end, depth h = 15 m) were investigated [16]. Fig. 6 shows the calculated tidal range as a function of position for four canal models (16, 50, and 55 km long, and of different forms). For the two cases of the 55-km-long canal, the corresponding comparison values, obtained on the basis of measurements in the hydraulic model, are also drawn in. The discrepancies lie within the range of measuring accuracy. Finally, for the case of the 55-km-long straight canal, a comparison was undertaken at one point between the calculated and measured vertically averaged tidal flow velocities as a function of time. In this case as well, the qualitative and quantitative agreement is very good.

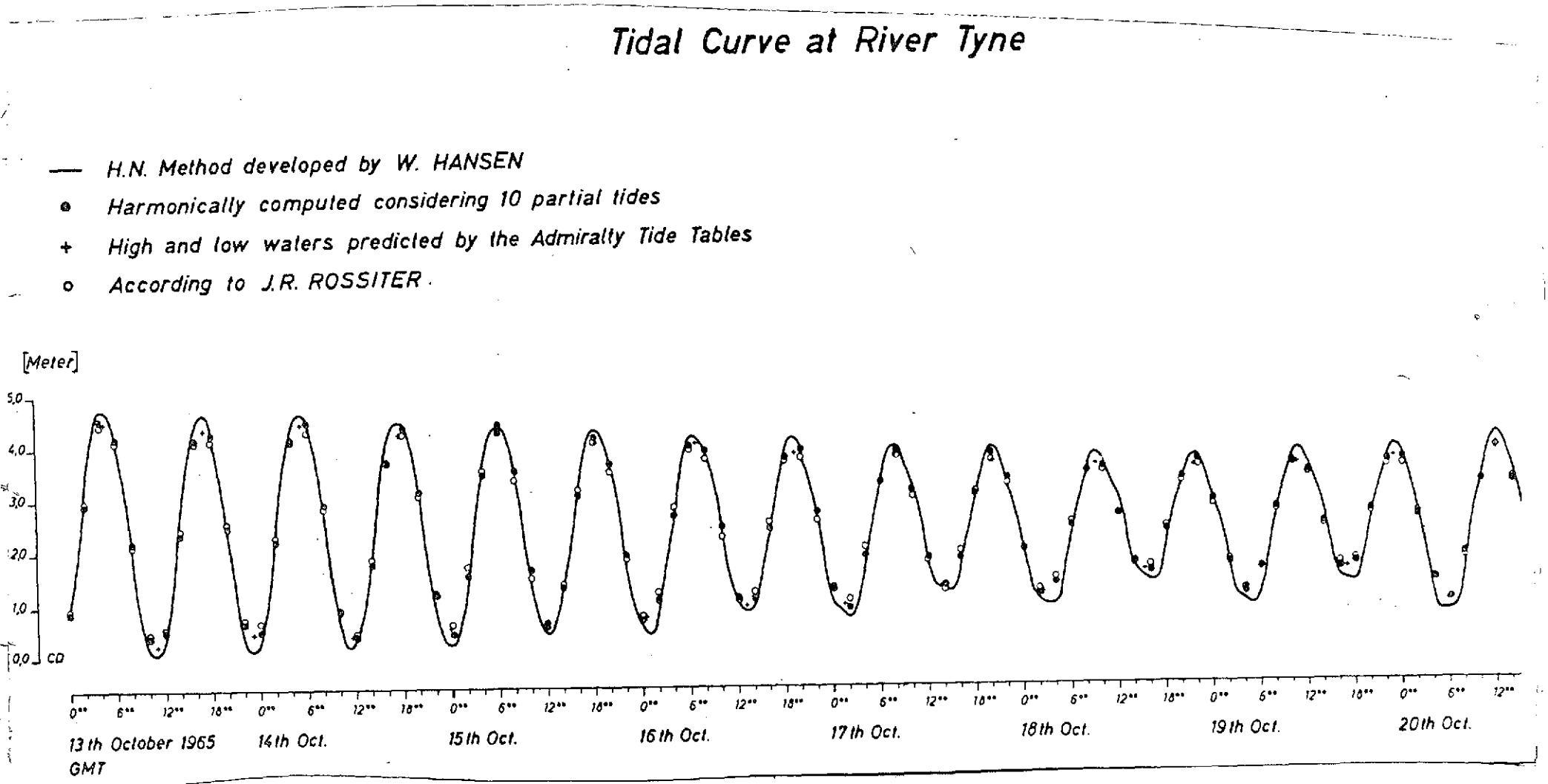


Fig. 5. Calculated tides in mouth of the River Tyne, along with comparison values, for the period October 13-20, 1965.

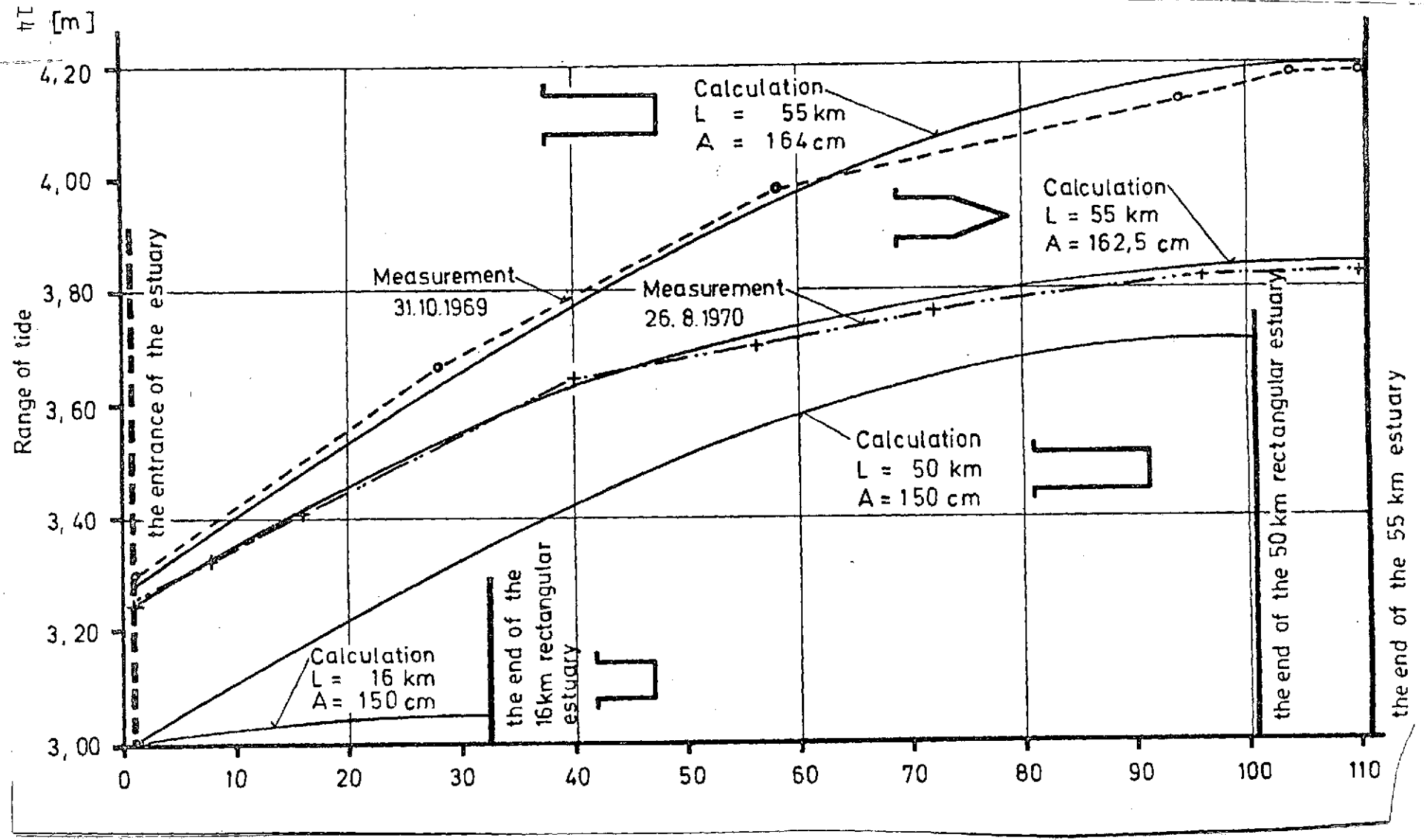


Fig. 6. Range of tide as function of distance from entrance for various simple canal models (h = 15 m). Comparison between HN calculation and measurement in hydraulic model (model scales: horizontal 1:1000, vertical 1:100).

/17

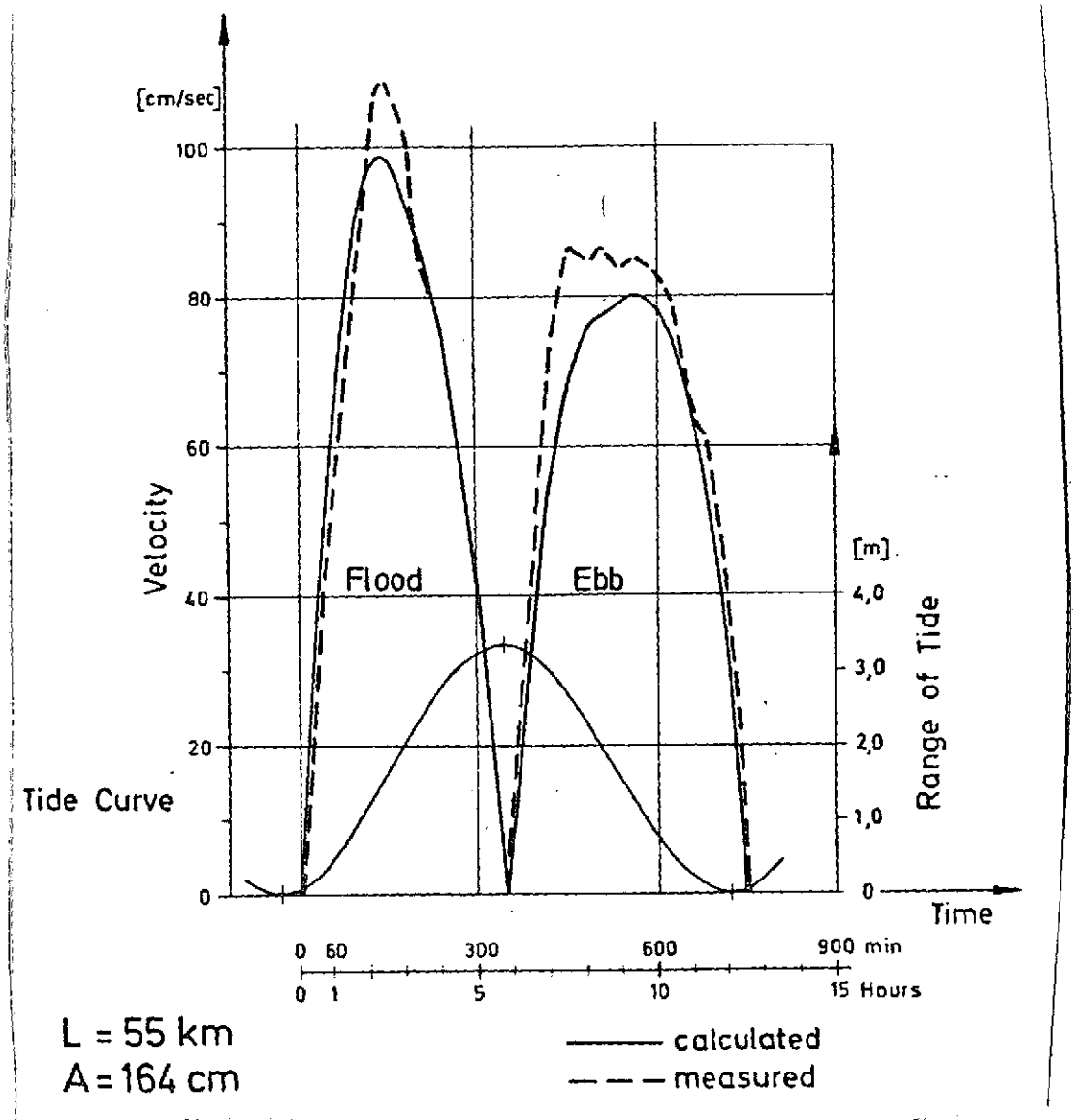


Fig. 7. Flood and ebb in a simple model canal ( (h = 15 m). Comparison between HN calculation and measurements in hydraulic model. In addition, the calculated tide curve is drawn in.

## 3. The Three-Dimensional HN Method /18

### 3.1. The Foundations of the Three-Dimensional HN Model

For the time being, we will base our treatment of the vertical structure of water motions on the Equations (3). The reason for this is economy of effort, in order to study the fundamental

questions at the outset in the simplest possible model. It will already be possible to recognize the most important problems, and perhaps to solve them. In this respect, we will already speak of a three-dimensional model, although the situation will be presumed to be homogeneous in one horizontal direction.

Equation (2) will be used for genuinely three-dimensional processes.

In addition to (3), the kinematic boundary conditions employed in the vertical integration also apply:

$$w_S = \frac{\partial \xi}{\partial x} u_S + \frac{\partial \xi}{\partial t} \tag{14.1}$$

$$w_B = -\frac{\partial h}{\partial x} u_B \tag{14.2}$$

With the aid of Equation (3.2), pressure gradients are replaced by water-level gradients. One can then use either of the two following systems to analyze the motion in the canal, depending on whether the vertical component w of the velocity is to be calculated or not:

$$\frac{\partial u}{\partial t} - A_v \frac{\partial^2 u}{\partial z^2} + g \frac{\partial \xi}{\partial x} = 0 \tag{15.1}$$

$$\frac{\partial \xi}{\partial t} + \frac{\partial}{\partial x} \int_{-h}^{\xi} u \, dz = 0 \tag{15.2}$$

$$\frac{\partial u}{\partial t} - A_v \frac{\partial^2 u}{\partial z^2} + g \frac{\partial \xi}{\partial x} = 0 \tag{16.1}$$

$$\frac{\partial \xi}{\partial t} + u_{cb} \frac{\partial \xi}{\partial x} - w_{ob} = 0 \tag{16.2}$$

$$\frac{\partial u}{\partial x} + \frac{\partial w}{\partial z} = 0 \tag{16.3}$$

These equations are supplemented by the boundary conditions: /19

(1) $A_v \partial u/\partial z|_S = \tau_S^{(x)}$ at the surface (see (5.3)) (17.1)

(2) For the horizontal component of velocity at the bottom, the following alternatives are considered:

(2a) $A_V \, \partial u/\partial z|_B = \tau_B^{(x)}$ (see (5.1)) (17.2)

(2b) $u_B = 0$ . (17.3)

(3) The normal component of the velocity at a fixed boundary is equal to zero (this applies to coasts and the bottom). (17.4)

(4) $\zeta = \zeta_0(t)$ at an open boundary. (17.5)

(5) $\partial\zeta/\partial x$ = const. at a closed boundary. (17.6)

Conditions (17.1), (17.4), and (17.5) are standard. Condition (17.3), i.e. adhesion to the bottom, is common in hydrodynamics, and is supported by numerous measurements (cf. e.g. Van Veen [17]); therefore, in the following investigations, this assumption is the one usually employed. On the other hand, condition (17.2) offers a chance to consider a non-zero flow at the bottom; its applicability has also been tested. Lastly, condition (17.6) is a way to approximate $\partial\zeta/\partial x$ at a boundary; it is only required if the equations are nonlinear.

The initial state is assumed to be stationary water:

$$u = w = 0; \quad \zeta = 0.$$

It seems logical to use the HN method designed by Hansen for the numerical treatment of the systems (15) and (16) and to appropriately generalize the difference method to include the vertical dimension. Central differences again suggest themselves for the spatial differential quotients in the z-direction. In approximating Equation (15.2) by finite expressions, an integral must now be numerically approximated.

It likewise seems logical to start from Hansen's successful arrangement of the calculating points (Figs. 2 and 4) in choosing a grid match to the system (2) and (15) or (16). These grids are now considered to be the uppermost calculating plane or line -- situated at the unperturbed sea level -- of a network expanded to include the vertical dimension. The network is composed of (not necessarily equidistant) computing planes or lines at various depths. In this case, u-points are always situated directly above u-points. The newly chosen w-points are located so that the Equations (16.2) and (16.3) can be approximated as simply as possible: namely, at the $\zeta$-points in the uppermost plane, and vertically below them in lower planes (cf. Fig. 8). /20

In contrast to the horizontal grid, variable spacing in the vertical direction must be considered from the very beginning. For one thing, available computer storage capacity does

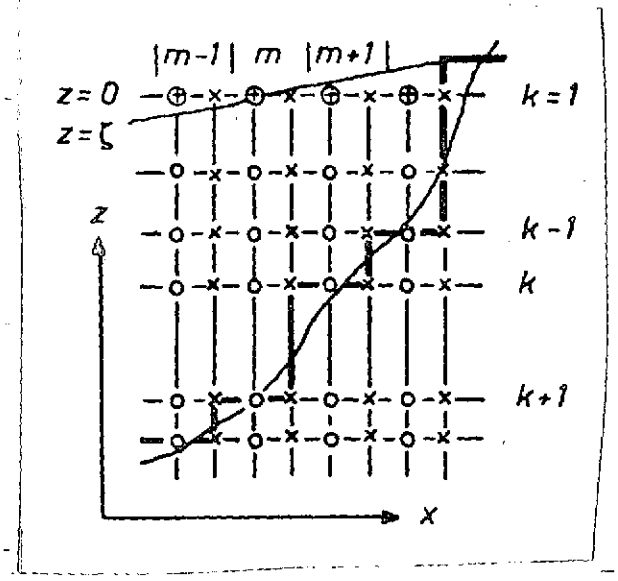


Fig. 8. x-z grid for the HN model of a canal with variable depth and variable vertical spacing. The polygonal boundary gives the model's approximation of the natural bottom profile. The indexing can also be seen in the diagram. The symbols employed are:
⊕ ζ- and w-point
o w-point
x u-point

not permit more than five or six computing planes in regions of the horizontal extent of the North Sea (25 x x 26 grid points with a spacing of $\Delta\ell$ = 37 km). Furthermore, experience (cf. [17]) has taught that the state of motion in the ocean is often practically homogeneous over rather great vertical distances, while on the other hand, substantial gradients can suddenly appear within relatively small spatial intervals (interfaces, boundary layers). In order to retain flexibility in adapting the method to the situation, /21 variable spacing has been incorporated into the analysis from the very beginning. Nevertheless, the first fundamental studies are based on equidistant computing planes.

Fig. 8 shows how the bottom on the coast is approximated within this grid. The polygonal boundary is situated so that the boundary conditions (17.3) and (17.4) can be applied as simply as possible. In later studies, the approximation of the bottom is still further improved.

In order to simplify the subsequent analysis, without substantially restricting its generality, the conditions are first assumed to be linear. System (15) is linearized by neglecting the water level $\zeta$ in comparison with the overall depth: $\zeta \ll h$. In place of Equation (15.2), consequently, the relation

$$\frac{\partial \zeta}{\partial t} + \frac{\partial}{\partial x}\int_{-h}^{0} u\, dz = 0 \qquad (18)$$

is employed, because it is particularly simple to approximate in difference form. The integral can be evaluated with the aid of the continuity equation (16.3) and the boundary condition (17.4). It is found that system (16) is linearized analogously to (18) by replacing Equation (16.2) by the relation

$$\frac{\partial \zeta}{\partial t} - w_0 = 0 \quad \text{with} \quad w_0 = w(z=0) \qquad (19)$$

The following analyses are based on the system (15.1, 18) or (16.1, 19, 16.3).

In order to check the effects of this linearization, Equations (15) and (16) are also used for some of the numerical examples given in Chapter III. The resulting differences were always small. Nevertheless, the corresponding difference equations will be given separately.

It should also be observed that in numerical meteorology, the vertical dimension is taken into account in similar fashion by introducing computing planes above one another. Nevertheless, because of the different boundary conditions, the situation is quite different in this case; therefore, the results from one case cannot be directly applied to the other.

## 3.2. Canal of Constant Depth with Constant Vertical Spacing /22

In this case, there are a total of $K - h/\Delta z + 1$ computing planes; the uppermost computing plane is at the undisturbed sea level, while the lowest is on the bottom (Fig. 9).

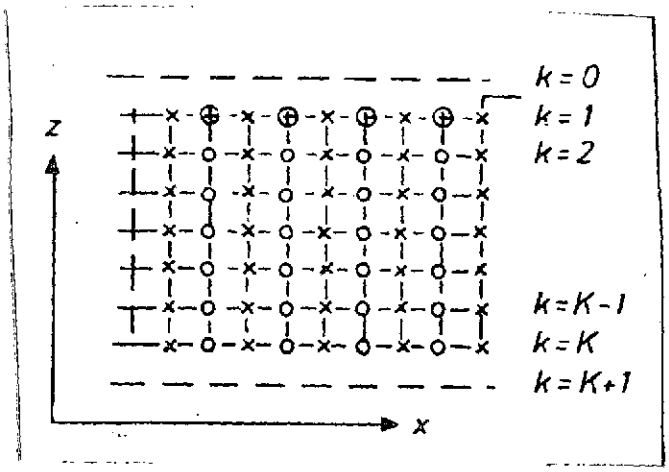


Fig. 9. x-z grid for HN model of a canal with constant depth using constant spacing $\Delta z$.

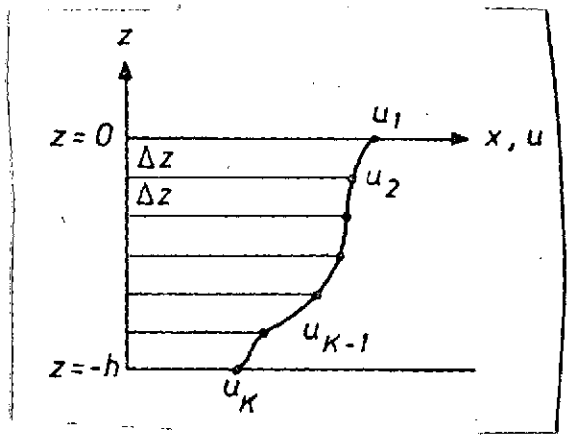


Fig. 10. Numerical intregration of $u(v)$.

The integral expression in (18) is most simply approximated by the trapezoidal rule (Fig. 10):

$$\int_{-h}^{0} u\,dz \approx \Delta z\left(\frac{u_1 + u_K}{2} + \sum_{k=2}^{K-1} u_k\right)$$

One then obtains the following differential equations: /23

(Without calculating w)

$$u^{(t+\Delta t)}(m,k) = u^{(t)}(m,k) + \frac{A_v\,\Delta t}{\Delta^2 z}\left(u^{(t)}(m,k-1) - 2u^{(t)}(m,k) + u^{(t)}(m,k+1)\right) - g\,\frac{\Delta t}{\Delta x}\left(\zeta^{(t+\frac{\Delta t}{2})}(m+1) - \zeta^{(t+\frac{\Delta t}{2})}(m)\right) \tag{20.1}$$

for $m = 1,\ldots,M;\ k = 1,\ldots,K$

$$\zeta^{(t+\frac{\Delta t}{2})}(m) = \zeta^{(t-\frac{\Delta t}{2})}(m) - \frac{\Delta t\,\Delta z}{\Delta x}\left(\frac{u^{(t)}(m,1)+u^{(t)}(m,K)}{2} + \sum_{k=2}^{K-1} u^{(t)}(m,k) - \frac{u^{(t)}(m-1,1)+u^{(t)}(m-1,K)}{2} + \sum_{k=2}^{K-1} u^{(t)}(m-1,k)\right) \tag{20.2}$$

for $m = 1,\ldots,M$ .

(calculating w)

$$u^{(t+\Delta t)}(m,k) = u^{(t)}(m,k) + \frac{A_v\,\Delta t}{\Delta^2 z}\left(u^{(t)}(m,k-1) - 2u^{(t)}(m,k) + u^{(t)}(m,k+1)\right) - g\,\frac{\Delta t}{\Delta x}\left(\zeta^{(t+\frac{\Delta t}{2})}(m+1) - \zeta^{(t+\frac{\Delta t}{2})}(m)\right) \tag{21.1}$$

for $m = 1,\ldots,M;\ k = 1,\ldots,K$

$$\zeta^{(t+\frac{\Delta t}{2})}(m) = \zeta^{(t-\frac{\Delta t}{2})}(m) + \Delta t\, w^{(t)}(m,1) \tag{21.2}$$

for $m = 1,\ldots,M$

$$w^{(t)}(m,k) = w^{(t)}(m,k+1) - \frac{\Delta z}{2\Delta x}\left(u^{(t)}(m,k) + u^{(t)}(m,k+1) - u^{(t)}(m-1,k) - u^{(t)}(m-1,k+1)\right) \tag{21.3}$$

for $m = 1,\ldots,M;\ k = 1,\ldots,K$ .

Two auxiliary planes $k = 0$ and $k = K + 1$ are introduced to assist in the finite approximation of the boundary conditions (17.1) and (17.2). These planes are at a distance $\Delta z$ above the

surface and below the bottom respectively. Then, using (5), we obtain

$$A_V \frac{u^{(t)}(m,c) - u^{(t)}(m-1)}{\Delta z} = \lambda \left| U^{(t)}(m) \right| U^{(t)}(m) \quad \text{for all m} \qquad (22.1)$$ /24

$$A_V \frac{u^{(t)}(m,K) - u^{(t)}(m,K+1)}{\Delta z} = r \left| u^{(t)}(m,K) \right| u^{(t)}(m,K) \quad \text{for all m} \qquad (22.2)$$

Instead of (22.2), the condition

$$u^{(t)}(m,K) = 0 \quad \text{for all m} \qquad (22.3)$$

is also reasonable. The remaining boundary conditions in (17) acquire the form:

$$u^{(t)}(m,k) = 0 \qquad (22.4)$$

if m designates a fixed boundary

$$w^{(t)}(m,k) = 0 \qquad (22.4)$$

$$\zeta^{(t)}(m) = \zeta_0^{(t)}(m), \qquad (22.5)$$

if m denotes an open boundary

$$\frac{\zeta^{(t)}(M+1) - \zeta^{(t)}(M-1)}{2\Delta x} = \frac{\zeta^{(t)}(M) - \zeta^{(t)}(M-1)}{\Delta x} \qquad (22.6)$$

if the canal is closed from the right and the last internal $\zeta$-point corresponds to M.

Equation (22.6) is modified appropriately for a model closed on the left.

With regard to these difference equations, the following points should be noted:

(1) In place of the difference approximation (22.1), one could also have chosen

$$A_V \frac{u^{(t)}(m,0) - u^{(t)}(m,2)}{2\,\Delta t} = \lambda \left| U^{(t)}(m) \right| U^{(t)}(m)$$

which, symmetrically, holds exactly for the surface, but does not use the value u(m,1). Comparison calculations have shown that the difference between the two forms of the approximation is small. /25

(2) Equation (22.2) differs from the expression in (5) in that the friction force at the bottom is assumed to be proportional not to the mean flow but to the flow velocity at the bottom. This is a better approximation of the natural situation to the extent that friction at the bottom can actually be directly correlated only with the flow in the vicinity of the bottom. Strictly speaking, the approach used in (5.1) and (5.2) for the case of vertically integrated equations can be justified physically only when an entire water column moves uniformly in a single direction. The successful application of (5) in numerous HN models indicates that the vertical profiles in Fig. 11a can frequently be used in the open sea. For tidal currents, this vertical structure has been established by numerous measurements [17, 18].

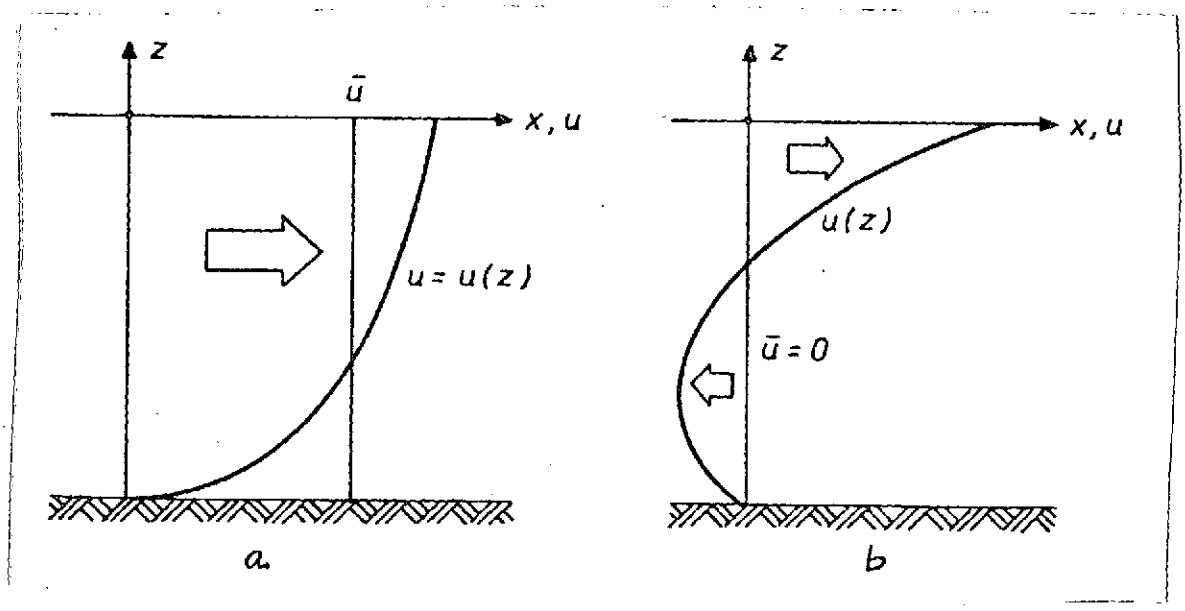


Fig. 11. Schematic vertical profiles for flow velocity in motion induced by (a) tides and (b) wind. In each case, ū denotes the value of u(z) averaged over the vertical direction.

For wind-induced motions, which can be generated in a relatively thin surface layer, the resulting profiles can take the form shown in Fig. 11b (cf. [19]). In these cases, (5) appears dubious, /26 since -- as shown in Fig. 11b -- the mean flow can be zero (so that there will be no friction at the bottom in the model), while the flow near the bottom is quite different from zero, thus losing energy via bottom friction. This deficiency of an HN model with integrated equations does not greatly affect the results, but the computing time is substantially increased, since the steady state is achieved relatively late due to the low bottom friction.

(3) If, as is frequently done, the zero-motion conditions (22.3) is used at the bottom, an empirical friction term of the form of (22.2) is no longer necessary. This case can be interpreted to mean that the energy loss at the bottom is so great that the velocity is retarded to zero.

(4) The difference approximation (21.1) presumes a constant vertical exchange coefficient: $A_V$ = const. This makes conditions homogeneous with respect to internal friction between adjacent water layers. This model still does not contain a boundary layer near the bottom with its important effects on the vertical velocity profile. Consequently, the calculated vertical profiles of velocity do not have the steep gradients near the bottom which may be considered typical of natural situations. However, this deficiency is of a rather technical nature, and is less vital as far as the immediate question, i.e. whether the HN method can be generalized at all in the proposed manner, is concerned. The model is extended in this direction in Section II.5.

(5) With regard to the computing procedure: first, the velocity component w is calculated -- from left to right and from the bottom up -- next the water level $\zeta$ -- from left to right ~~and~~ and then the velocity component u -- from left to right and from the top down.

next the

If one wishes to forego the linearization performed in (18) and (19), the HN model will be based on Equations (15.2) and /27 (16.2). For convenience, these are rewritten in the following forms:

$$\frac{\partial}{\partial x}\int_{-h}^{\zeta} u\,dz \approx \frac{\partial}{\partial x}\int_{-h}^{0} u\,dz + \frac{\partial}{\partial x}(u_s\,\zeta) .$$

This rep

This replacement is based on the mean value theorem of integration, and certainly will involve only minor errors as long as $|\zeta| \ll \Delta z$. Analogously:

$$
\begin{aligned}
u_s \frac{\partial \zeta}{\partial x} - w_s &= \frac{\partial}{\partial x}(u_s \zeta) - \frac{\partial u_s}{\partial x}\zeta - w_s \\
&\approx \frac{\partial}{\partial x}(u_s \zeta) + \left.\frac{\partial w}{\partial z}\right|_s \zeta - w_s \\
&\approx \frac{\partial}{\partial x}(u_s \zeta) - w_0 \quad .
\end{aligned}
$$

One then obtains for (15.2):

$$
\frac{\partial \zeta}{\partial t} + \frac{\partial}{\partial x}\int_{-h}^{0} u\,dz + \frac{\partial}{\partial x}(u_s \zeta) = 0 \tag{23}
$$

and for (16.2):

$$
\frac{\partial \zeta}{\partial t} - w_0 + \frac{\partial}{\partial x}(u_s \zeta) = 0 \tag{24}
$$

Then, for $|\zeta| \ll \Delta z$, the following difference equations are obtained:

$$
\begin{aligned}
\zeta^{(t+\frac{\Delta t}{2})}(m) = \zeta^{(t-\frac{\Delta t}{2})}(m) &- \frac{\Delta t \Delta z}{\Delta x}\Big(\frac{1}{2}\big(u^{(t)}(m,1) + u^{(t)}(m,K)\big) + \sum_{k=2}^{K-1} u^{(t)}(m,k) \\
&- \frac{1}{2}\big(u^{(t)}(m-1,1) + u^{(t)}(m-1,K)\big) - \sum_{k=2}^{K-1} u^{(t)}(m-1,k)\Big) \\
&- \frac{\Delta t}{2\Delta x}\Big(u^{(t)}(m,1)\big(\zeta^{(t-\frac{\Delta t}{2})}(m) + \zeta^{(t-\frac{\Delta t}{2})}(m+1)\big) - u^{(t)}(m-1,1)\big(\zeta^{(t-\frac{\Delta t}{2})}(m-1) + \zeta^{(t-\frac{\Delta t}{2})}(m)\big)\Big)
\end{aligned} \tag{25}
$$

or:

$$
\begin{aligned}
\zeta^{(t+\frac{\Delta t}{2})}(m) = \zeta^{(t-\frac{\Delta t}{2})}(m) &+ \Delta t\, w^{(t)}(m,1) \\
&- \frac{\Delta t}{2\Delta x}\Big(u^{(t)}(m,1)\big(\zeta^{(t-\frac{\Delta t}{2})}(m) + \zeta^{(t-\frac{\Delta t}{2})}(m+1)\big) - u^{(t)}(m-1,1)\big(\zeta^{(t-\frac{\Delta t}{2})}(m-1) + \zeta^{(t-\frac{\Delta t}{2})}(m)\big)\Big).
\end{aligned} \tag{26}
$$

If the condition $|\zeta| << \Delta z$ is violated, these difference equations must naturally be modified. However, for the cases treated here, Equations (25) and (26) are sufficient. /28

In the following, the special case "without calculating $\hat{w}$" is omitted. w will always be calculated. Naturally, there are no difficulties in applying the method to the first case.

## 3.3. Canal of Constant Depth with Variable Vertical Spacing

Initially, the variable vertical spacing is introduced for the case of a canal model with constant depth. The analysis which led to the derivation of the difference equations (20) and (21) can otherwise be appropriately applied.

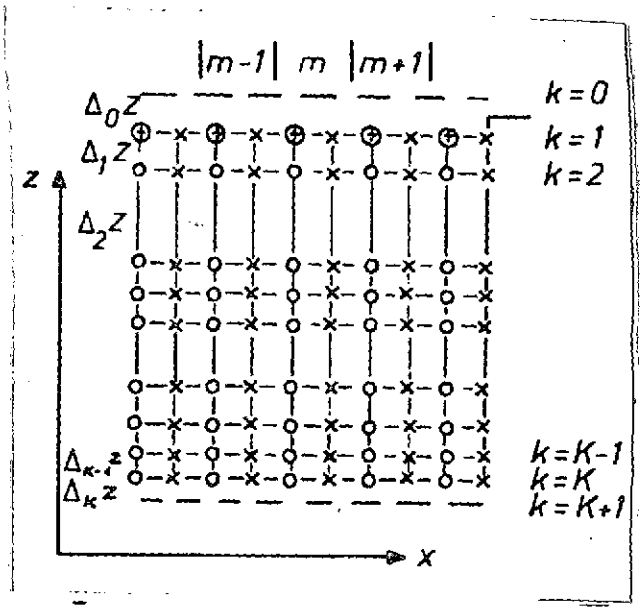


Fig. 12. x-z grid for the HN model of a canal with constant depth using variable spacing $\Delta_k z$.

Let the number of computing planes again be K, so that there are K - 1 (in general different) grid intervals $_k z$ (between the planes k and k + 1). Again, there are supplementary planes for k = 0 at a distance $\Delta_0 z = \Delta_1 z$ above the undisturbed surface, and for k = K + 1 at a distance $\Delta_K z = \Delta_{k-1} z$ below the bottom (Fig. 12). The difference equations analogous to (21) are now:

$$\overset{(t+\Delta t)}{u}(m,k) = \overset{(t)}{u}(m,k) + \frac{2A_v\,\Delta t}{\Delta_{k-1}z + \Delta_k z}\left(\frac{1}{\Delta_{k-1}z}\left(\overset{(t)}{u}(m,k-1) - \overset{(t)}{u}(m,k)\right) - \frac{1}{\Delta_k z}\left(\overset{(t)}{u}(m,k) - \overset{(t)}{u}(m,k+1)\right)\right) - g\frac{\Delta t}{\Delta x}\left(\overset{(t+\frac{\Delta t}{2})}{\zeta}(m+1) - \overset{(t+\frac{\Delta t}{2})}{\zeta}(m)\right) \quad (27.1)$$

$$\overset{(t+\frac{\Delta t}{2})}{\zeta}(m) = \overset{(t-\frac{\Delta t}{2})}{\zeta}(m) + \Delta t\, \overset{(t)}{w}(m,1) \quad (27.2)$$ /29

$$\overset{(t)}{w}(m,k) = \overset{(t)}{w}(m,k+1) - \frac{\Delta_k t}{2\Delta x}\left(\overset{(t)}{u}(m,k) + \overset{(t)}{u}(m,k+1) - \overset{(t)}{u}(m-1,k) - \overset{(t)}{u}(m-1,k+1)\right) \qquad (27.3)$$

Among the boundary conditions (22), only the relations (22.1) and (22.2) must be reformulated:

$$A_v \frac{\overset{(t)}{u}(m,0) - \overset{(t)}{u}(m,1)}{\Delta_1 t} = \lambda \left|\overset{(t)}{U}(m)\right| \overset{(t)}{U}(m) \qquad (28.1)$$

$$A_v \frac{\overset{(t)}{u}(m,K) - \overset{(t)}{u}(m,K+1)}{\Delta_{K-1} t} = r \left|\overset{(t)}{u}(m,K)\right| \overset{(t)}{u}(m,K) \qquad (28.2)$$

## 3.4. Canal of Variable Depth with Variable Vertical Spacing

Since the HN models are designed with a view toward practical applications, and since the crucial role of bottom topography is known precisely in shelf waters, a variable depth distribution must sooner or later be incorporated into the models. This can be done in three ways (cf. Fig. 13):

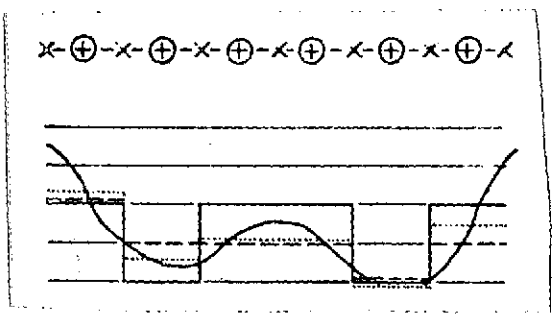

Fig. 13. Approximations of different accuracy to natural depth profile in the HN model, depending on whether the depth increments are (1) constant (solid line), (2) variable (but with quantized steps: broken line), or (3) variable (with arbitrary steps; dotted line).

(1) Fixed spacing and quantized depth increments of $k\Delta z$ ($k = 1, 2, \ldots$).

(2) Variable spacing $\Delta_k z$ and quantized depth increments

($k_1$, $k_2$ being two

grid planes.

(3) Variable grid spacing $\Delta_k z$ and variable depth increments.

Method (1) would be the three-dimensional generalization /30 of the two-dimensional HN method; in it too, the coast is generally approximated within a fixed grid. Because of the relatively low number of numerically practical vertical computing planes (computer capacity), method (1) is unsuitable for approximating real depth distributions. Method (2) is better only in special cases. Only with method (3) can natural situations be relatively closely

approximated. Therefore, the difference equations were derived for that method; it contains methods (1) and (2) as special cases.

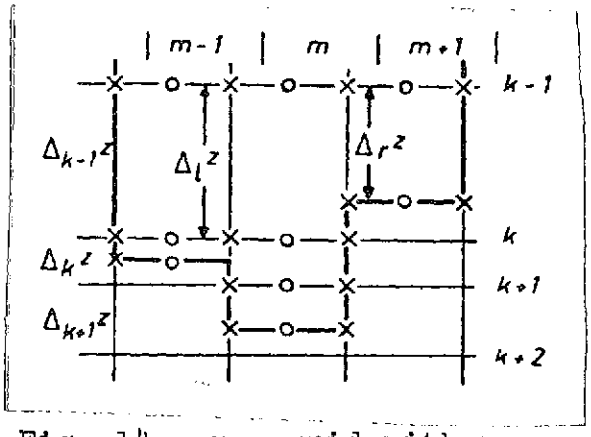


Fig. 14. x-z grid with variable spacing $\Delta_k z$ and arbitrary depth increments.

First, a system of vertical grid separations is chosen. However, this holds for a specific grid point on the horizontal line P(m) only until the bottom is reached. The lowest plane is always the bottom itself, even when there are still more planes in the system ($\Delta_k z$) (cf. Fig. 14). Changes in the system (27), which applies to models with constant depth, occur in the motion equation (27.1) and in particular in the continuity equation (27.3).

In the equation of motion, this is done whenever, for water less than $\Sigma\ \Delta_k z$ deep, fewer than K equations are to be considered, and the boundary conditions at the bottom must be applied to a plane $k < K$. In the continuity equation, it must be kept in mind that the volume elements of the grid now have different boundaries. If the height of the laterally open boundary of the lattice element (m,k-1/k) in Fig. 14 is denoted by $\Delta_\ell z$ on the left and $\Delta_r z$ on the right, the continuity equation now reads:

$$\boxed{\begin{aligned} w^{(t)}(m,k) = w^{(t)}(m,k+1) - \frac{1}{2\Delta x}\Big(&\big(u^{(t)}(m,k) + u^{(t)}(m,k+1)\big)\Delta_r z \\ &- \big(u^{(t)}(m-1,k) + u^{(t)}(m-1,k+1)\big)\Delta_\ell z\Big) . \end{aligned}} \qquad (29)$$

## 3.5. Basin of Constant Depth with Constant Vertical Spacing /31

The starting point is now the system (2) of equations. If, by analogy with the canal analysis, one wishes to calculate the water level $\zeta$ instead of the pressure p, it is convenient to employ the following linearized system:

$$\boxed{\frac{\partial u}{\partial t} - fv - A_v \frac{\partial^2 u}{\partial z^2} + g\frac{\partial \zeta}{\partial x} = 0} \qquad (30.1)$$

$$\frac{\partial v}{\partial t} + fu - A_v \frac{\partial^2 v}{\partial z^2} + g\frac{\partial \xi}{\partial y} = 0 \qquad (30.2)$$

$$\frac{\partial \xi}{\partial t} - w_0 = 0 \qquad (30.3)$$

$$\frac{\partial u}{\partial x} + \frac{\partial v}{\partial y} + \frac{\partial w}{\partial z} = 0 \qquad (30.4)$$

They are supplemented by the appropriately generalized boundary conditions (17).

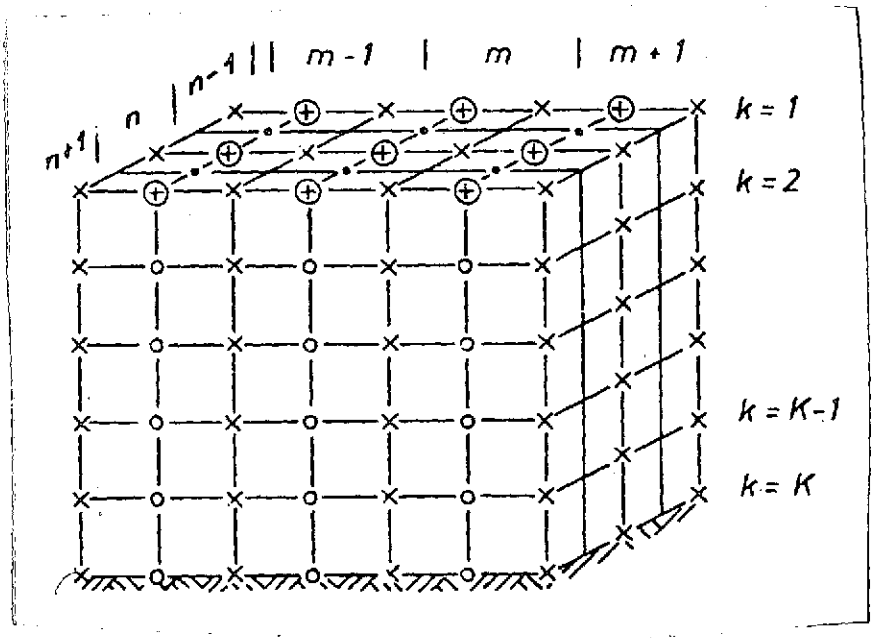


Fig. 15. Three-dimensional coordinate grid system for the HN model of a basin with constant depth and constant grid spacing. The following symbols are employed: ⊕ ζ- and w-point
o w-point
x u-point
· v-point

The structure of the grid matched to the system (30) is now derived by combining the horizontal and vertical networks shown in Fig. 2 and 8 (cf. Fig. 15). The difference equations associated with the system (30) now read: /32

$$
\begin{aligned}
u^{(t+\Delta t)}(n,m,k) = {} & u^{(t)}(n,m,k) + f\,\Delta t\,\bar{\bar{v}}^{(t)}(n,m,k) \\
& + \frac{A_V\,\Delta t}{\Delta^2 z}\left(u^{(t)}(n,m,k-1) - 2u^{(t)}(n,m,k) + u^{(t)}(n,m,k+1)\right) \\
& - g\,\frac{\Delta t}{\Delta \ell}\left(\zeta^{(t+\frac{\Delta t}{2})}(n,m+1) - \zeta^{(t+\frac{\Delta t}{2})}(n,m)\right)
\end{aligned}
\tag{31.1}
$$

$$
\begin{aligned}
v^{(t+\Delta t)}(n,m,k) = {} & v^{(t)}(n,m,k) - f\,\Delta t\,\bar{\bar{u}}^{(t)}(n,m,k) \\
& + \frac{A_V\,\Delta t}{\Delta^2 z}\left(v^{(t)}(n,m,k-1) - 2v^{(t)}(n,m,k) + v^{(t)}(n,m,k+1)\right) \\
& - g\,\frac{\Delta t}{\Delta \ell}\left(\zeta^{(t+\frac{\Delta t}{2})}(n,m) - \zeta^{(t+\frac{\Delta t}{2})}(n+1,m)\right)
\end{aligned}
\tag{31.2}
$$

$$
\zeta^{(t+\frac{\Delta t}{2})}(n,m) = \zeta^{(t-\frac{\Delta t}{2})}(n,m) + \Delta t\; w^{(t)}(n,m,1)
\tag{31.3}
$$

$$
\begin{aligned}
w^{(t)}(n,m,k) = {} & w^{(t)}(n,m,k+1) - \frac{\Delta z}{2\Delta \ell}\Big(u^{(t)}(n,m,k) + u^{(t)}(n,m,k+1) \\
& - u^{(t)}(n,m-1,k) - u^{(t)}(n,m-1,k+1) + v^{(t)}(n-1,m,k) \\
& + v^{(t)}(n-1,m,k+1) - v^{(t)}(n,m,k) - v^{(t)}(n,m,k+1)\Big)
\end{aligned}
\tag{31.4}
$$

with

$$
\begin{aligned}
\bar{\bar{u}}^{(t)}(n,m,k) &= \tfrac{1}{4}\left(u^{(t)}(n,m-1,k) + u^{(t)}(n,m,k) + u^{(t)}(n+1,m-1,k) + u^{(t)}(n+1,m,k)\right) \\
\bar{\bar{v}}^{(t)}(n,m,k) &= \tfrac{1}{4}\left(v^{(t)}(n-1,m,k) + v^{(t)}(n-1,m+1,k) + v^{(t)}(n,m,k) + v^{(t)}(n,m+1,k)\right).
\end{aligned}
$$

The boundary conditions are approximated by analogy with (22):

$$
\begin{aligned}
A_V\,\frac{u^{(t)}(n,m,0) - u^{(t)}(n,m,1)}{\Delta z} &= \lambda\sqrt{U_u^{(t)2}(n,m) + V_u^{(t)2}(n,m)}\;U_u^{(t)}(n,m) \\
A_V\,\frac{v^{(t)}(n,m,0) - v^{(t)}(n,m,1)}{\Delta z} &= \lambda\sqrt{U_v^{(t)2}(n,m) + V_v^{(t)2}(n,m)}\;V_v^{(t)}(n,m)
\end{aligned}
\tag{32.1}
$$

$$A_v \frac{u^{(t)}(n,m,K) - u^{(t)}(n,m,K+1)}{\Delta z} = r\sqrt{u^{(t)}(n,m,K)^2 + \bar{v}^{(t)}(n,m,K)^2}\; u^{(t)}(n,m,K)$$

$$A_v \frac{v^{(t)}(n,m,K) - v^{(t)}(n,m,K+1)}{\Delta z} = r\sqrt{\bar{u}^{(t)}(n,m,K)^2 + v^{(t)}(n,m,K)^2}\; v^{(t)}(n,m,K) \qquad (32.2)$$ /33

or

$$u^{(t)}(n,m,K) = v^{(t)}(n,m,K) = 0 \qquad (32.3)$$

$$u^{(t)}(n,m,k) = 0, \quad v^{(t)}(n,m,k) = 0, \qquad (3.24)$$

if (n,m,k) is situated on a fixed boundary

$$w^{(t)}(n,m,K) = 0 \qquad (32.4)$$

$$\zeta^{(t)}(n,m) = \zeta_0^{(t)}(n,m), \qquad (32.5)$$

if (n,m) is situated on an open boundary.

The three-dimensional equations can be generalized further, but this will not be done here.

## 4. Explicit and Implicit Difference Methods. Numerical Stability

### 4.1. Numerical Stability of Explicit Method with Constant Vertical Spacing

The difference equations including the vertical dimension have been formulated so far without taking the numerical stability of this approximation method into account. Initially, only the criterion (13) -- the CFL condition -- which regulates the relationship between the time increment and the horizontal distance increment, is known.

However, one would not anticipate that once the quantities $\Delta t$ and $\Delta x$ have been established, the vertical distance increment can be chosen arbitrarily. Instead, there will likely be a condition analogous to criterion (13). This will now be derived by means of an eigenvalue analysis, followed by a general discussion of stability on the basis of results found in the literature. /34

The starting point is the difference equation (20.1) with the boundary conditions (22.1) and (22.2); it will be found that the

special choice of boundary condition is not particularly significant for numerical stability, within certain limits. With the symbols

$$
\begin{aligned}
u_k &= u^{(t)}(m,k) \\
u'_k &= u^{(t+\Delta t)}(m,k) \\
a &= \frac{A_v \Delta t}{\Delta^2 t} \\
b_1 &= \frac{\Delta t}{\Delta t} \lambda \left| U^{(t)}(m) \right| U^{(t)}(m) - g \frac{\Delta t}{\Delta x} \left( \zeta^{(t+\frac{\Delta t}{2})}(m+1) - \zeta^{(t+\frac{\Delta t}{2})}(m) \right) \\
b_2 &= b_3 = \cdots = b_K = - g \frac{\Delta t}{\Delta x} \left( \zeta^{(t+\frac{\Delta t}{2})}(m+1) - \zeta^{(t+\frac{\Delta t}{2})}(m) \right) \\
b &= \frac{\Delta t}{\Delta t} r \left| u^{(t)}(m,k) \right|
\end{aligned}
$$

we obtain the system of equations

$$
\begin{aligned}
u'_1 &= (1-a)u_1 + au_2 + b_1 \\
u'_2 &= au_1 + (1-2a)u_2 + au_3 + b_2 \\
&- - - - - - - - - - - \\
u'_k &= au_{k-1} + (1-2a)u_k + au_{k+1} + b_k \\
&- - - - - - - - - - - \\
u'_{K-1} &= au_{K-2} + (1-2a)u_{K-1} + au_K + b_{K-1} \\
u'_K &= au_{K-1} + (1-a-b)u_K + b_K
\end{aligned}
$$

or, in matrix form,

$$
u' = \mathfrak{A} u + b \tag{33}
$$

In this case, u' is $(u_1', \ldots, u_K')$, expressed as a column vector, u is the column vector $(u_1, \ldots, u_K)$, and $b = (b_1, \ldots, b_K)$ is the column vector of inhomogeneities, i.e. the terms which do not contain the velocity u. Lastly, $\mathfrak{A}$ is the amplification matrix as defined by Richtmyer [20], which characterizes the special difference method. /35

For the concrete cases discussed here, a and b have the following orders of magnitude ($A_V = 10^3$ cm$^2$/sec, $\Delta\Delta t = 10^2$ sec, $\Delta z = 10^3$ cm, $r = 10^{-3}$, $|u| = 10$ cm/sec):

$$[a] = \left[\frac{A_v \Delta t}{\Delta^2 z}\right] = \frac{10^3 \quad 10^2}{10^6} = 10^{-1}$$

$$[b] = \left[\frac{\Delta t}{\Delta z} r |u|\right] = \frac{10^{-3} \cdot 10 \cdot 10^2}{10^3} = 10^{-3};$$

i.e. $b \ll a$. Therefore, in the following stability analysis, friction is ignored. Then the amplification matrix is

$$\mathfrak{A} = \begin{pmatrix} 1-a & a & & & & & \\ a & 1-2a & a & & & 0 & \\ & a & 1-2a & a & & & \\ & & & \cdot & & & \\ & & & & \cdot & & \\ & 0 & & & & \cdot & \\ & & & & a & 1-2a & a \\ & & & & & a & 1-a \end{pmatrix}_K$$

Here, K gives the number of rows and columns in the square matrix $\mathfrak{A}$. If (33) is viewed as an initial-value problem, the necessary criterion for stability of the interation process expressed by (33) is the von Neumann condition, according to which the absolute values of the eigenvalues $\lambda_i^{(k)}$ of $\mathfrak{A}$ must be bounded (cf. [20]):

$$|\lambda_i^{(k)}| \leqq 1 + 0(\Delta t) \qquad (i = 1, \ldots, K) \tag{34}$$

In the case where

for $0 < \Delta t < T$ and all grid points within the region; the function $O(\Delta t)$ denotes that the leftover term is at most a linear function of the time step.

In the case where the elements of $\mathfrak{A}$ are bounded, (34) can be sharpened to actually provide a sufficient condition for stability (cf. [20]): /36

$$\left| \begin{array}{ll} |\lambda_1^{(k)}| \leqq 1 + O(\Delta t) & \\ |\lambda_i^{(k)}| \leqq C < 1 & (i = 2, \ldots, K) \end{array} \right| \qquad (35)$$

This criterion is only applicable when a is bounded, i.e. in case the time step does not become arbitrarily large and the vertical distance step not arbitrarily small. Just this restriction shows that the spacing cannot be chosen arbitrarily in the explicit method.

In principle, the eigenvalues of the amplification matrix can be calculated in different ways. For instance, the simple makeup of the matrix permits an analytic solution of the system (33) in the form of a Fourier series, in which the eigenvalues are found directly.

However, this route will not be taken here, since it does not appear to be generalizable for the case of a more complicated structure of this matrix. To calculate the eigenvalues of the amplification matrix, we start from its characteristic equation:

$$D_k = |\mathfrak{a}_k - \lambda \mathfrak{E}| = \begin{vmatrix} 1-a-\lambda & a & & & \\ a & 1-2a-\lambda & a & & 0 \\ & & \ddots & & \\ 0 & & a & 1-2a-\lambda & a \\ & & & a & 1-a-\lambda \end{vmatrix}_k = 0 \qquad (36)$$

T <u>Claim</u>: The values $D_k$ are related by the recursion formula

$$\left| D_k = (1-2a-\lambda)\, D_{k-1} - a^2 D_{k-2} \right| \qquad (37)$$

Proof:

By adding the first column to the second in (36), we obtain

/37

$$\mathcal{D}_k = \begin{vmatrix} 1-a-\lambda & 1-\lambda & & & & \\ a & 1-a-\lambda & a & & 0 & \\ & a & 1-2a-\lambda & & & \\ & & & \ddots & & \\ & 0 & & & \ddots & \\ & & & a & 1-2a-\lambda & a \\ & & & & a & 1-a-\lambda \end{vmatrix}_k$$

Then, expanding along the first row yields:

$$\mathcal{D}_k = (1-a-\lambda)\,\mathcal{D}_{k-1} - (1-\lambda) \begin{vmatrix} a & a & & & & \\ & 1-2a-\lambda & a & & 0 & \\ & & \ddots & & & \\ & 0 & & \ddots & & \\ & & & a & 1-2a-\lambda & a \\ & & & & a & 1-a-\lambda \end{vmatrix}_{k-1}$$

The determinants on the right side differ only in the first column, and consequently can be added easily:

$$\mathcal{D}_k = (1-2a-\lambda)\,\mathcal{D}_{k-1} + \begin{vmatrix} -a^2 & a & & & & \\ a^2 & 1-2a-\lambda & a & & 0 & \\ & & \ddots & & & \\ & 0 & & \ddots & & \\ & & & a & 1-2a-\lambda & a \\ & & & & a & 1-a-\lambda \end{vmatrix}_{k-1}$$

By adding the first row to the second, and then expanding along the first column, we obtain (37).

Now, by repeated application of the recursion formula (37), the number of rows of the determinants on the right side can be reduced one by one:

$$\begin{aligned} D_k &= (1-2a-\lambda)\, D_{k-1} - a^2 D_{k-2} \\ &= (1-2a-\lambda)\left[(1-2a-\lambda)\, D_{k-2} - a^2 D_{k-3}\right] - a^2 D_{k-2} \\ &= \left[(1-2a-\lambda)^2 - a^2\right] D_{k-2} - (1-2a-\lambda)\, a^2 D_{k-3} \end{aligned}$$

and so forth.

Claim: The $(D_k)$ satisfy the recursion formula /38

$$\begin{aligned} D_k = {} & D_{k-q} \sum_{\nu=0}^{[\frac{q}{2}]} (-1)^\nu \binom{q-\nu}{\nu} (1-2a-\lambda)^{q-2\nu} a^{2\nu} \\ & - D_{k-q-1} \sum_{\nu=0}^{[\frac{q-1}{2}]} (-1)^\nu \binom{q-\nu-1}{\nu} (1-2a-\lambda)^{q-2\nu-1} a^{2(\nu+1)} \end{aligned} \tag{38}$$

for $q < k$.

As usual, $[x]$ denotes the largest integer less than or equal to $x$.

Proof: (by complete induction on $q$)

(1) Let $q = 1$. Then

$$D_k = D_{k-1}(1-2a-\lambda) - D_{k-2}\, a^2$$

in agreement with (37).

(2) For the induction, we now assume that (38) is correct. Then we must show:

$$\begin{aligned} D_k = {} & D_{k-q-1} \sum_{\nu=0}^{[\frac{q+1}{2}]} (-1)^\nu \binom{q+1-\nu}{\nu} (1-2a-\lambda)^{q+1-2\nu} a^{2\nu} \\ & - D_{k-q-2} \sum_{\nu=0}^{[\frac{q}{2}]} (-1)^\nu \binom{q-\nu}{\nu} (1-2a-\lambda)^{q-2\nu} a^{2(\nu+1)} \end{aligned}$$

By (37):

$$-a^2 D_{k-q-2} = D_{k-q} - (1-2a-\lambda)\, D_{k-q-1}$$

Substituting this above, we obtain:

$$\mathcal{D}_k = \mathcal{D}_{k-q-1} \sum_{v=0}^{\left[\frac{q+1}{2}\right]} (-1)^v \binom{q+1-v}{v} (1-2a-\lambda)^{q+1-2v} a^{2v}$$
$$- \mathcal{D}_{k-q-1} \sum_{v=0}^{\left[\frac{q}{2}\right]} (-1)^v \binom{q-v}{v} (1-2a-\lambda)^{q+1-2v} a^{2v}$$
$$+ \mathcal{D}_{k-q} \sum_{v=0}^{\left[\frac{q}{2}\right]} (-1)^v \binom{q-v}{v} (1-2a-\lambda)^{q-2v} a^{2v}$$

In the second sum, the upper limit of the sum can also be written [(q + 1)/2], since the binomial coefficient vanishes for $v \geqslant q/2$. Then, the two upper sums can be combined: /39

$$\mathcal{D}_k = \mathcal{D}_{k-q-1} \sum_{v=0}^{\left[\frac{q+1}{2}\right]} (-1)^v \left[\binom{q+1-v}{v} - \binom{q-v}{v}\right] (1-2a-\lambda)^{q+1-2v} a^{2v}$$
$$+ \mathcal{D}_{k-q} \sum_{v=0}^{\left[\frac{q}{2}\right]} (-1)^v \binom{q-v}{v} (1-2a-\lambda)^{q-2v} a^{2v} . \qquad (39)$$

The difference between the binomial coefficients in the first sum can be calculated as follows:

$$\binom{q+1-v}{v} - \binom{q-v}{v} = \frac{(q+1-v)!}{v!(q+1-2v)!} - \frac{(q-v)!}{v!(q-2v)!}$$
$$= \frac{(q-v)!\ v}{v!(q+1-2v)!} = \frac{(q-v)!}{(v-1)!(q-2v+1)!} = \binom{q-v}{v-1} .$$

This binomial coefficient vanishes for v = 0; consequently the lower limits of the sum in the first term of (39) can be raised by one:

$$\mathcal{D}_k = \mathcal{D}_{k-q-1} \sum_{v=1}^{[\frac{q+1}{2}]} (-1)^v \binom{q-v}{v-1} (1-2a-\lambda)^{q+1-2v} a^{2v}$$
$$+ \mathcal{D}_{k-q} \sum_{v=0}^{[\frac{q}{2}]} (-1)^v \binom{q-v}{v} (1-2a-\lambda)^{q-2v} a^{2v} .$$

If, in the first sum, the index is modified by replacing v by v - 1, the result is formula (38), which was presumed to be correct.

If q = k - 2 is substituted in (38), the determinants $D_1$ and $D_2$ appear on the right, and they can be calculated very easily by going back to the definition of $D_k$ in (36):

/40

$$\mathcal{D}_1 = 1 - \lambda$$

$$\mathcal{D}_2 = \begin{vmatrix} 1-a-\lambda & a \\ a & 1-a-\lambda \end{vmatrix} = (1-a-\lambda)^2 - a^2 = (1-\lambda)(1-2a-\lambda) .$$

Formula (38) finally yields

$$\mathcal{D}_k = (1-\lambda) \sum_{v=0}^{[\frac{k-1}{2}]} (-1)^v \binom{k-1-v}{v} (1-2a-\lambda)^{k-1-2v} a^{2v} . \qquad (40)$$

Using this formula, the characteristic equation of the amplification matrix $D_k = 0$ can be formulated for an arbitrary number k of computing planes in the vertical direction, so that the eigenvalues can then be calculated.

Equation (40) implies that one of the eigenvalues is always $\lambda_1 = 1$, which satisfies the first part of Condition (35).

The first six equations and their solutions are:

$$k = 1 : \quad 1 - \lambda = 0$$
$$\lambda_1 = 1$$

$$k = 2 : \quad (1-\lambda)(1-2a-\lambda) = 0$$
$$\lambda_1 = 1$$
$$\lambda_2 = 1 - 2a$$

$$k = 3: \quad (1-\lambda)\left[(1-2a-\lambda)^2 - a^2\right] = 0$$

$$\lambda_1 = 1$$
$$\lambda_2 = 1-a$$
$$\lambda_3 = 1-3a$$

$$k = 4: \quad (1-\lambda)\left[(1-2a-\lambda)^3 - 2(1-2a-\lambda)a^2\right] = 0$$

$$\lambda_1 = 1$$
$$\lambda_2 = 1-2a$$
$$\lambda_3 = 1-(2-\sqrt{2})a$$
$$\lambda_4 = 1-(2+\sqrt{2})a$$

/41

$$k = 5: \quad (1-\lambda)\left[(1-2a-\lambda)^4 - 3(1-2a-\lambda)^2a^2 + a^4\right] = 0$$

$$\lambda_1 = 1$$
$$\lambda_2 = 1-\frac{5-\sqrt{5}}{2}a$$
$$\lambda_3 = 1-\frac{5+\sqrt{5}}{2}a$$
$$\lambda_4 = 1-\frac{3-\sqrt{5}}{2}a$$
$$\lambda_5 = 1-\frac{3+\sqrt{5}}{2}a$$

$$k = 6: \quad (1-\lambda)\left[(1-2a-\lambda)^5 - 4(1-2a-\lambda)^3a^2 + 3(1-2a-\lambda)a^4\right] = 0$$

$$\lambda_1 = 1$$
$$\lambda_2 = 1-2a$$
$$\lambda_3 = 1-a$$
$$\lambda_4 = 1-3a$$
$$\lambda_5 = 1-(2+\sqrt{3})a$$
$$\lambda_6 = 1-(2-\sqrt{3})a$$

It can be seen that, at least for $k \leq 6$, the eigenvalues of can be represented as follows:

$$\lambda_1^{(k)} = 1 \tag{41}$$
$$\lambda_i^{(k)} = 1-\alpha_i^{(k)}a \quad \text{with} \quad \alpha_i > 0 \ (i=2,\ldots,k)$$

This calculation of the eigenvalues for models with up to six computing planes will suffice in this case, since more extensive analyses are not planned for the time being, because of the limits set by computer capacity. Moreover, it is not at all obvious that the eigenvalues up through k = 6 can be given explicitly. For k = 7, this is no longer possible even in this case; one would then have to resort to approximations.

From the sufficient condition (35) for the stability of the method, restrictions can now be derived on the magnitude of a, and thus on the relationship between the time step and the vertical distance step. Presumably, $\Delta t$ will already have been determined in accordance with (13), following the choice of a suitable horizontal distance increment $\Delta x$. Then, (41) and (35) yield /42

$$\boxed{\left| 1 - \alpha_i^{(k)} a \right| \leqq c < 1}$$

Since $\alpha_i^{(k)} \geq 0$, that results in the requirement

$$\boxed{\alpha_i^{(k)} a \leqq c' < 2}$$

and with $a = A_v \Delta t / \Delta^2 z$, the desired sufficient stability criterion is obtained

$$\boxed{\Delta^2 z \geqq c'' > \frac{1}{2} \alpha_{max}^{(k)} A_v \Delta t} \qquad (42)$$

Hence, the larger the time step and the greater the vertical momentum transfer, the greater the vertical distance increment should be. In contrast to the CFL criterion (13), according to which the time step and the horizontal distance increment are linearly related, the relationship in this case is quadratic: halving the vertical distance step means dividing the time step by four, in case $\Delta z$ and $\Delta t$ are chosen so that (42) is just satisfied.

Examples:

(A) We will consider motion in a canal with water h = 50 m deep. Let the horizontal distance step be $\Delta x$ = 8000 m. To what

restrictions are the time step and the vertical distance step subject in a six-plane model ($A_V = 0.1\ m^2/sec$)?

According to (13);

$$\Delta t \leq \frac{\Delta x}{\sqrt{gh}} = \frac{8000}{\sqrt{9.81 \cdot 50}}\ sec \approx 361\ sec.$$

For instance, if $\Delta t = 300$ sec, (13) will certainly be satisfied. The maximum $\alpha$ for $k = 6$ is then found for $i = 5$, with

$$\alpha = 2 + \sqrt{3}.$$

Hence

$$\Delta z^2 > \frac{1}{2}(2+\sqrt{3}) \cdot 0.1 \cdot 300$$

and

$$\Delta z > 7.48\ m.$$

Hence, the minimum grid spacing sufficient for numerical stability is in this case greater than 7.48 m. Therefore, /43
$\Delta z = 50/(6 - 1) = 10$ m resulting from equidistant separation is acceptable. We will return to this example in Chapter III.

(B) We again consider the canal in Example (A). Suppose that the time step $\Delta t$ has not been established using (13), but will be determined by (42) after the choice of $\Delta z$. What restrictions would then apply to $\Delta t$ for a 2-, 3-, ..., 6-plane model?

The answers are contained in Table 1.

To apply criterion (42), it is enough to know the maximum value $\alpha_{max}^{(k)}$ of the set $\{\alpha_i^{(k)}\}$; except for the case $\lambda = 1$, this value corresponds to the eigenvalue of greatest magnitude $|\lambda|_{max}^{(k)}$ of the amplification matrix. It is not necessary to know the other eigenvalues $\lambda_i^{(k)}$.

This raises the question of whether statements can be made about $|\lambda|_{max}^{(k)}$ even without breaking down the polynomial (40) into linear factors -- a process which will obviously give rise to

TABLE 1. VERTICAL SPACING AND MAXIMUM PERMISSIBLE TIME STEP IN AN EQUIDISTANT k-PLANE MODEL

| k | $\Delta z$ [m] | $\Delta t <$ [sec] |
|---|---|---|
| 2 | 50 | 25000 |
| 3 | 25 | 4167 |
| 4 | 16.7 | 1636 |
| 5 | 12.5 | 863 |
| 6 | 10 | 536 |

considerable difficulties in the general case for $k > 6$.

If the eigenvalues of greatest magnitude are plotted on a graph for the six known cases $k = 1, \ldots, k = 6$, the resulting pattern suggests that $|\lambda|_{max}^{(k)}$ converges to a limit $\lambda_0 > 0$ as $k \to \infty$ (cf. Fig. 16). As indicated by the diagram, this limit appears to be

$$\lambda_{max} = \lim_{k \to \infty} |\lambda|_{max}^{(k)} = 1 - 4a$$

This suggests the criterion /44

$$\Delta z^2 > 2 A_v \Delta t \tag{43}$$

for the general case of a k-plane model. This conjecture has been confirmed by analyses of Richtmyer (see [20], p. 17).

The existence of a universal stability criterion for models with arbitrarily many vertical computing planes is of great importance, since it eliminates the necessity of working with the characteristic equation (40) for each model, which can be difficult in particular cases. Nevertheless, the condition (43) -- as Fig. 16 shows -- is necessary only for the limiting case $k \to \infty$, and can be replaced by less restrictive conditions for models with relatively few computing planes. Therefore, in these cases, (e.g. for $k \leq 6$), the above "individual" stability criteria are preferable.

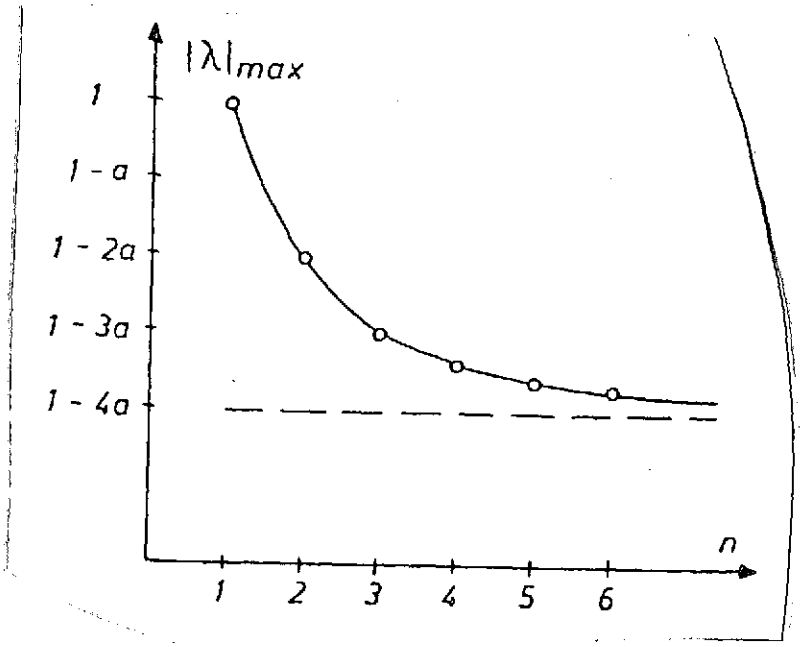


Fig. 16. The maximum eigenvalue of the amplification matrix as a function of the number of vertical computing planes. The broken line is the approximation curve.

## 4.2. Numerical Stability of Explicit Method with Variable Vertical Spacing /45

So far, the analyses of numerical stability have presumed constant vertical spacing. Adherence to criterion (42) will be assured even in the case of variable spacing whenever the smallest value $\lambda_{min^z}$ satisfies this condition.

We hypothesize that this condition is also necessary. We will not give the proof for the case of a general k-plane model; instead, the situation will be illustrated by an example for k = 3. In this case, the difference equations for u are:

$$u_1' = u_1 - \frac{A_V \Delta t}{\Delta_{1z}^2}(u_1 - u_2)$$

$$u_2' = u_2 + \frac{2A_V \Delta t}{h}\left(\frac{1}{\Delta_1 z}(u_1 - u_2) - \frac{1}{\Delta_2 z}(u_2 - u_3)\right)$$

$$u_3' = u_3 + \frac{A_V \Delta t}{\Delta_{2z}^2}(u_2 - u_3)$$

with

$$h = \Delta_1 z + \Delta_2 z$$

The eigenvalues of the associated amplification matrix are:

$$\lambda_1 = 1$$

$$\lambda_{2,3} = 1 - \frac{A_V \Delta t}{2\Delta_1^2 z \Delta_2^2 z}\left(h^2 \pm \sqrt{h^4 - 12\Delta_1^2 z \Delta_2^2 z}\right)$$

From the requirement $|\lambda_i| < 1$, we obtain the condition

$$\Delta_1 z \Delta_2 z > A_V \Delta t \sqrt{\frac{h^2}{2A_V \Delta t} - \frac{3}{4}} \tag{44.1}$$

For $\Delta_1 z = \Delta_2 z = \Delta z = h/2$, (44.1) leads to criterion (42) for the case $k = 3$:

$$\Delta^2 z > \frac{3}{2} A_V \Delta t \tag{44.2}$$

Assuming that in the equidistant case, the time step had been chosen so that this criterion, and thus (44.1), were satisfied: /46

$$\Delta^2 z > A_V \Delta t \sqrt{\frac{h^2}{2A_V \Delta t} - \frac{3}{4}} = C \tag{44.3}$$

Then any deviation from the equidistant configuration would act to the detriment of the inequality in (44.1). Namely, let

$$\Delta_1 z = \Delta z - \varepsilon$$

$$\Delta_2 z = \Delta z + \varepsilon \qquad (\varepsilon > 0)$$

According to (44.1), the following inequality must be satisfied:

$$\Delta^2 z - \varepsilon^2 = (\Delta z - \varepsilon)(\Delta z + \varepsilon) = \Delta_1 z \Delta_2 z > A_V \Delta t \sqrt{\frac{h^2}{2A_V \Delta t} - \frac{3}{4}} = C$$

However, (44.3) only says that

$$\Delta^2 z > C$$

Hence, for $\varepsilon \neq 0$, (44.1) is not in general satisfied, if the time step $\Delta t$ of the equidistant case (the spacing for which is obtained via the arithmetic mean: $\Delta z = (\Delta_1 z + \Delta_2 z)/2$) is to be retained.

If, on the other hand $\Delta t$ in (44.2) is chosen so that

$$\Delta^2_{min} z = \Delta_1^2 z = \Delta^2 z > \frac{3}{2} A_V \Delta t$$

then (44.1) is always satisfied:

$$\Delta_1 z \Delta_2 z = \Delta z(\Delta z + 2\varepsilon) = \Delta^2 z + 2\varepsilon\Delta z > C \;;$$

since, according to (44.3), it is already true that $\Delta^2 z > C$.

## 4.3. An Implicit Difference Method /47

The stability criterion (42) constitutes a major restriction in HN models for calculating the three-dimensional structure of motion processes. This may be illustrated by Example A on p.39. With a desired spacing of $\Delta x = 8$ km, it was found that the very reasonable time step of $\Delta t = 5$ min was allowed by the CFL condition. Then, by applying criterion (42), it was found that the vertical spacing had to satisfy

$$\Delta z > 7.48 \text{ m}.$$

If the water motion is subject to large variations in the vertical direction (e.g. near the bottom), such a large spacing must be viewed as far too big. Simulating e.g. boundary layers in the HN model makes it desirable that the distance steps $\Delta z$ here be in the decimeter or even in the centimeter range. However, even with water several meters deep, the necessary restriction to a small number of computing planes means that such spacing can no longer be achieved in the explicit HN method discussed so far, for reasons of numerical stability. This makes it necessary to design a numerical method which gets liberated from criterion (42) and which guarantees numerical stability for an arbitrary choice of the vertical distance step $\Delta z$.

This is now accomplished by going over to a partially implicit method, one proposed by W. Hansen, and used for the first time with great success for the vertical dimension in the present investigations.

The new method retains the explicit HN method for the horizontal dimension, since the necessary stability condition (13) has not proved to be a major restriction for the models considered here.

To calculate the vertical velocity profiles, on the other hand, an implicit procedure is induced by a new approximation of the vertical exchange term in the difference equations. To calculate the velocities in k vertical computing planes, this implicit method requires the solution of a k-dimensional system of equations for each grid point in the horizontal plane. /48

The new method will now be illustrated for the previous case in 3.2 (canal of constant depth with constant vertical spacing) and studied in more detail. Using Equations (16.1), 19, 16.3) as starting points, the only equation which will differ from those given in systems (20) and (21) is the equation of motion, inasmuch as the exchange term is approximated in a new way:

$$\text{(explicit)} \quad A_V \frac{\partial^2 u}{\partial x^2}\bigg|_t \approx \frac{A_V}{\Delta^2 z}\left(u^{(t)}(m,k-1) - 2u^{(t)}(m,k) + u^{(t)}(m,k+1)\right)$$

$$\text{(implicit)} \quad A_V \frac{\partial^2 u}{\partial x^2}\bigg|_t \approx \frac{A_V}{2\Delta^2 z}\left(u^{(t)}(m,k-1) - 2u^{(t)}(m,k) + u^{(t)}(m,k+1) + u^{(t+\Delta t)}(m,k-1) - 2u^{(t+\Delta t)}(m,k) + u^{(t+\Delta t)}(m,k+1)\right)$$

A time average of the values from two successive computing planes is used for the exchange term. in Richtmyer [20] or Forsythe-Wasow [21], one finds that such a procedure compels the method to be stable in many cases. Later on, this will be shown for a special case in our situation as well.

The implicit form analogous to the explicit difference equation (20.1) is now:

$$\begin{aligned} u^{(t+\Delta t)}(m,k) &= \frac{A_V \Delta t}{2\Delta^2 z}\left(u^{(t+\Delta t)}(m,k-1) - 2u^{(t+\Delta t)}(m,k) + u^{(t+\Delta t)}(m,k+1)\right) \\ &= u^{(t)}(m,k) + \frac{A_V \Delta t}{2\Delta^2 z}\left(u^{(t)}(m,k-1) - 2u^{(t)}(m,k) + u^{(t)}(m,k+1)\right) \\ &\quad - \frac{g\Delta t}{\Delta x}\left(\zeta^{(t+\frac{\Delta t}{2})}(m+1) - \zeta^{(t+\frac{\Delta t}{2})}(m)\right) \qquad \text{for } m = 1,\ldots,M;\ k = 1,\ldots,K. \end{aligned} \tag{45.1}$$

How can (45.1) be solved in practice? We introduce the following abbreviations:

$$u'_k = u(m,k)^{(t+\Delta t)}$$
$$u_k = u(m,k)^{(t)}$$
$$a = \frac{A_V \Delta t}{\Delta^2 z}$$
$$Z = g\frac{\Delta t}{\Delta x}\left(\zeta(m+1)^{(t+\frac{\Delta t}{2})} - \zeta(m)^{(t+\frac{\Delta t}{2})}\right)$$

Furthermore, we assume, without loss of generality, that the shear stresses at the surface and at the bottom can be neglected. Then, the following system of equations is obtained /49

$$\begin{aligned}
(1+\tfrac{a}{2})u'_1 \quad -\tfrac{a}{2}u'_2 \quad &= b_1 \\
-\tfrac{a}{2}u'_1 + (1+a)u'_2 - \tfrac{a}{2}u'_3 \quad &= b_2 \\
\cdot \quad \cdot \quad \cdot \quad & \\
-\tfrac{a}{2}u'_{K-2} + (1+a)u'_{K-1} \quad -\tfrac{a}{2}u'_K &= b_{K-1} \\
-\tfrac{a}{2}u'_{K-1} + (1+\tfrac{a}{2})u'_K &= b_K \quad .
\end{aligned} \tag{45.2}$$

In these equations, $b_1,\ldots,b_K$ are the corresponding right sides of the system (45.1):

$$\begin{aligned}
b_1 &= (1-\tfrac{a}{2})u_1 + \tfrac{a}{2}u_2 - Z \\
b_2 &= \tfrac{a}{2}u_1 + (1-a)u_2 + \tfrac{a}{2}u_3 - Z \\
&- \; - \; - \; - \; - \; - \; - \; - \\
b_{K-1} &= \tfrac{a}{2}u_{K-2} + (1-a)u_{K-1} + \tfrac{a}{2}u_K - Z \\
b_K &= \tfrac{a}{2}u_{K-1} + (1-\tfrac{a}{2})u_K - Z \quad .
\end{aligned}$$

The system (45.2) can be solved simply by the Gaussian algorithm. One begins with the last equation and derives a relation between two successive unknowns at each step. Arriving at the top, one finally obtains two equations for $u'_1$ and $u'_2$. From

them, $u_1'$ and $u_2'$ can be determined, then $u_3'$ and finally all other $u_k$. We will now give the appropriate recursion formulas.[2]

In general

$$u_k' = c_k\, u_{k-1}' + d_k \quad \text{for} \quad k = 2,\ldots,K\,. \tag{46.1}$$

In this equation: /50

$$c_K = \frac{a}{2}\left(1+\frac{a}{2}\right)^{-1}$$

$$c_{K-1} = \frac{a}{2}\left(1+a-\left(\frac{a}{2}\right)^2\left(1+\frac{a}{2}\right)^{-1}\right)^{-1}$$

$$- \quad - \quad - \quad - \quad - \quad - \quad - \quad - \quad -$$

and

$$d_K = \left(1+\frac{a}{2}\right)^{-1} b_K$$

$$d_{K-1} = \left(1+a-\left(\frac{a}{2}\right)^2\left(1+\frac{a}{2}\right)^{-1}\right)^{-1}\left(b_{K-1}+\frac{a}{2}\left(1+\frac{a}{2}\right)^{-1} b_K\right)$$

$$- \quad - \quad - \quad - \quad - \quad - \quad - \quad - \quad -$$

Summarizing, we obtain for the coefficients:

$$c_k = \frac{a}{2}\left(1+a-\frac{a}{2}c_{k+1}\right)^{-1} \qquad \text{for} \quad k = 2,\ldots,K \tag{46.2}$$

$$c_{K+1} = 1$$

$$d_k = c_k\left(\frac{2}{a}b_k+d_{k+1}\right) \qquad \text{for} \quad k = 2,\ldots,K \tag{46.3}$$

$$d_{K+1} = 0$$

[2] It is always assumed that the determinant of the system (45.2) is not equal to zero.

for $k = 2, \ldots, K$.

For $k = 2$, (46.1) and the first equation in (45.2) yield the system of equations

$$\boxed{\begin{aligned} -c_2 u_1' + u_2' &= d_2 \\ (1 + \tfrac{a}{2}) u_1' - \tfrac{a}{2} u_2' &= b_1 \end{aligned}}$$

and hence

$$\boxed{u_1' = \frac{\frac{a}{2} d_2 + b_1}{1 + \frac{a}{2} - \frac{a}{2} c_2}}$$

Now, successive $u_2', \ldots, u_K'$ can be calculated by (46.1) from top to bottom. /50

For the case 3.3 (canal of constant depth with variable vertical spacing), the corresponding result is

$$\boxed{\begin{aligned} u_k' &= c_k u_{k-1}' + d_k \qquad \left(a_k = \frac{A_V \Delta t}{\Delta_{k-1} z + \Delta_k z}\right) \\ c_k &= \frac{a_k}{\Delta_{k-1} z}\left(1 + a_k\left(\frac{1}{\Delta_{k-1} z} + \frac{1}{\Delta_k z}\right) - a_k \frac{c_{k+1}}{\Delta_k z}\right)^{-1}; \quad c_{K+1} = 1 \\ d_k &= c_k\left(\frac{\Delta_{k-1} z}{a_k} b_k + \frac{\Delta_{k-1} z}{\Delta_k z} d_{k+1}\right); \quad d_{K+1} = 0 \end{aligned}} \qquad (47)$$

for $k = 2, \ldots, K$.

## 4.4. Numerical Stability of the Implicit Method

No exhaustive stability analysis has yet been performed for the combined explicit/implicit method employed here (explicit horizontally, implicit vertically). On the other hand, numerous works have dealt separately with the stability of the explicit HN method (cf. [5, 3, 11]), and the stability of this implicit method (cf. [20, 21]).

For now, the main objects of interest are the properties of the implicit method characterized by (45). This method can be

assigned to the general class of implicit difference methods characterized by the system of equations

$$\frac{u_k^{(t+\Delta t)} - u_k^{(t)}}{\Delta t} = \sigma \frac{\theta(\delta^2 u)_k^{(t+\Delta t)} + (1-\theta)(\delta^2 u)_k^{(t)}}{\Delta^2 z}$$

with $\sigma$ = const $\geqslant 0$, $0 \leq \theta \leq 1$,

and

$$(\delta^2 u)_k^{(t)} = u_{k-1}^{(t)} - 2u_k^{(t)} + u_{k+1}^{(t)}$$

(cf. Richtmyer [20], p. 16). For $\theta = 0$, this yields the original explicit system while $\theta > 0$ gives an implicit method. The degree of stability of the system (45) depends on the choice of $\theta$. According to Richtmyer, the criterion is /52

$$\begin{aligned} &\frac{2\sigma\Delta t}{\Delta^2 z} \leqq \frac{1}{1-2\theta}, && \text{if } 0 \leq \theta < 1/2 \\ &\text{No restriction,} && \text{if } 1/2 \leq \theta \leq 1. \end{aligned} \qquad (48)$$

The case which will be used here, namely $\theta = 1/2$, which was studied for the first time by Crank and Nicolson [22] according to Forsythe and Wasow, and which has a particularly small approximation error, therefore results in a stable solution for any choice of $\Delta z$. For $\theta = 0$, observe that (48) yields the criterion (43).

Criterion (48) is valid only when the system has constant coefficients -- as in (45). Moreover, the boundary conditions must have a relatively simple form: they must be linear and homogeneous. Since, if the shear stress at the bottom is negligible (it was shown on p. 32 that this assumption is justified for the models discussed here), this requirement is satisfied for each of the boundary conditions (22.2) and (22.3), the special choice of the boundary conditions does not matter here as far as numerical stability is concerned.

In applying the combined explicit/implicit method, consequently, only the CSL condition (13) for the horizontal distance increment need be satisfied; there are no restrictions at all on the vertical distance increment. Numerical practice has shown that

the high stability of the implicit method used in the vertical direction obviously overflows into the horizontal direction as well: even if the CFL criterion is violated by a small amount, the solution remains stable.

We will now prove, for the example of a simple, three-plane model, that the implicit procedure just described is unconditionally stable. In accordance with (45.2), the fundamental homogeneous system of equations is:

$$\left|\begin{array}{l} (1+\frac{a}{2})u_1' - \frac{a}{2}u_2' = (1-\frac{a}{2})u_1 + \frac{a}{2}u_2 \\ -\frac{a}{2}u_1' + (1+a)u_2' - \frac{a}{2}u_3' = \frac{a}{2}u_1 + (1-a)u_2 + \frac{a}{2}u_3 \\ -\frac{a}{2}u_2' + (1+\frac{a}{2})u_3' = \frac{a}{2}u_2 + (1-\frac{a}{2})u_3 \end{array}\right| \quad (49)$$ /53

or in matrix form

$$\left|\begin{pmatrix} 1+\frac{a}{2} & -\frac{a}{2} & 0 \\ -\frac{a}{2} & 1+a & -\frac{a}{2} \\ 0 & -\frac{a}{2} & 1+\frac{a}{2} \end{pmatrix} = \begin{pmatrix} 1-\frac{a}{2} & \frac{a}{2} & 0 \\ \frac{a}{2} & 1-a & \frac{a}{2} \\ 0 & \frac{a}{2} & 1-\frac{a}{2} \end{pmatrix}\right|$$

[sic]

If the matrix on the left is denoted by $\mathfrak{A}$ [sic], and the matrix on the right by $\mathfrak{A}$, the matrix equation can be rewritten

$$\left| \mathfrak{A}' u' = - \mathfrak{A} u \right|$$

and the vector u' must be determined from this equation. This is simple to do formally:

$$\left| u' = \mathfrak{A}'^{-1} \mathfrak{A} u = \mathfrak{B} u \right|$$

The matrix $\mathfrak{B} = \mathfrak{A}'^{-1}\mathfrak{A}$ is the amplification matrix of the implicit system of equations (49). It is found to be

$$\mathcal{L} = \begin{pmatrix} \dfrac{1+a-\frac{a^2}{4}}{(1+\frac{a}{2})(1+\frac{3}{2}a)} & \dfrac{a}{1+\frac{3}{2}a} & \dfrac{a^2}{2(1+\frac{a}{2})(1+\frac{3}{2}a)} \\ \dfrac{a}{1+\frac{3}{2}a} & \dfrac{1-\frac{a}{2}}{1+\frac{3}{2}a} & \dfrac{a}{1+\frac{3}{2}a} \\ \dfrac{a^2}{2(1+\frac{a}{2})(1+\frac{3}{2}a)} & \dfrac{a}{1+\frac{3}{2}a} & \dfrac{1+a-\frac{a^2}{4}}{(1+\frac{a}{2})(1+\frac{3}{2}a)} \end{pmatrix}$$

The characteristic roots of $\mathcal{L}$ are:

$$\lambda_1 = 1$$

$$\lambda_2 = \frac{1-\frac{a}{2}}{1+\frac{a}{2}}$$

$$\lambda_3 = \frac{1-\frac{3}{2}a}{1+\frac{3}{2}a}$$

/54

Since $a > 0$, it follows that the eigenvalues $\lambda_i$ always satisfy the condition

$$|\lambda_1| = 1 \quad , \quad |\lambda_i| < 1 \qquad (i = 2,3)$$

for an arbitrary positive a. However, this means that the method is stable no matter how the vertical spacing is chosen.

Incidentally, one could have obtained a weaker result by not calculating the eigenvalues directly, but instead estimating them by the well-known Theorem of Frobenius (see e.g. [23]). According to this theorem, for a matrix $(b_{ik})$:

$$|\lambda| \leq \max_i \sum_{k=1}^{K} b_{ik}$$

In the present case, all three rows satisfy

$$|\lambda| \leq \sum_{k=1}^{3} |b_{ik}| = \frac{1 + 2a + \frac{3}{4}a^2}{1 + 2a + \frac{3}{4}a^2} = 1$$

However, this shows only that the necessary criterion (34) is satisfied.

## 5. Simulation of a Boundary Layer Near the Bottom in the HN Model

While suitable boundary conditions for lateral boundaries on the surface can easily be formulated to conform to natural situations, things are much more complicated at the bottom. However, the situation near the bottom plays a crucial role in determining the shape of the vertical velocity profiles. Fig. 11a depicts a typical profile, such as those found by Van Veen [17] by means of numerous tidal measurements off the Dutch coast. That curve can be represented analytically by the well-known empirical power law /55

$$u(z) = \sqrt[\alpha]{\frac{z + h}{h}}\, u_s \quad , \tag{50}$$

where Van Veen found $\alpha = 5$ to be the most favorable value. Characteristic features of this profile are that

-- from the surface to the bottom, the water flows essentially in the same direction,

-- the velocity is greatest at the surface,

-- the velocity right at the bottom is zero,

-- the velocity is practically constant over a long vertical distance (i.e. varies only slightly from a mean value u) and undergoes a steep drop only in the immediate vicinity of the bottom.

It was already mentioned previously that the boundary conditions (22.2) or (22.3) would not suffice by themselves to reproduce the measured profiles given in Fig. 11a in the HN model.

What is crucial is that this profile is obviously influenced strongly not only by the boundary conditionat the bottom, but also by the variations in vertical momentum transfer with depth. If the vertical exchange coefficient $A_V$ is assumed to be constant, -- as has been done so far -- the vertical exchange term can be written in the form employed in Equation (16.1):

$$A_V \frac{\partial^2 u}{\partial z^2} \tag{51.1}$$

This expression has a substantial influence on the vertical profile. If it is supposed that the system has reached a steady state, and that the horizontal gradients of water level are slight, this profile is described by the equation

/56

$$\frac{d^2 u}{dz^2} = 0$$

which corresponds to a linear rise of velocity from the bottom to the surface in the form

$$u(z) = c_1 z + c_2$$

where $c_1$ and $c_2$ areconstants. This means that the natural vertical profile of velocity given in Fig. 11a is not adequately approximated in general when (51.1) is employed. The more this term dominates the other term in the equation of motion (16.1), the greater the tendency toward a linear profile willbe. This result does not make any difference as far as the numerical behavior of the solution is concerned, but it is very important for practical considerations, since it makes the HN models designed so far appear somewhat unfit for applications.

How can theseHN models be improved? That is, how can they be better adapted to natural situations? In view of the above analysis, it seems logical to abandon the assumption of a constant vertical exchange coefficient and to represent the exchange term by the expression

$$\frac{\partial}{\partial z} \left(A_V \frac{\partial u}{\partial z}\right) \tag{51.2}$$

which can be derived directly from Newton's friction equation (cf. Sverdrup [24].

Now the difficult part is to find a suitable law to describe the vertical turbulent exchange $A_V$ as a function of depth. Numerical data on $A_V$ in the literature vary widely and depend heavily on the type of flow under investigation. Usually, just one value is given, intended to cover an entire range of depth (corresponding to $A_V$ = const). This order of magnitude is $10^3$ cm$^2$/sec (Sverdrup [24], p. 482). Sverdrup merely makes a rough qualitative statement about the vertical distribution of $A_V$, stating that near the bottom small values were measured throughout, while large values occurred at a great distance from the bottom. Kagan [25], who looked for a suitable expression for $A_V$ to use in analytical studies of three-dimensional motion, arrives at the law /57

$$A_V(z) = \begin{cases} A_V^*, & \text{if} \quad 0 \geqq z \geqq -h+d \\ \frac{z+h}{d} A_V^*, & \text{if} \quad -h+d \geqq z \geqq -h \end{cases} \qquad (52)$$

after a thorough study of the literature, in particular of the works of Boden [26], and after is own investigations. In (52), d is the thickness of a boundary layer near the bottom. This approach therefore keeps $A_V$ constant from the surface down to a point near the bottom, followed by a continuous transition to a linear drop to zero in a boundary layer near the bottom (Fig. 17). Two methods now suggest themselves for matching the HN model to the natural situation:

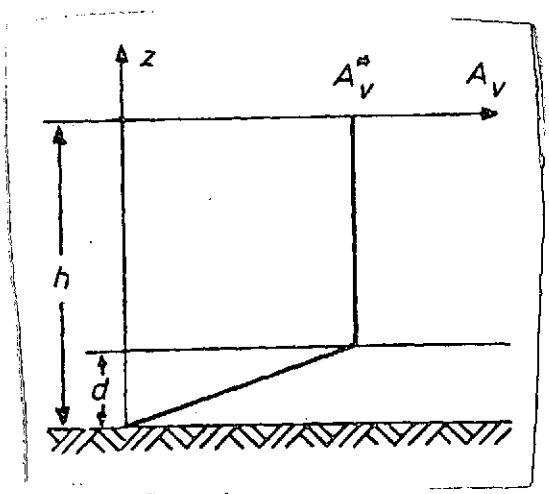

Fig. 17. $A_V(z)$ for a two-layer model with a linear drop near the bottom.

(1) The approach given in (52) is employed. Since the boundary layer near the bottom is very thin relative to the total depth, this can only be done by suitably refining the grid network near the bottom.

(2) A two-layer model is used, with a constant exchange coefficient $A_V^*$ above the boundary layer, and a smaller constant exchange coefficient $\bar{A}_V$ in the boundary layer.

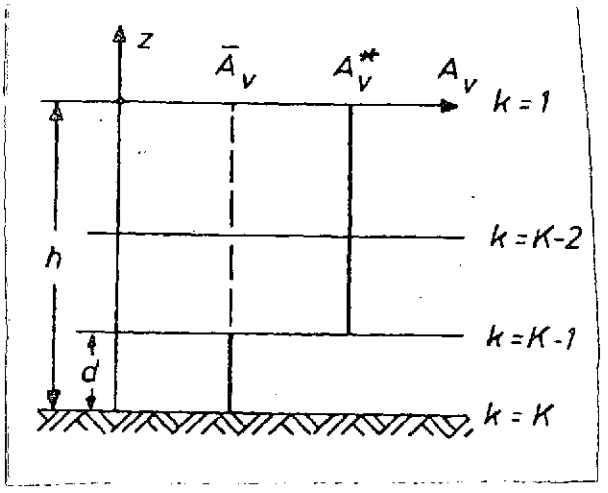


Fig. 18. $A_V(z)$ for a two-layer model with homogeneous conditions in each layer.

We will take alternative (2). Numerically, this case can be implemented by providing a boundary layer of thickness d as the lowest grid element in the vertical direction (Fig. 18). Now assuming that right at the bottom, the exchange term (51.2) dominates the other terms in the equation of motion (16.1) to such an extent that those other terms can be neglected (which appears legitimate for the boundary layer), and hence that the equation /58

$$\frac{\partial}{\partial z}\left(A_V \frac{\partial u}{\partial z}\right) = 0 \tag{53}$$

applies, we obtain an easily manipulated boundary-layer condition at the bottom. Namely, in difference form, (53) means that (cf. (27.1)):

$$\frac{2}{\Delta_{K-1}z+d}\left(A_V^* \frac{u_{K-2}-u_{K-1}}{\Delta_{K-1}z} - \bar{A}_V \frac{u_{K-1}-u_K}{d}\right) = 0$$

If, in line with boundary condition (22.3), we suppose that there is no motion at the bottom, $u_K = 0$. We then obtain the relationship:

$$u_{K-2} = \left(1 + \frac{\bar{A}_V \Delta_{K-1}z}{A_V^* d}\right) u_{K-1}$$

or

$$u_{K-2} = (1 + \varkappa)\, u_{K-1} \quad \text{with} \quad \varkappa = \frac{\bar{A}_V \Delta_{K-1}z}{A_V^* d}. \tag{54}$$

Introducing this condition (54) makes it simple to simulate the boundary layer near the bottom in the HN model. The quantity $\varkappa$ is a dimensionless parameter which can be varied in conformity with the model until sufficient agreement is attained /59

between the calculated and measured vertical profiles of velocity. In this way, the difficulties involved in a quantitative determination of $x$ on the basis of measurements of vertical exchange in boundary layers are avoided. The parameterization presented here was already noticed by Kagan [25].

If, in line with boundary condition (22b2), motion is permitted at the bottom, a boundary-layer condition analogous to (54) can be derived.

## III. Selected Examples

### 1. Tides in Canal of Constant Depth

Example 1:

The $M_2$ tide is studied in a simple canal model of constant depth (92 km long, 50 m deep). The grid employed can be seen in Fig. 19 (cf. Fig. 9). With a horizontal spacing of $\Delta x = 8$ km /60
and a constant vertical increment of $\Delta z = 10$ m, there are 11 internal $\zeta$-points and six computing planes in the vertical direction, the plane $k = 1$ coincided with the undisturbed surface, and plane $k = 6$ with the bottom. The tide is given as a sinusoidal wave at $\zeta$-point 13 with an amplitude of $A = 100$ cm. The time step is $\Delta t = 5$ min and the exchange coefficient is constant: $A_V = 10^3$ cm$^2$/sec.

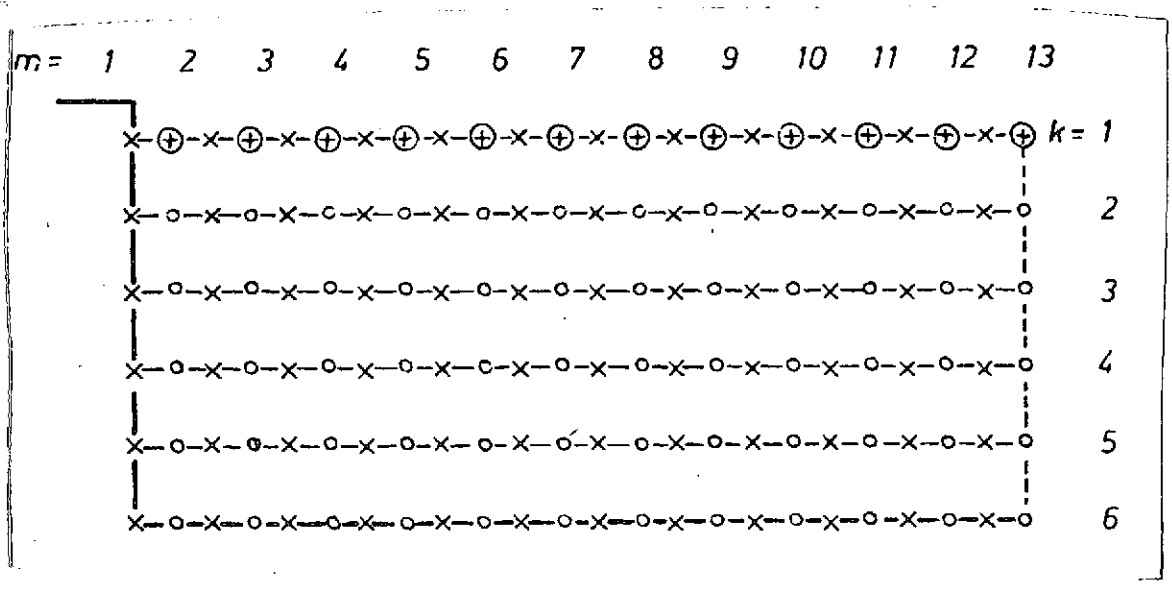


Fig. 19. x-z grid of the model canal ($\ell = 92$ km, $h = 50$ m).

After four periods, the calculation is practically stationary, i.e. the water level changes by less than 1 mm from one period to the next, and the velocities by less than 1 mm/sec.

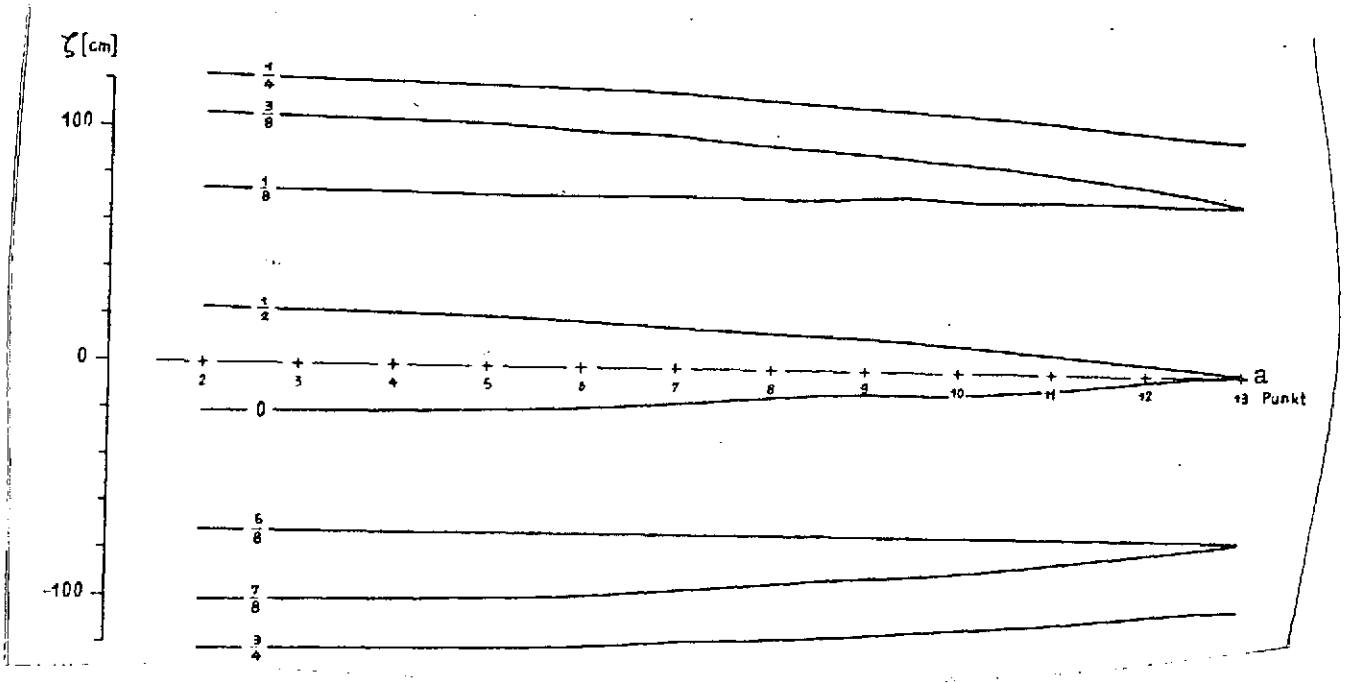


Fig. 20. $M_2$ tides in canal of constant depth. Water levels at different tidal phases (every eighth of a period). The tide waves are generated on the right, and the canal is closed on the left.

Key: a. Point

Fig. 20 depicts the water level along a longitudinal section for eight different tide phases. The effect typical of canals of these dimensions is found, namely that the amplitude of the water level increases toward the end of the canal. It should also be observed that the water level rises and falls practically simultaneously over the entire canal, so that no nodes or anti- /61 nodes can form within the canal. This oscillation pattern is consistent with well-known results for standing waves in canals of constant depths, as given by e.g. von Trepka [27]. The equation

$$L = T\sqrt{gh} \qquad \text{(T is the period)}$$

yields a value of almost 1000 km for the wavelength L of the $M_2$

type if h = 50 m. This value is many times the length of the canal. The linearity of the starting equations is manifested in the virtually mirror-symmetric surface pattern relative to the axis $\zeta = 0$ for tide phases T/2 apart in time.

The horizontal and vertical velocities distributions are given in Fig. 21 for two selected tidal phases along a lengthwise section of the canal. In order to bring out the relatively small vertical components of the velocity, the vertical dimension was stretched by a factor of 800.

Horizontally, the flow velocity is a maximum at the entrance, and vertically, it is greatest at the surface, the velocity decreasing toward the end of the canal and toward the bottom. At the entrance of the canal, the flow vector has only a relatively small vertical component. The latter grows toward the end of the canal and, given the distortion in the diagram, results in a predominantly upward or downward flow at the fixed boundary. The upper diagram (influx and upward motion) is associated with the canal filling, and the lower pattern (outflow and downward motion) with the canal draining (cf. Fig. 20).

The line connecting the tips of the arrows for a fixed point in the horizontal plane yields a vertical profile, which is analogous to that discussed later in Fig. 37 (top).

## 2. Tide in Canal of Variable Depth

Since marine areas of constant water depth are very rare in nature, one of the principal objectives was to incorporate a variable depth profile into the HN models at an early point. In /63 order to accumulate numerical and programming experience, some simple canal models with schematic depth increments were first investigated. The properties of the $M_2$ tide in a canal 92 km long with variable depth was studied under conditions otherwise identical to those in Example 1.

The depth profiles employed are shown in Fig. 22.

Example 2: canal 50 m deep, with ridge 20 m deep in middle;

Example 3: canal divided into two sections, one 20 m deep and the other 50 m deep;

Example 4: canal with stair-shaped configuration (five levels with /64 depths of 10, 20, 30, 40, and 50 m).

The results of these studies are summarized in Figs. 23, 24, and 25: as in Example 1, the diagrams show the form of the water

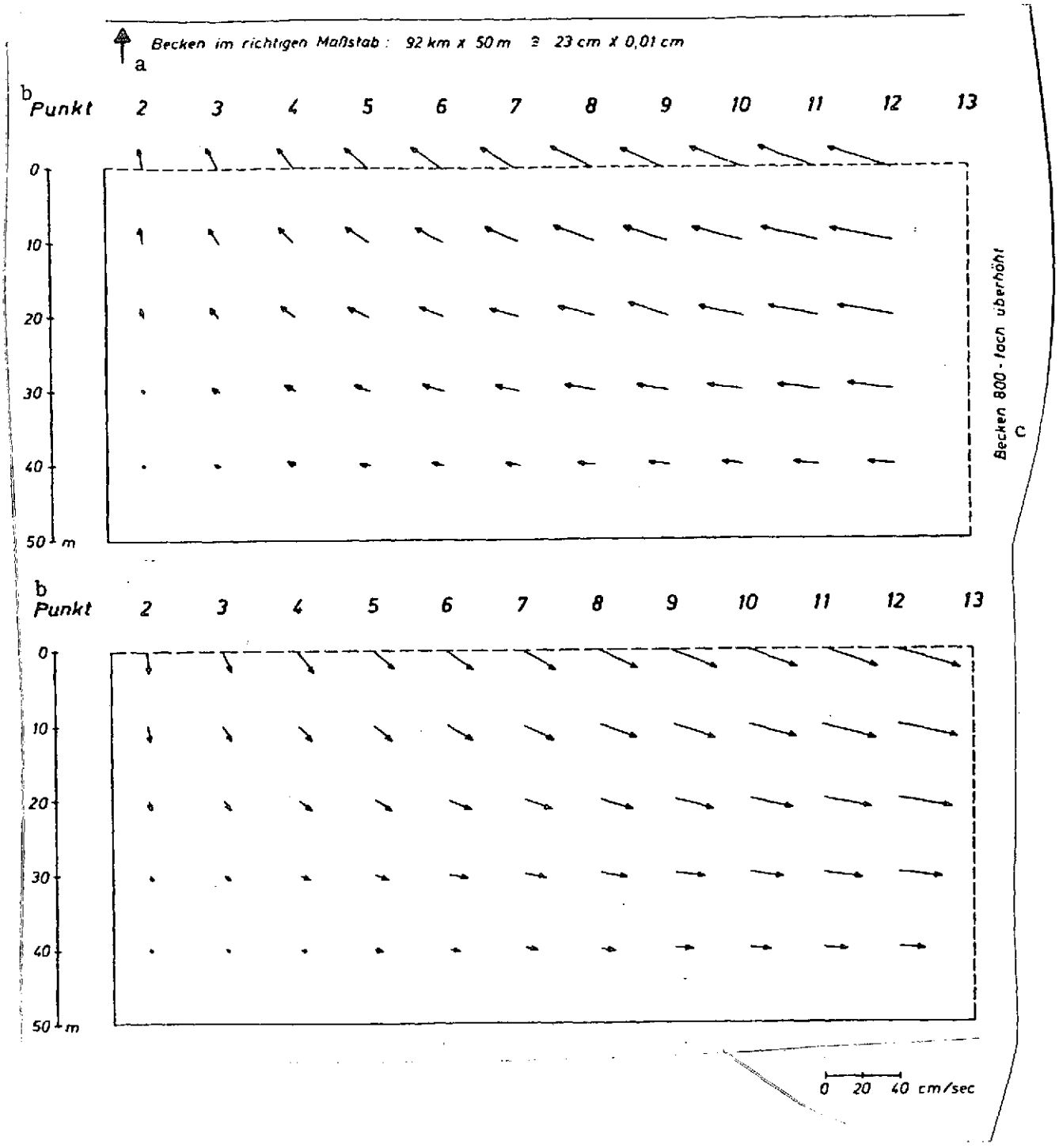


/62

Fig. 21. $M_2$ tide in canal of constant depth. Velocity distributions (longitudinal section) for two different tidal phases (t = 0, t = T/2). The vertical scale of the canal is exaggerated by a factor of 800; the thin line at the top of the diagram reflects the true dimensions of the section.

Key: a. Basin on the correct scale
b. Point
c. Height of basin exaggerated by a factor of 800

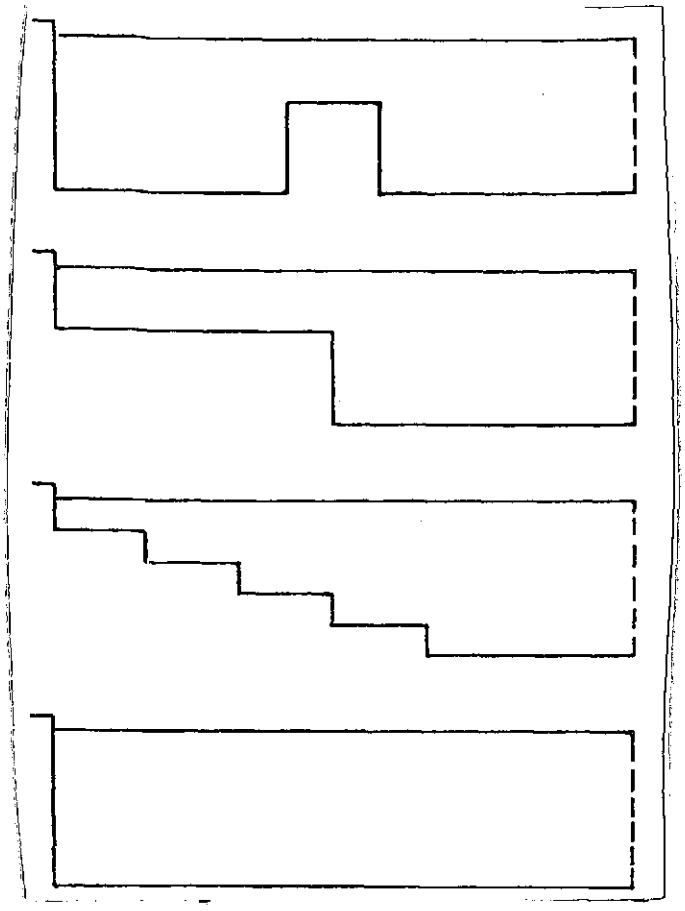

Fig. 22. Schematics of canal models with simple depth increments (upper three) in comparison to model with constant depth. The tide is generated at the right, and the canals are closed on the left.

surface (for eight tidal phases) and the velocity distribution (for two tidal phases) along the longitudinal section for the steady state.

First consider the water levels. It was found that the modified depth structure had had a decisive influence on the configuration of the water surface. There is greater shape variety in the longitudinal profiles, and extrema are observed in the interior of the canal. It is characteristic that there are now points in the canal (indicated in the drawing by a vertical line) distinguished by a particular steep water-level gradient, thus suggesting an oscillatory node. This effect occurs in the region of the ridge in Example 2 and near the change in depth in Example 3. In Example 4, there are actually two such "nodes."

The greater complexity of these curves are compared with those in Fig. 20 is a symptom of the fact that the water level in the canal no longer rises and falls simultaneously along its entire length. Parts separated off by obstructions and shallow areas of the canal are not capable of immediately following the motion of the water level at the entrance. They participate in this motion with a certain phase lag, so that sometimes the water level in these sections is still rising while the level has already begun to fall at the entrance, and conversely.

The velocity fields have also been greatly altered by the modified depth structure. The changes in depth alter the cross section and thus intensify vertical transport and raise horizontal velocities are particularly shallow points. Inherently, conditions are most drastically modified near the disturbance, i.e. the change in depth, while otherwise there is a tendency to preserve the original state, namely in the entrance zone of the canal.

/65

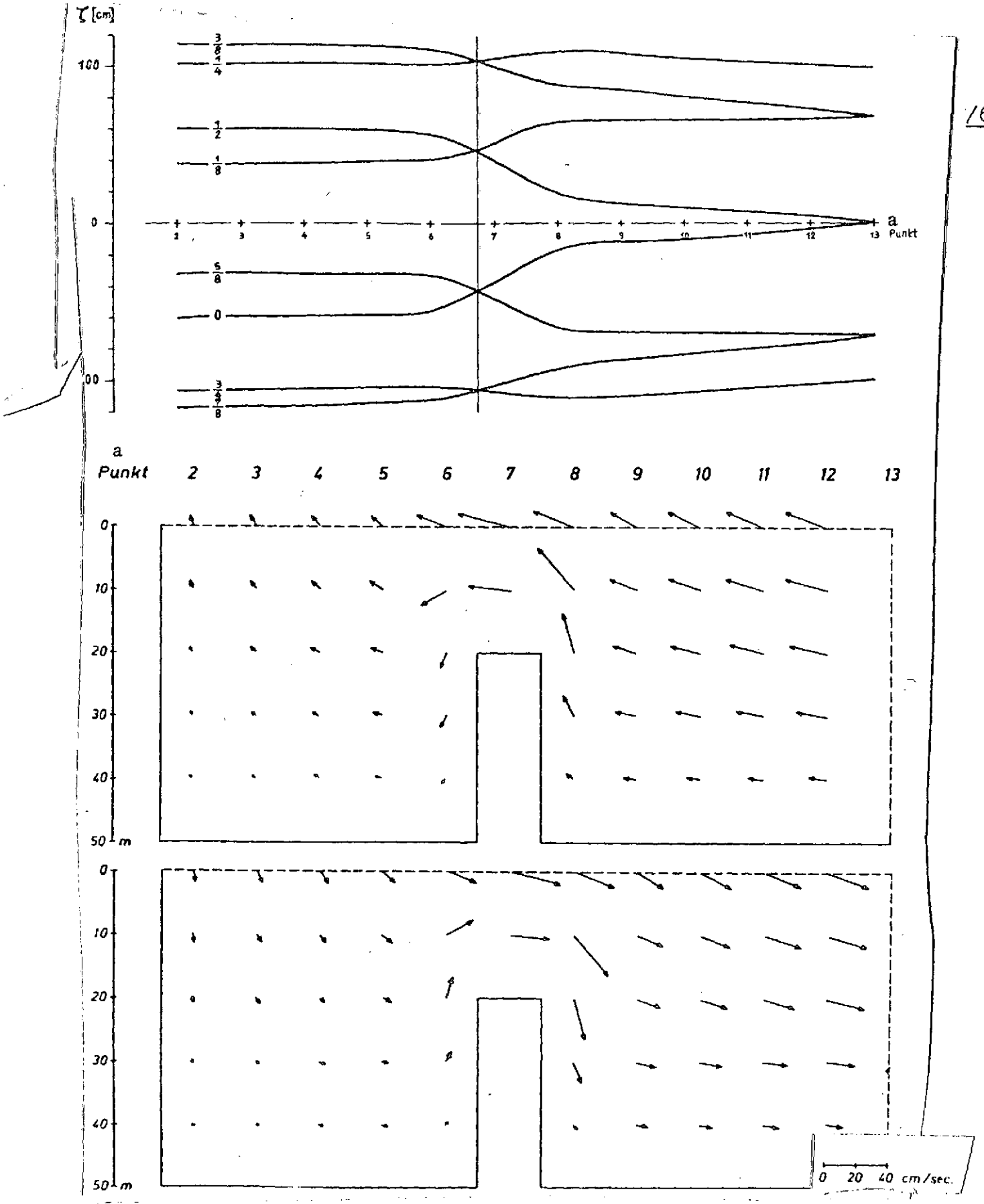


Fig. 23. $M_2$ tide in canal with ridge. Top: water level every eighth of a period. Center: velocity distribution for t = 0. Bottom: velocity distribution for t = T/2.
Key: a. Point

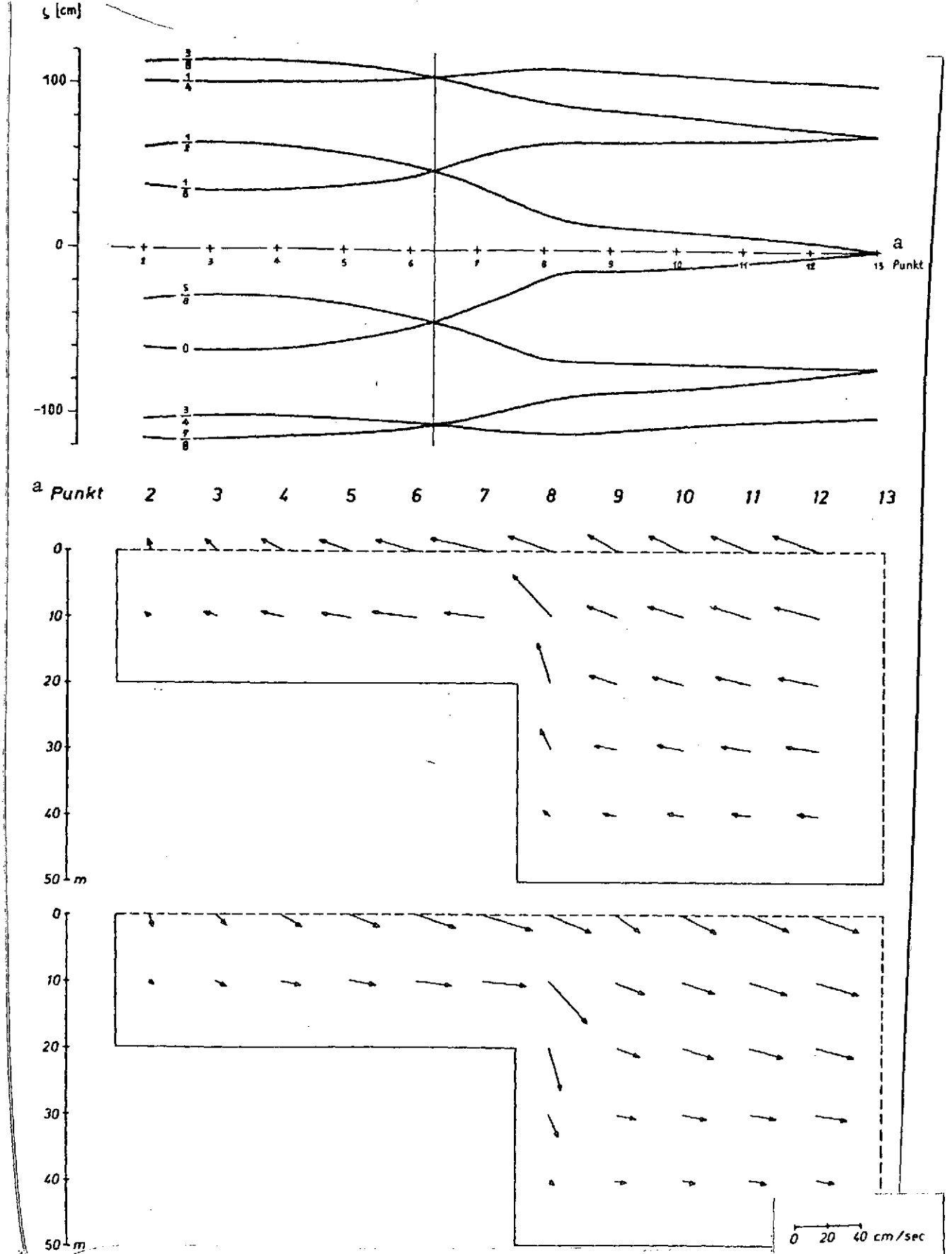


/66

Fig. 24. $M_2$ tide in canal with two different depths. Top: water level every eighth of a period. Center: velocity distribution for t = 0. Bottom: velocity distribution for t = T/2.

Key: a. Point

/67

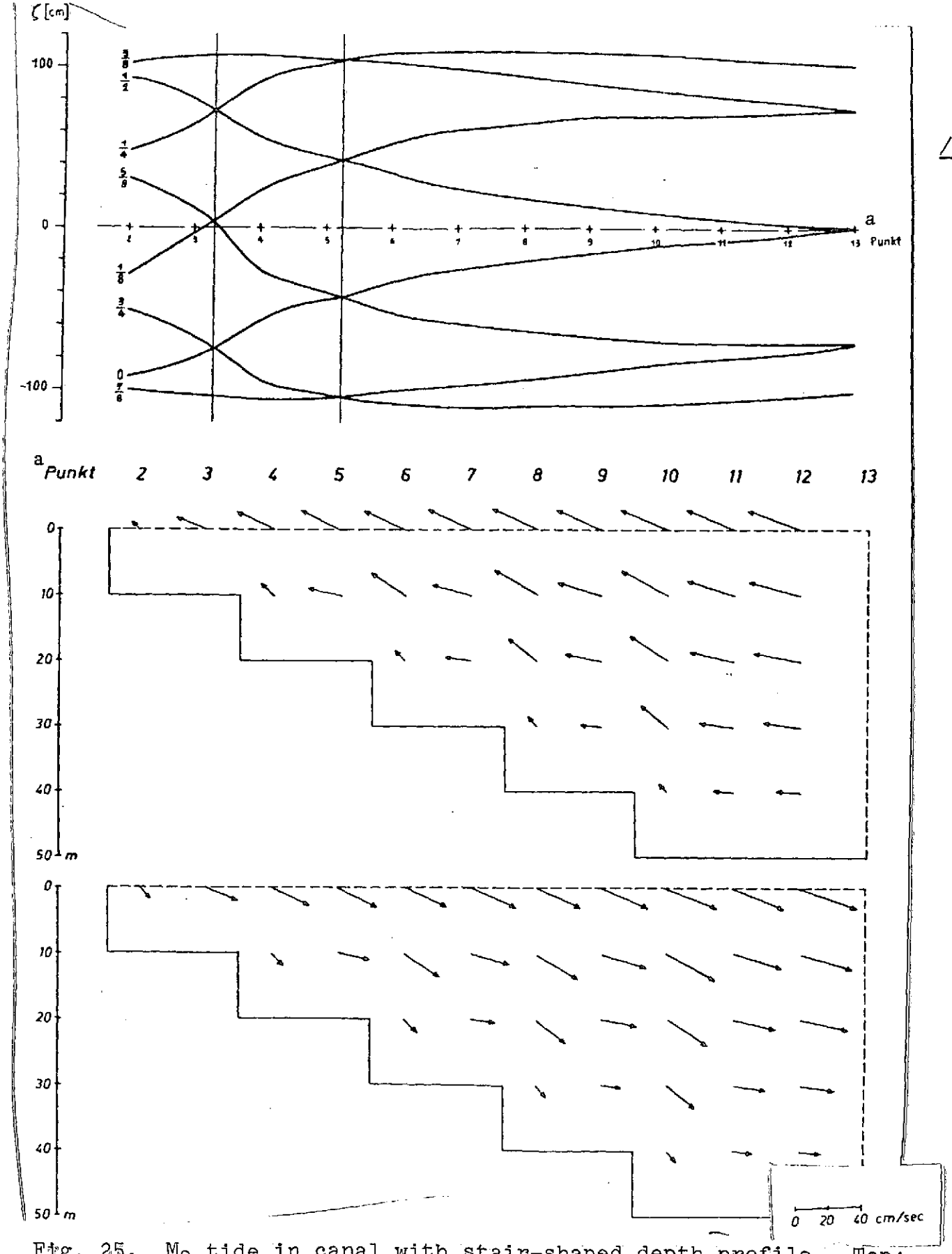


Fig. 25. $M_2$ tide in canal with stair-shaped depth profile. Top: water level every eighth of a period. Center: velocity distribution for t = 0. Bottom: velocity distribution for t = T/2.

Key: a. Point

Example 5: /68

Already with a view to practical applications and thus to HN models conforming to natural conditions, the next example dealt with a canal with a "natural" depth profile: from the IfM's HN model of the North Sea, the Grimsby-Esbjerg depth profile was taken and converted to a canal model (Fig. 26). (In order to make it easier to compare it with the models just discussed, the canal was again taken to include only 13 points, so that the profile terminated before the Danish coast of the North Sea was reached.)

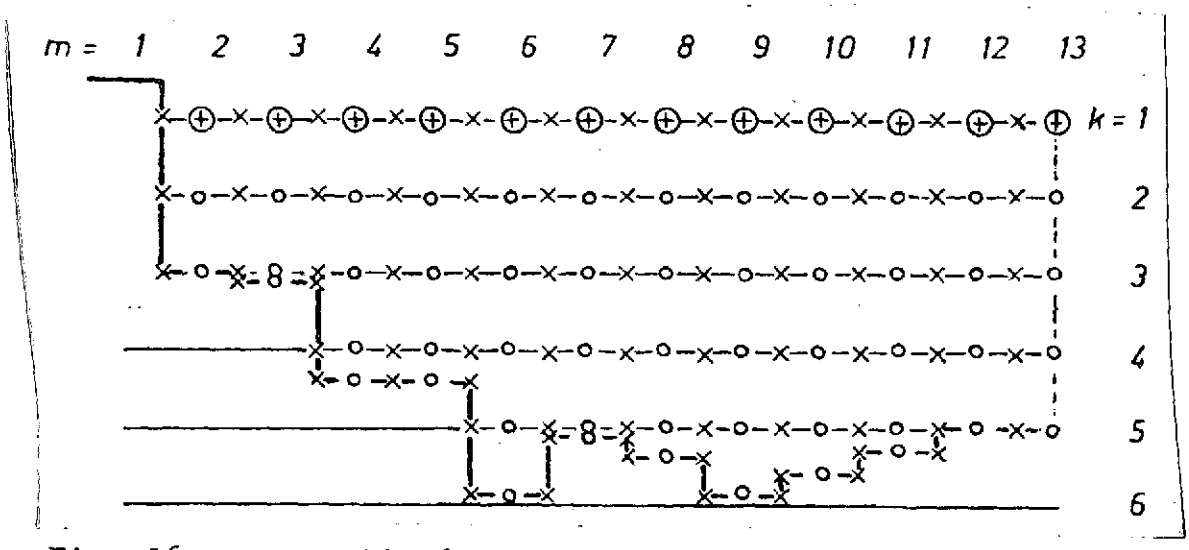


Fig. 26. x-z grid of the model canal with variable depth ($\ell$ = 92 km, h as given by section n = 17 in the HN model of the North Sea).

The canal is again 92 km long, and a tidal oscillation with an amplitude of 100 cm was applied at the right edge. Fig. 26 shows that although the vertical spacing $\Delta z$ was constant, the depth increments were no longer "quantized," i.e. were no longer multiples of $\Delta z$, instead conforming to natural conditions.

The most important results are collected in Figs. 27 and 28 for the steady state. First, Fig. 27 again shows the position of the water level for various tide phases. Comparing these curves /69 with those for a canal of constant depth (Fig. 20), we find changes which are smaller than those in Examples 2, 3, and 4. This indicates that while the present model, as a whole, does exhibit a more complicated depth fine structure, it differs less than the other models from the canal with constant depth. Only the left end of the canal, in which the water is only about

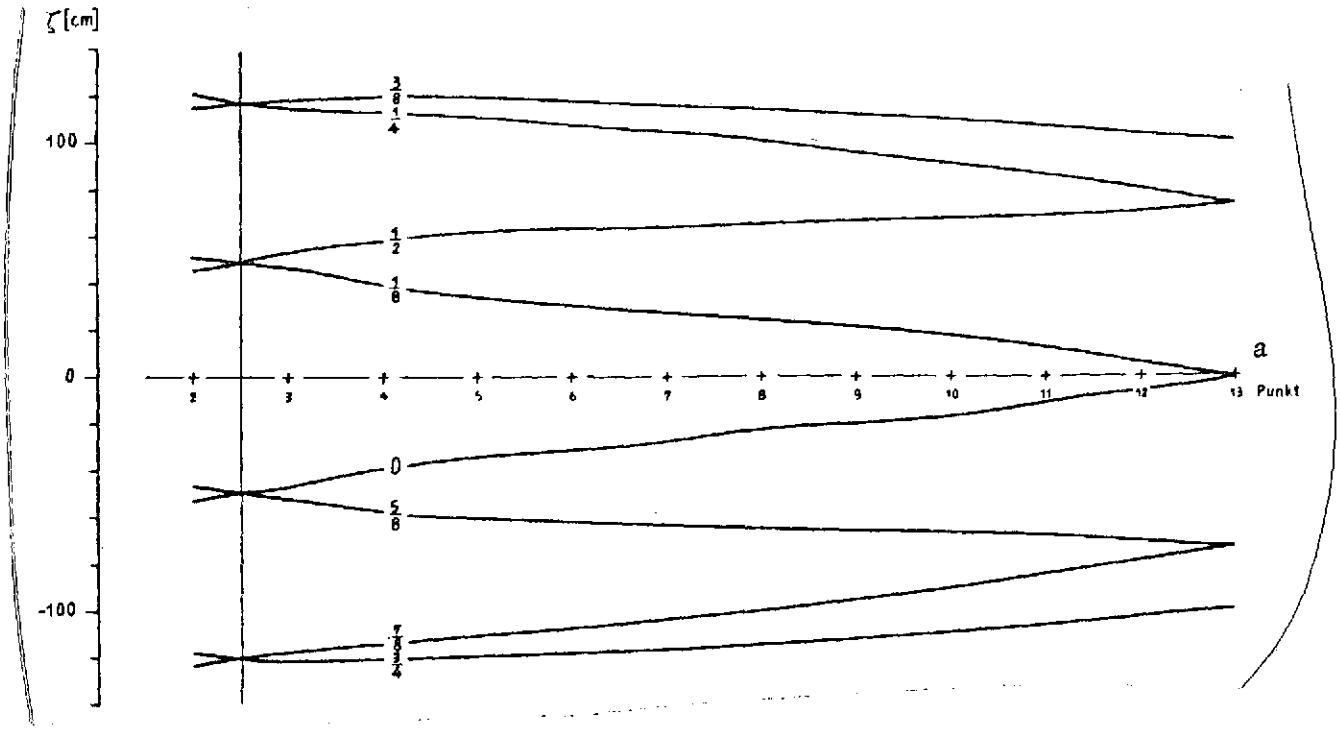


Fig. 27. $M_2$ tide in canal of variable depth. Water levels at different tide phases (every eighth of a period).

Key: a. Point

20 m deep, is there again a phase lag in the tides and thus an intersection point for different water levels (again designated by a vertical line in the diagram).

Neither does the flow diagram -- given in Fig. 28, again for two tide phases -- differ very much from that in the canal of constant depth (Fig. 21). Because the water is shallower at the entrance, the maximum velocities here and over the entire canal are greater than in Example 1. From Fig. 28, it can be seen that there is a tendency for the tidal flow to follow the depth profile.

## 3. Wind in Canal of Constant Depth /71

Example 6:

To calculate wind-induced circulation in a canal of constant depth, the model reproduced in Fig. 19 is again employed, but with slight modifications. It is assumed that the canal is also closed on the right; the corresponding fixed boundary corresponds

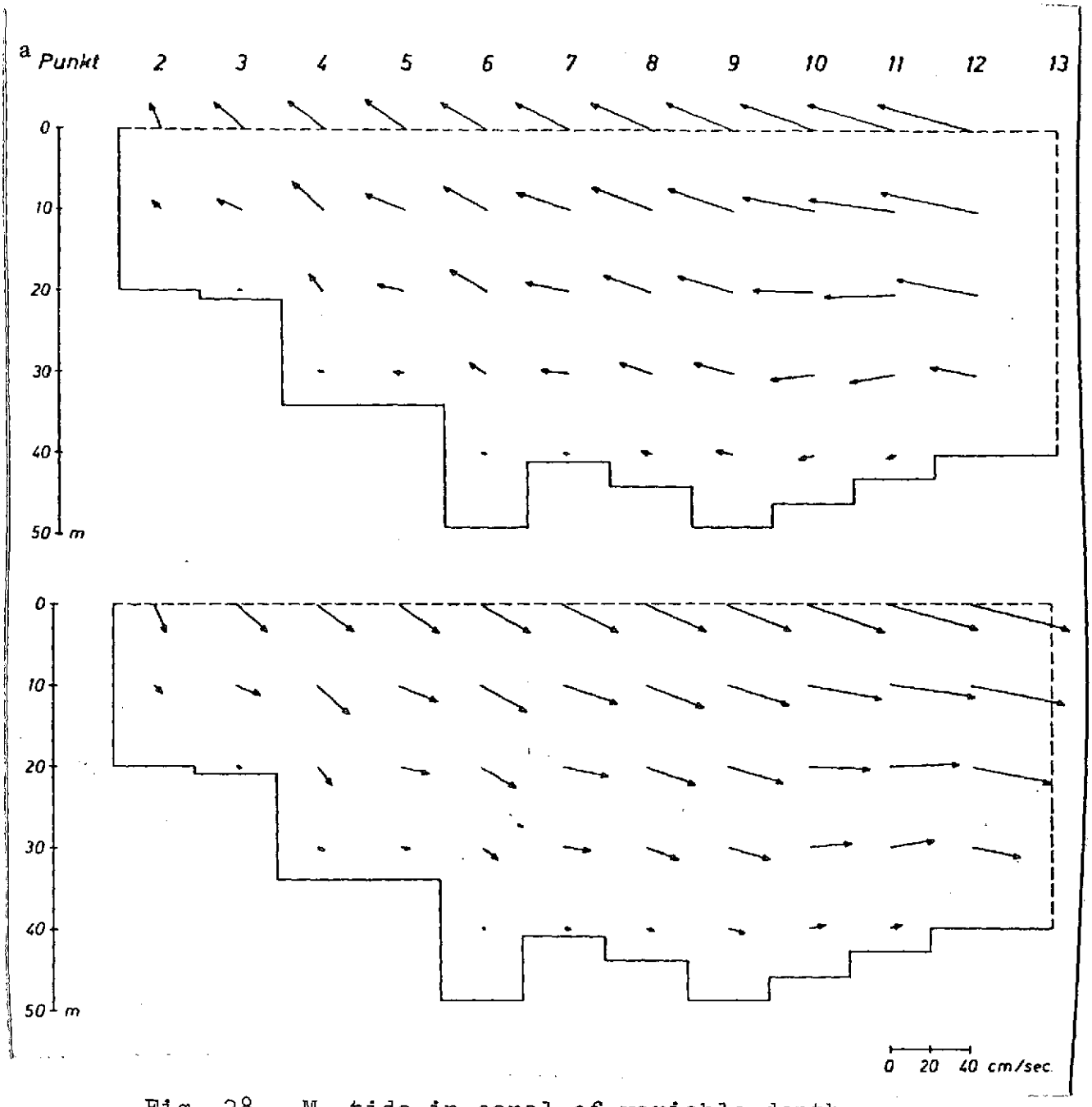


Fig. 28. $M_2$ tide in canal of variable depth. Velocity distribution at two different tide phases ($t = 0$, $t = T/2$).

Key: a. Point

to u-point 13, so that the canal now is 96 km long. A constant west wind (blowing from left to right) with a velocity of 20 m/sec is assumed. The other parameters are the same as in Example 1. The tangential wind-stress coefficient was chosen to be $\lambda = 3.2 \cdot 10^{-6}$.

Fig. 29 shows the configuration of the water surface and the velocity distribution along a longitudinal section for the steady state, which was reached after about 2 days (model time). The water level has the form of an inclined plane; in the west, it is below the undisturbed level, and in the east it is raised by the same amount (to an accuracy of $10^{-3}$ cm).

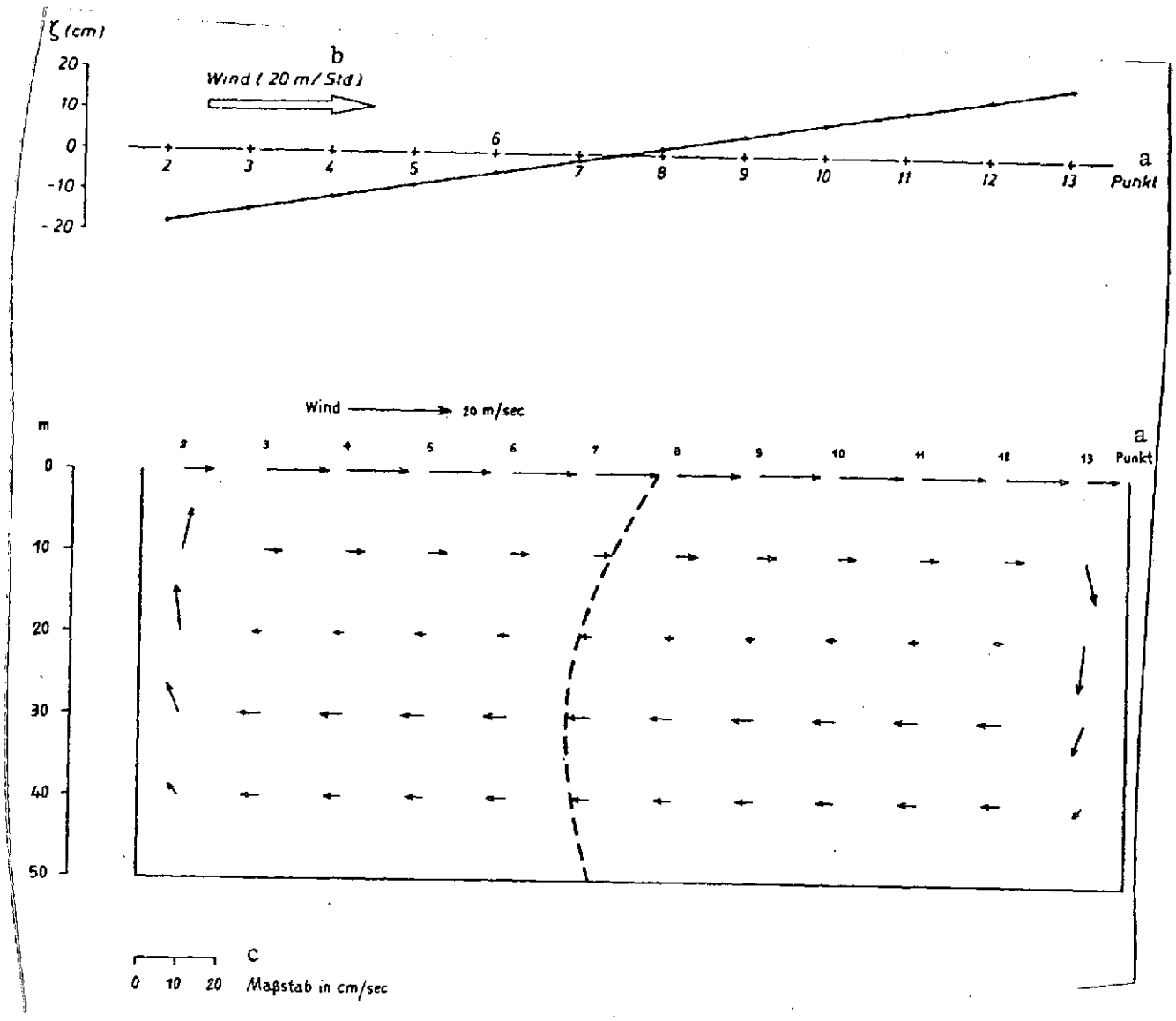


Fig. 29. Steady wind over closed canal of constant depth. Top: water level in steady state. Bottom: velocity distribution in steady state. The broken line shows a vertical profile.

Key: a. Point
b. Hour [sic]
c. Scale

In the lower picture, the height of the basin is again exaggerated by a factor of 800. The water at the surface flows in the direction of a wind with a relatively high velocity. When it reaches the right edge, it plunges toward the bottom, resulting in a broad countercurrent moving toward the left deep in the water. At the left edge, the water again rises and once again falls under the direct influence of the wind. The vertical profiles occurring within this circulation correspond to those in Fig. 38 later on. The only points at which there is an appreciable vertical component to the flow velocity are the ends of the canal (with maxima at a depth of about 20 m; in the rest of the canal, $w < 10^{-3}$ cm/sec).

As has already been emphasized above, this result for wind-driven circulation in a canal conforms far better to natural conditions than the result of an HN model with vertically integrated equations. The latter model yields the same water levels, but also vanishing flow velocities. In the present model, the kinetic energy of the wind is converted into the potential energy of the backed-up water and into the kinetic energy of the circulation.

## 4. Tide in Basin of Constant Depth /73

Example 7:

The first really three-dimensional studies (i.e. in a region extended in two horizontal directions and one vertical one) were conducted in a simple rectangular basin 100 km long, 48 km wide, and 50 m deep. The grid -- just for the case of a closed basin, however -- can be seen in Fig. 30; it was based on the canal model (Fig. 19). The network comprises 72 internal $\zeta$-points and six computing planes in the vertical direction. The grid constants are then $\Delta x = \Delta y = 8$ km and $\Delta z = 10$ m. According to the CFL criterion (13), the time step may then be $\Delta t = 4$ min. The other constants used in the calculation are the vertical exchange coefficient $A_V = 10^3$ cm$^2$/sec and the Coriolis parameter /74
$f = 1.2 \cdot 10^{-4}$ sec$^{-1}$. At the bottom, the flow was assumed to be zero in accordance with boundary conditions (22.3).

In this three-dimensional HN model, we first studied the behavior of an $M_2$ co-oscillational tide, generated at the $\zeta$-points of the north entrance ($n = 1$) by prescribing a sinusoidal wave with a uniform amplitude of 100 cm and a constant phase. The steady state (defined to be the state in which the water levels and velocities at identical times within successive periods differ by less than 1 mm and 1 mm/sec respectively) is reached after no more than four periods.

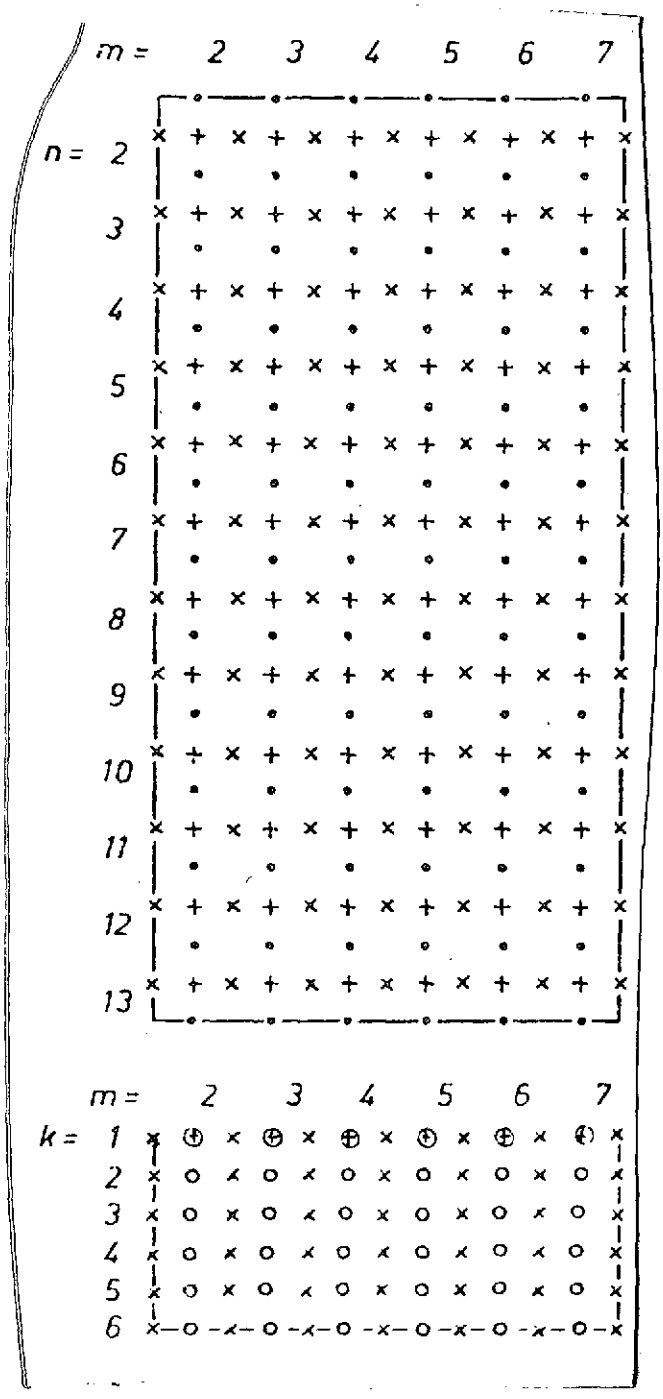


Fig. 30. Three-dimensional grid of the rectangular basin with constant depth ($\ell$ = 96 km, w = 48 km, h = 50 m). Top: top view; bottom: cross section.

We will dispense with a detailed presentation of the results of the analysis, which would consume a great deal of space in this case. The development of tides in rectangular basins has been studied very thoroughly in the literature (usually with the aid of vertically integrated hydrodynamic differential equations), so that we can restrict ourselves to certain important aspects of the vertical structure. These are shown in Fig. 31, which contains the tidal-flow ellipses in five horizontal planes (surface, 10 m, 20 m, 30 m, and 40 m) for four selected grid points. The sketch in the upper lefthand corner of each diagram indicates the position of the point in the basin. The two lower diagrams have a scale enlarged by the factor 2 for clearer presentation.

The tidal flows near the entrance have the greatest magnitudes, and the figures there have relatively low eccentricities. The further one penetrates into the interior of the basin (in this case, toward the south), the lower the velocities and the greater the tendency for the tidal flows to become narrow ellipses, finally forming virtually alternating flows. It should be pointed out, however, that the flow figures shown here refer to points situated near the axis of the basin.

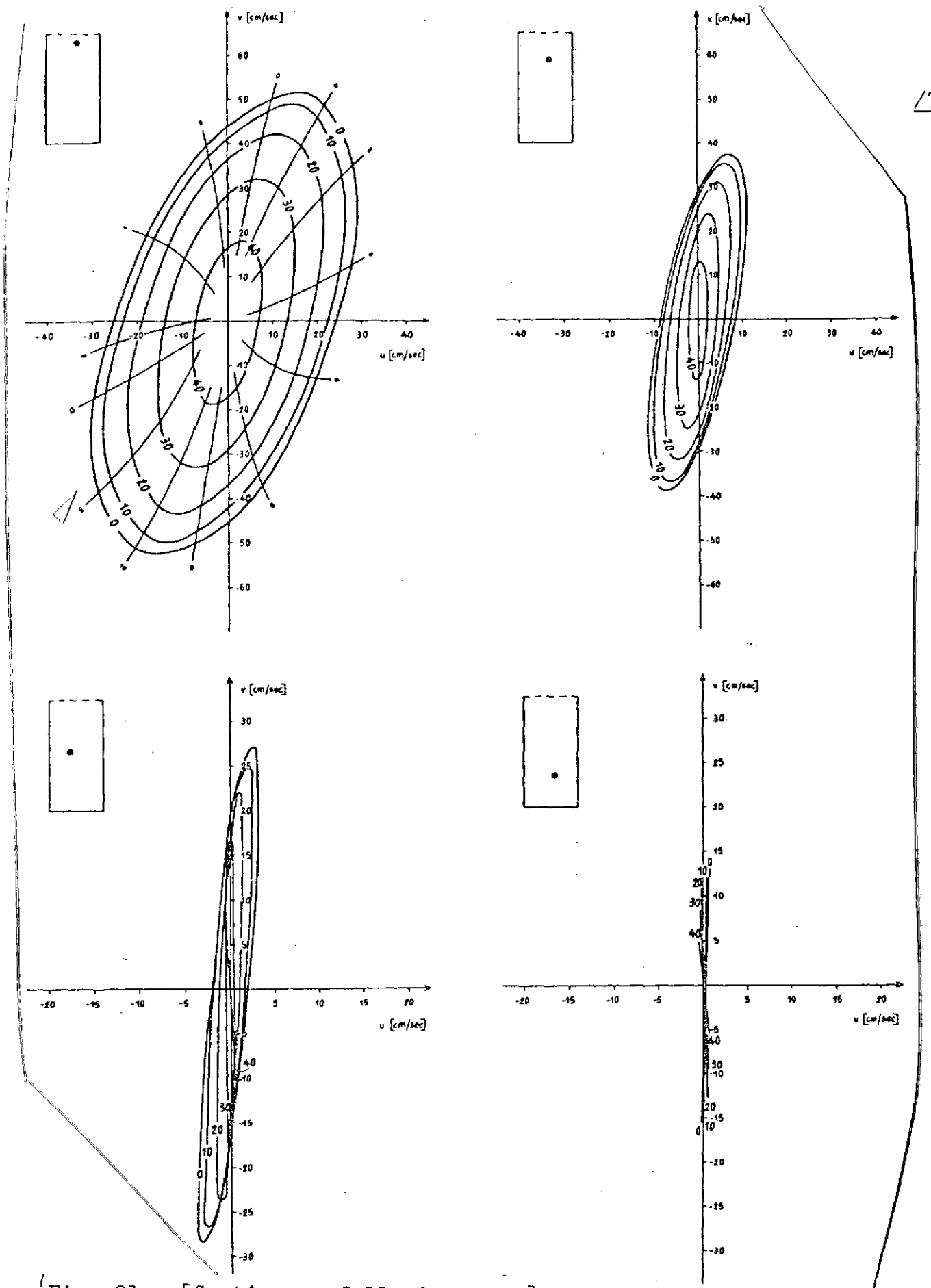


Fig. 31. [Caption on following page]

Fig. 31. $M_2$ tide in basin of constant depth. Tidal-flow ellipses in relation to depth for four selected point. The numbers by the ellipses give the depth in m. The numbers by the phases lines in the first [bottom of caption cut off].

---

In all cases, the monotonic decrease in velocity with depth /76
is very evident; the profiles resemble those found for the canal (cf. Fig. 37). It can also be seen that the direction of the tidal-flow ellipses is depth-dependent. The deeper flow figures are rotated toward the left (in the mathematically positive sense) relative to the ones near the surface, and this rotation increases with increasing distance from the entrance. Nevertheless, ellipses associated with points on the same vertical line have very similar forms.

It should also be pointed out that the sense of the rotation of the flow figures for one and the same point is the same at all depths (cf. the hour figures in the first diagram) and that -- despite the rotation of the axes -- corresponding sections on ellipses associated with points on the same vertical line are traversed at roughly the same times. This means that e.g. the flows of maximum magnitude for a fixed position (n,m) occur at roughly the same times at all depths. Kagan [25] arrived at a similar result in calculating tidal-flow ellipses for the Yellow Sea.

## 5. Wind in Basin of Constant Depth

Example 8:

The following investigations are based on the basin 96 km long depicted in Fig. 30. By analogy with Example 6, the wind is assumed to be a uniform north wind at 20 m/sec, blowing over the entire basin and constant in time. The tangential wind-stress coefficient is $\lambda = 3.2 \cdot 10^{-6}$ and the vertical exchange coefficient is $A_V = 10^2$ cm$^2$/sec. Condition (22.2) is employed as the boundary condition on the bottom, so that non-zero flow at the bottom is also permitted.

Fig. 32 shows the global circulation system which has developed in the steady state after 20 days (model time); the velocity fields in horizontal planes at six different depths are depicted.

At the surface, there is a very intensive flow system with
various directions. By and large, the flow is shifted to the /78
right of the wind direction. The absolute magnitudes of the velocities decrease rapidly with increasing depth, and the directions,

/77

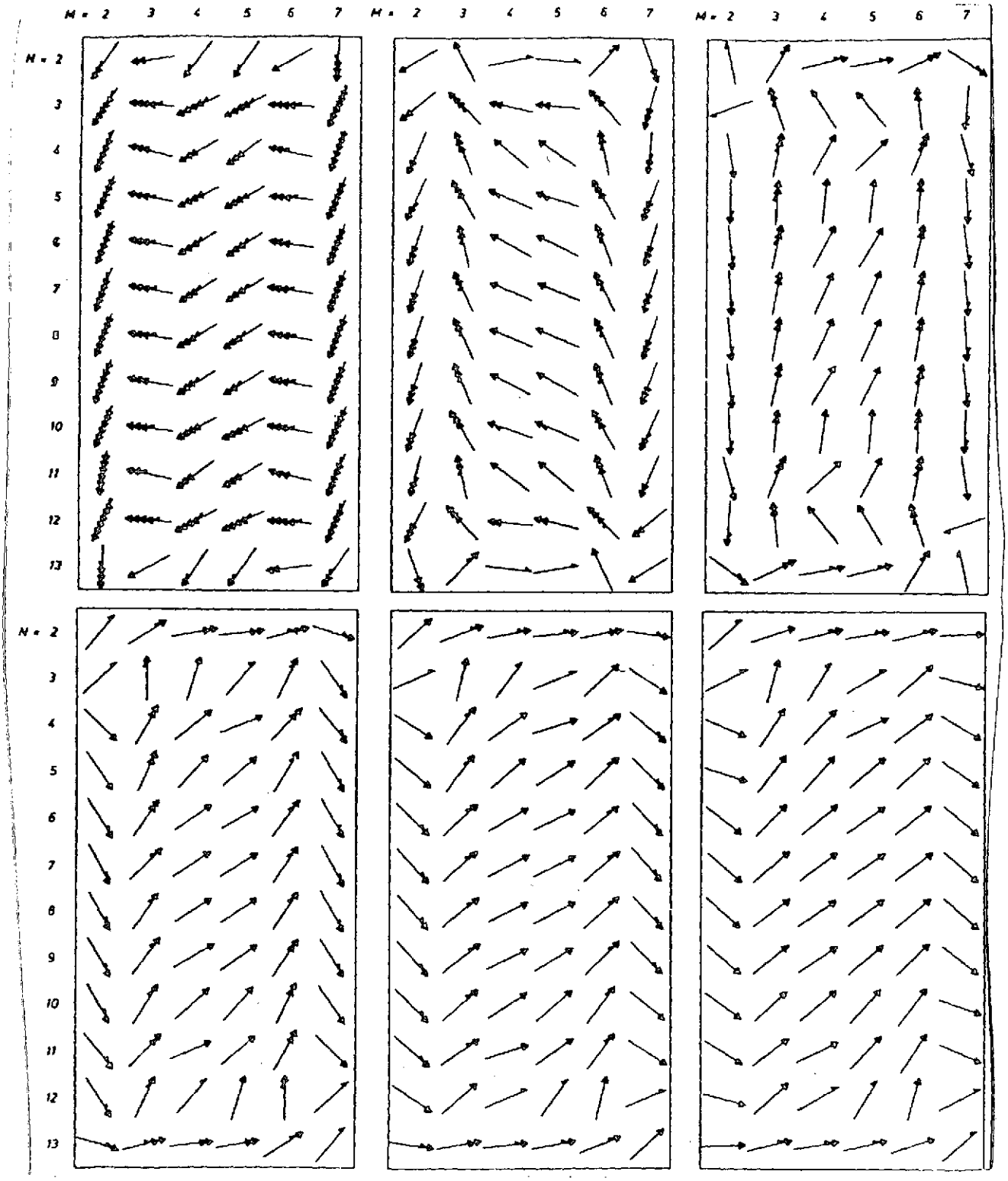


Fig. 32. North wind in basin of constant depth. Velocity distribution in steady state at various depths. The diagrams correspond to depths of (upper row, from left) 0, 10, 20 m and (lower row, from left) 30, 40, 50 m. Each 1/2-tip of arrow corresponds to 10 cm/sec.

particularly in the central portion of the basin, vary widely. For instance, just 20 m down, there is a broad northward current, while the surface flow is predominantly toward the south. Nevertheless, the flow arrows along the western and eastern edges, which always have a southwards component, indicates that transport compensation between the surface current and the deep current does not in general take place separately at every point (as in the canal, Example 6), but is supplanted by a three-dimensional compensation. The flow patterns at every depth can be transformed onto themselves by (axially symmetric) north/south and subsequent east/west interchange. The relatively high velocity can be ascribed to the relatively low energy dissipation, which is a consequence of the relatively small vertical exchange coefficient and the minor bottom friction because of condition (22.2).

Vertical flows were not calculated in this example.

An obvious step is to compare this situation with Ekman's drift current theory. First, the vector diagrams of the flow velocities at different depths are drawn in Fig. 33 for three points. A small insert shows the position of the point within the basin.

In the ideal case, the line connecting the heads of the vectors should yield the well-known Ekman spiral. The curves calculated for this case differ somewhat from the Ekman pattern, and the discrepancy obviously decreases as one moves into the interior of the basin. This situation becomes comprehensible, when it is recalled that Ekman started from an ocean which was unbounded horizontally. The closer one comes to the edge in the present model, the more seriously this assumption is violated.

In all three cases, there is a deflection toward the right at the surface; the angles are (from west to east) 20°, 99° and 57°. While the flow rotates toward the left with increasing depth at points at the very edge, the flow at points further in toward /80
the center -- in line with Ekman's theory -- rotates further toward the right, turning back toward the left only in the vicinity of the bottom, this fact is also consistent with Ekman's theory of elementary flow, obtained under the assumption of finite water depths. For the purpose of a qualitative comparison, a curve given by Ekman [28] is drawn next to the right diagram, this curve having been obtained analytically for a water depth of $h = 1.25\ D$ ($D$ = Ekman's friction depth). The curves resemble each other quite closely.

In the present case, the friction depth is found to be

$$D = \pi\sqrt{\frac{2A_V}{f}} = \pi\sqrt{\frac{2\cdot 10^{-2}}{1.2\cdot 10^{-4}}}\ \mathrm{m} = 40.7\ \mathrm{m}\ .$$

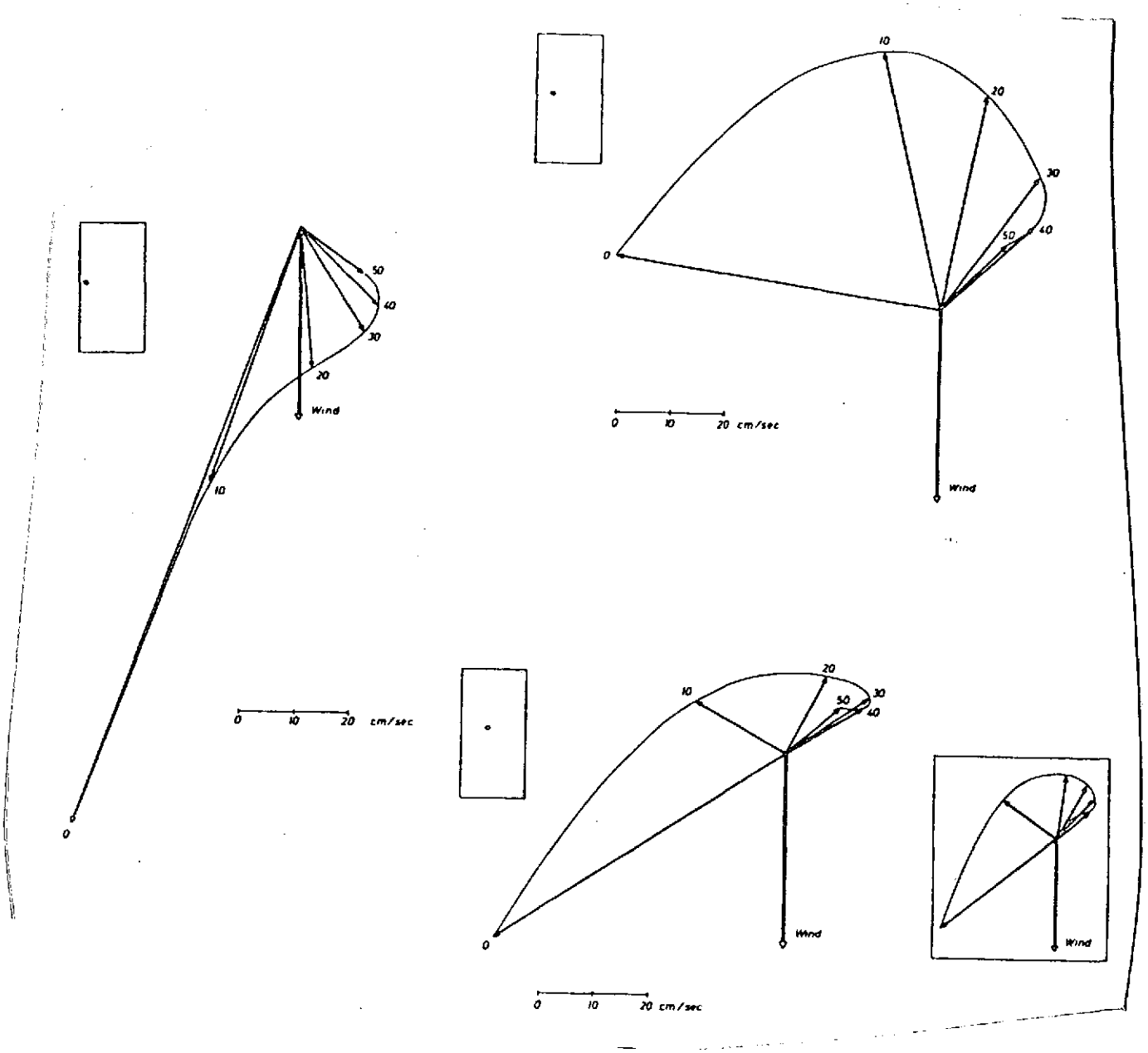


Fig. 33. North wind in basin of constant depth. Ekman flow figures (velocity vectors at various depths) for three selected points. The position of the point is shown in the sketch to the upper left of each diagram. The numbers give the depth in meters. The diagram in the box at the lower right shows a flow figure given by Ekman.

At this depth, Ekman states that the direction of the flow should be opposite to that of the surface. The diagram for the point at the bottom right shows that this is actually the case in the numerical model at this point.

Lastly, Fig. 34 permits a comparison with the unsteady Ekman theory. This diagram depicts the line connecting the velocity vectors at the surface at the point (6,4) (cf. Fig. 30) in relation to time (hodograph). According to Ekman [28], the velocity vector, in "homing in" on the 45°-direction, travels along the curve in the form of a Cornu spiral (cf. Fig. 34, right). Aside from the fact that the theoretical limiting angle of 45° is exceeded by 12° in the present example, the two hodographs exhibit remarkable similarity, particularly with regard to the times at which the specific sections of the curves are traversed.

/81

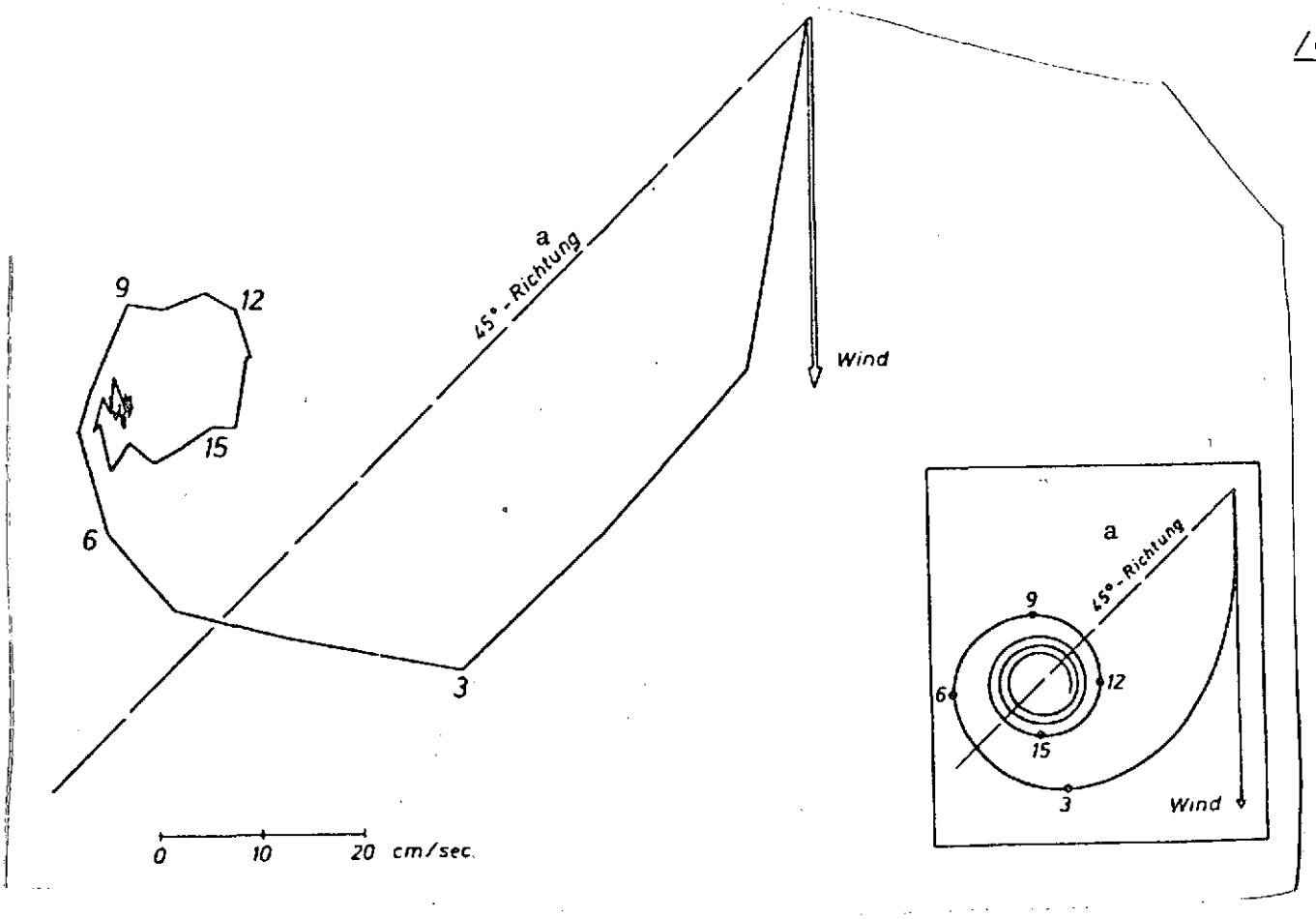


Fig. 34. North wind in basin of constant depth. The position of the tip of the surface vector in relation to time for the point (6,4); cf. Fig. 30. The numbers give the time in hours from the start of the wind. The diagram in the box at the lower right shows the corresponding curve as given by Ekman's theory.

Key: a. Direction

## 6. Stability of the Explicit Methods /82

Example 9:

In order to test numerically the stability analyses carried out on the explicit method in Section II.4.1, a number of HN models with various constant vertical spacings $\Delta z$ were studied for the case of a constant wind. As in Example 6, a canal was represented by six computing planes, the depth of the canal $h = 5\Delta z$ depending on the choice of $\Delta z$. Example (A) on p. 39 required a vertical distance step of

$$\Delta z > 7.48 \text{ m} \tag{55}$$

based on the theory of numerical stability. The calculations were therefore arranged so that various spacings near this critical value were employed.

The results of eight representative computations (for the values $\Delta z$ = 5, 6, 7, 7.3, 7.5, and 7.45, 7.48, and 10 m) are collected in Fig. 35. The latter shows (a) the water level at point 13 of the model in Fig. 19, considered as closed, and (b) the horizontal velocity at the surface at point 12, both as functions of time. For reasons of clarity, these diagrams are subdivided into a long-scale (time interval 10 hours) figure at the top and a short-scale (time interval 10 days) figure at the bottom.

On the whole, the result of the numerical computation illustrated in Fig. 35 agrees very well with the theoretical result. In particular, unstable behavior was in fact found when the spacing $\Delta z$ was less than 7.48 m. The "greater" the violation of criterion (55) the sooner the "overrun" (excessively large positive or negative numbers) occurred. For instance, the computer broke off the calculation for $\Delta z$ = 2 or 5 m after just 1 hour (12 time steps), but not for 7.5 hours when $\Delta z$ = 7.3 m and not until 1.5 days when $\Delta z$ = 7.45 m. It is noteworthy that the instability appears much /84
earlier in the velocity than in the water level, so that even with extreme velocities, the computation continues for quite a while before the arithmetic check interrupts it. The appearance of the instability is always preceded by a monotonic drop in the eastward velocity at point 12, which finally turns around into a growing westward (= against the wind!) flow.

To this extent, the HN model with $\Delta z$ = 7.48 m also harbors the danger of instability, although the water level has already achieved a relatively steady value after 10 days. In point of fact, the value $\Delta z$ = 7.48 m still violates criterion (55). Unfortunately, there is no corresponding comparison calculation with

/83

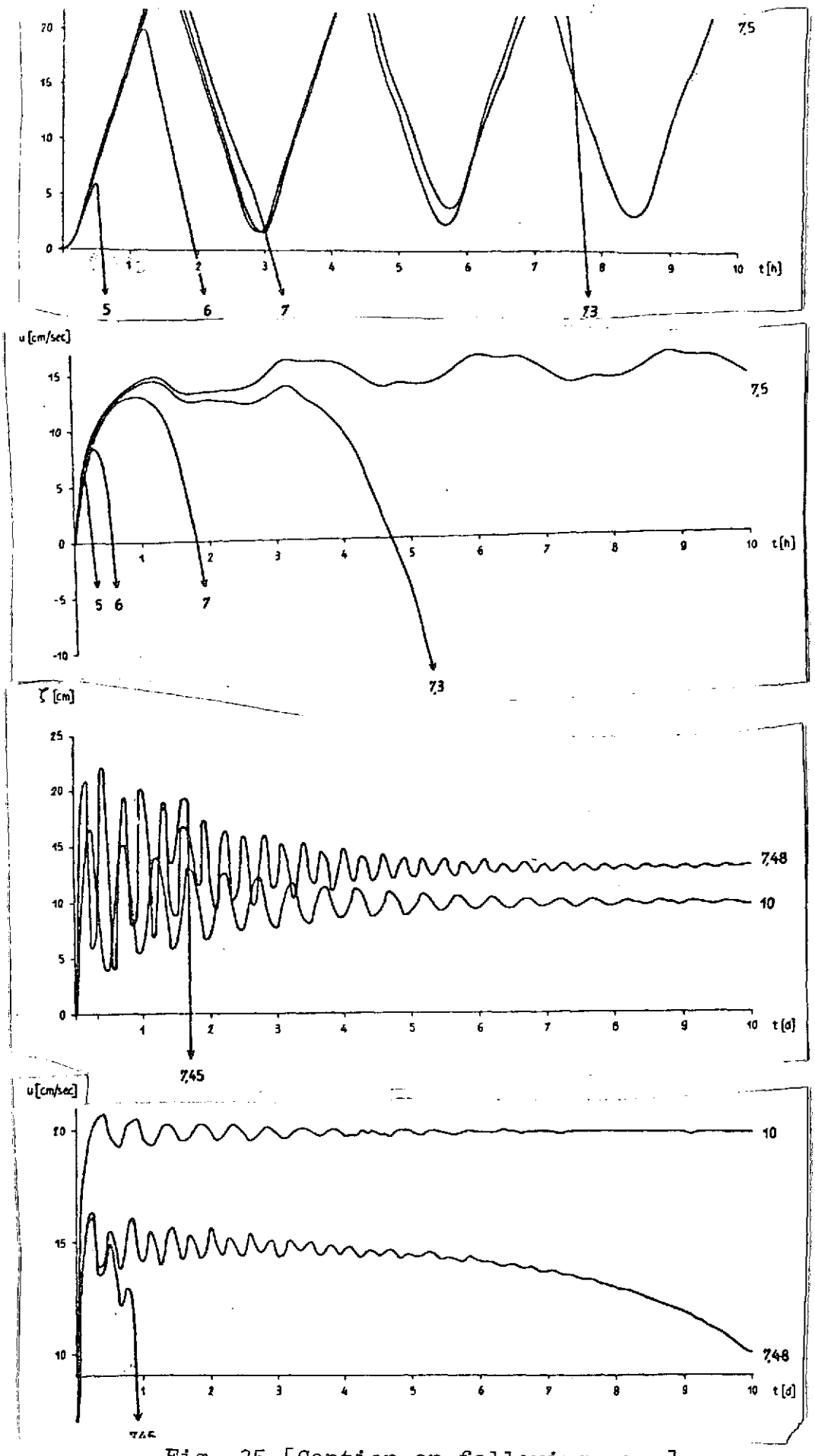


Fig. 35 [Caption on following page]

Fig. 35. Stability of explicit difference method with various vertical spacings z. Water level and flow velocity at surface at right side of canal model depicted in Fig. 29 (wind) as functions of time. The two upper diagrams cover a period of 10 hours, and the lower a 10-day interval. The numbers by the curves give the vertical spacing in meters.

---

$\Delta z$ equal to about 7.50 m, covering a period of about 10 days, which should then show complete stability (with respect to velocities as well). The corresponding curves for $\Delta z$ = 10 m are given, and exhibit unambiguously stable behavior.

In summary, this series of numerical tests has demonstrated the practical effectiveness of the theoretical stability criterion derived above.

## 7. Comparison Between Explicit and Implicit Methods

Example 10:

The explicit and implicit HN methods were compared for the case of wind-induced motion in the closed canal discussed in Example 6.

Fig. 36 depicts the vertical profile of the horizontal velocity for various HN models, as found for the steady state over the entire canal (cf. Fig. 29). The curve on the right was first obtained with the aid of the explicit method and a constant spacing of $\Delta z$ = 10 m. Within the output accuracy of the computer ($10^{-3}$ cm or cm/sec for water level and speed respectively), it coincides with the corresponding result of the implicit method with the same choice of spacing. /85

The center curve and the outer curve on the left were obtained with the aid of the implicit method for the same wind-induced motion, but with other spacings. The grid was refined near the bottom in order to get a more detailed picture of the bottom zone, which is very important dynamically. The intervals ranged from 2.5 m (center curve) to 0.25 m and even 0.01 m (curve on the left) at the very bottom. As Example 9 indicated, the lower limit of the refinement would have been about 7.5 m for the explicit method; the implicit method, on the other hand, even with the narrow spacing chosen here, provides stable solutions -- consistent with theory.

Fig. 36 shows that the solutions obtained for the identical problems with different vertical spacings agree quite well with each other. The further apart the spacing patterns were, the

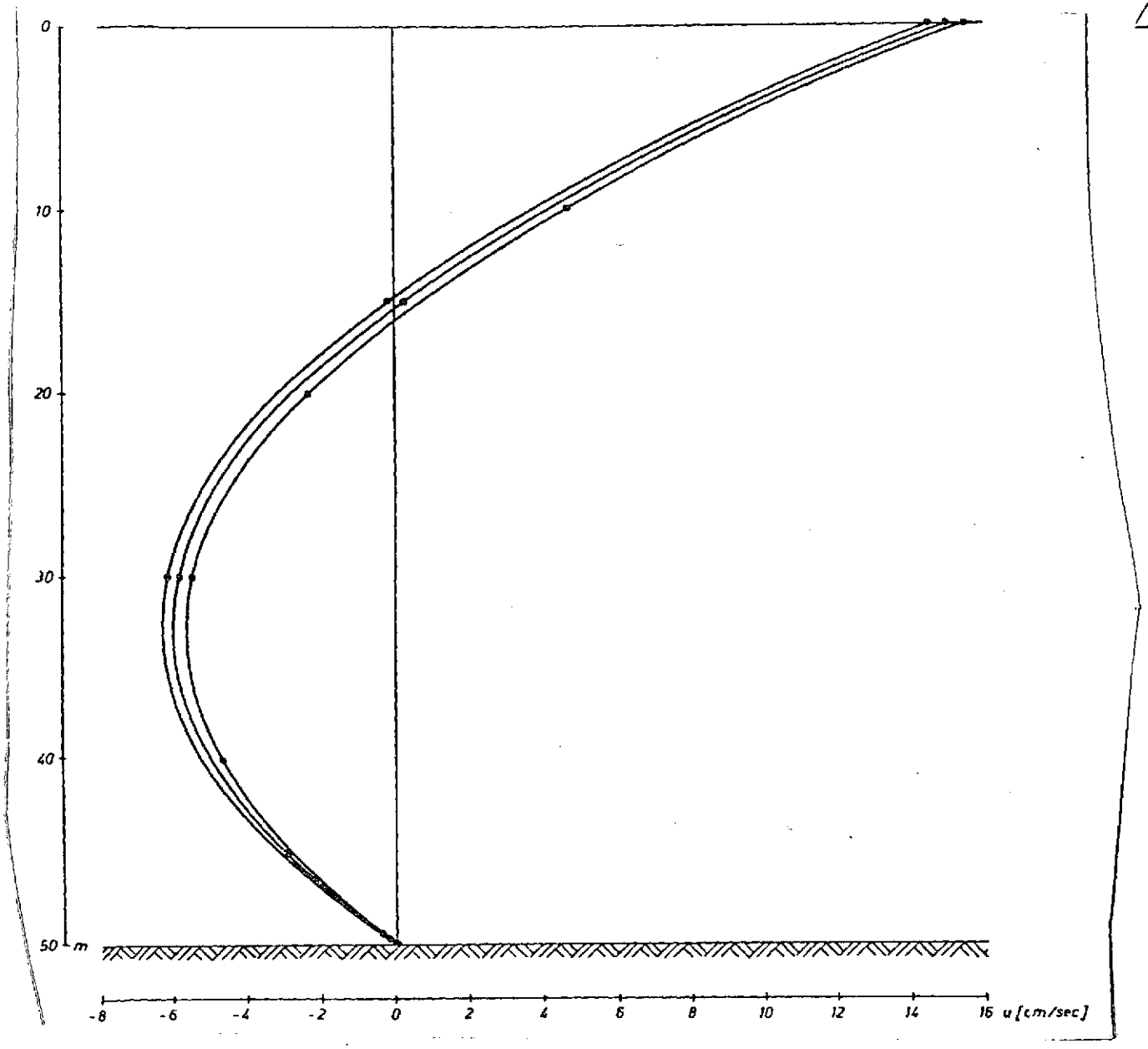


Fig. 36. Comparison between explicit and implicit difference methods. Vertical profile of flow velocity in steady state for wind-induced motion in canal model of Fig. 29.

Right curve: explicit and implicit method for $\Delta_k z$ = 10 m (k = 1,...,5)

Center curve: implicit method for $\Delta_k z$ = 15, 15, 15, 2.5, 2.5 m (k = 1,...,5)

Left curve: implicit method for $\Delta_k z$ = 15, 15, 19.5, 0.25, 0.25 m ( (k = 1,...,5)
$\Delta_k z$ = 15, 15, 19.89, 0.10, 0.01 m (k = 1,...,5).

greater the differences that resulted. The principal numerical differences occurred in the approximation of the shear-stress term at the surface, leading to slightly different surface velocities and eventually affecting the entire vertical profile.

On the whole, however, the vertical profiles for horizontal velocity are very similar and show that the implicit method can be employed with consistent success.

## 8. Vertical Profiles /87

These numerical studies have been based predominantly on the boundary condition (22.3) -- u = 0 at the bottom. This zero-flow condition is very common in the literature. Measurements have corroborated it, although current measurements are not practical right at the bottom, but must be taken a few centimeters away.

For comparison, computations have also been performed with the boundary condition (22.2) -- in general $u \neq 0$ at the bottom.

Example 11:

A direct comparison will now be made between the two boundary conditions with the aid of a canal model. The vertical profiles of flow velocity at an interior point during different tide phases are plotted in Fig. 37 for the case of the $M_2$ tide in a canal of constant depth (cf. Example 1) with a constant vertical exchange /88 coefficient $A_V = 10^3$ cm$^2$/sec. In the upper diagram, boundary conditions (22.3) was employed, and boundary condition (22.2) in the lower one. Water level vs. time is given (with the same height scale) in each case -- as the upper boundary of the profiles.

It is evident that the second boundary condition (lower picture), which permits non-zero velocities at the bottom, is hardly suitable for reproducing the observed tidal-flow profiles: the small amount of bottom friction implies that the horizontal velocity will decrease only slightly with increasing depth.

The condition u = 0 at the bottom (upper picture), on the other hand, leads to relatively steep vertical gradients for the horizontal velocity. The maximum flow velocities at the surface are now much larger than in the other case. During most of a tide period, the profiles are characterized by a monotonic decrease in velocity with depth. Only when the tide is turning are there flow distributions with maxima below the surface (at 7h) or even with a reversal of direction (at 0h). It is obvious that the tide turns first at the bottom.

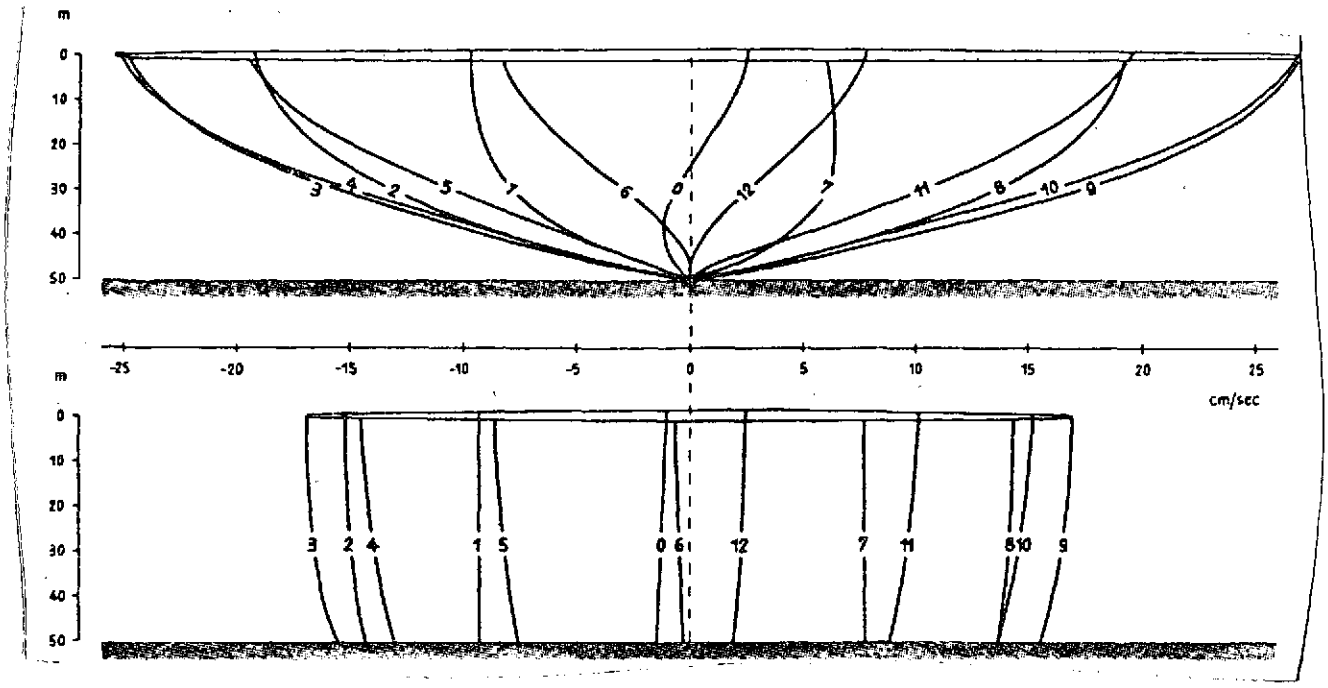


Fig. 37. $M_2$ tide in canal of constant depth for different boundary conditions at the bottom ($A_V = 10^3$ cm$^2$/sec). Vertical profiles of flow velocity in interior of model canal depicted in Fig. 19 (point m = 7) for various tide phases. The numbers by the curves mean hours (after lunar transit at Greenwich).
Top: boundary condition $u_B = 0$ (cf. (22.3)).
Bottom: boundary condition $\tau_B = r|u_B|u_B$ (cf. (22.2)).
The upper boundary of the profile is the associated water level.

Water level as a function of time is roughly the same in both cases.

The vertical profiles of tidal flow depicted in the upper diagram were given in very similar fashion by Sverdrup [18]. Sverdrup based his work on analytical solutions of hydrodynamic differential equations and likewise used a constant exchange coefficient $A_V$.

The vertical profiles computed here do agree roughly with the observed curves, but do not adequately reproduce an essential property of natural flow profiles, namely the steep gradient near the bottom (cf. Fig. 39). To this extent, the conjecture expressed in Section II.5 -- that assuming a constant exchange /89
coefficient $A_V$ would tend to produce linear profiles -- has been confirmed.

Example 12:

Fig. 38 shows an analogous depiction of vertical profiles for a steady west wind of 20 m/sec over a canal of constant depth (cf. Example 6). $A_V$ = const in this case as well. The chronological evolution of the vertical profile at an interior point from the onset of the wind until the steady state is reached can be seen from the diagram. The top curves are for boundary condition (22.3) and the lower ones for boundary condition (22.2).

It is evident that the water is carried along by the wind only in a relatively thin surface layer. Moving down from the surface, there is an immediate sharp drop in velocity, followed eventually by a reversal in the direction of the flow. Depending on the boundary condition prescribed at the bottom, the maximum of the deep current is intermediate (upper picture) or right at the bottom (lower picture). The shapes of the steady-state profiles are such that integrating velocity over depth at any point in the canal yields the value zero, i.e. transport through any section of the canal vanishes in the steady state.

In the upper diagram, a comparison is made with an analytic solution given by Hansen [19] for the case of a steady-state flow:

$$u(z') = \frac{g}{A_V}\frac{\partial\zeta}{\partial x}\left(\frac{z'^2}{2} - \frac{hz'}{3}\right) \quad ;$$

z' is measured positive up from the bottom (z' = h - z). The agreement between the numerical and the analytical values is quite good throughout. In particular, the statement made by Hansen that the maximum of the deep current occurs at z' = h/3 and that the inversion in the direction of the flow occurs at z' = 2h/3 is supported by the numerical results. Only near the surface do the values differ slightly (cf. column 2 and 3 in Table 2). These differences can be explained by the relatively coarse grid, resulting in a correspondingly rough approximation to the slope of the surface $\partial\zeta/\partial x$ and the shear stress term (17.1). If (17.1) is not approximated -- as it was in (22.1) -- by forward differences, but instead by central ones, i.e. in the form /91

$$A_V \frac{\overset{(t)}{u}(m,0) - \overset{(t)}{u}(m,2)}{2\Delta z} = \lambda \left|\overset{(t)}{U}(m)\right| \overset{(t)}{U}(m) \quad \text{für alle } m$$

the numerical solution agrees better with the analytic ones (cf. Table 2, column 4).

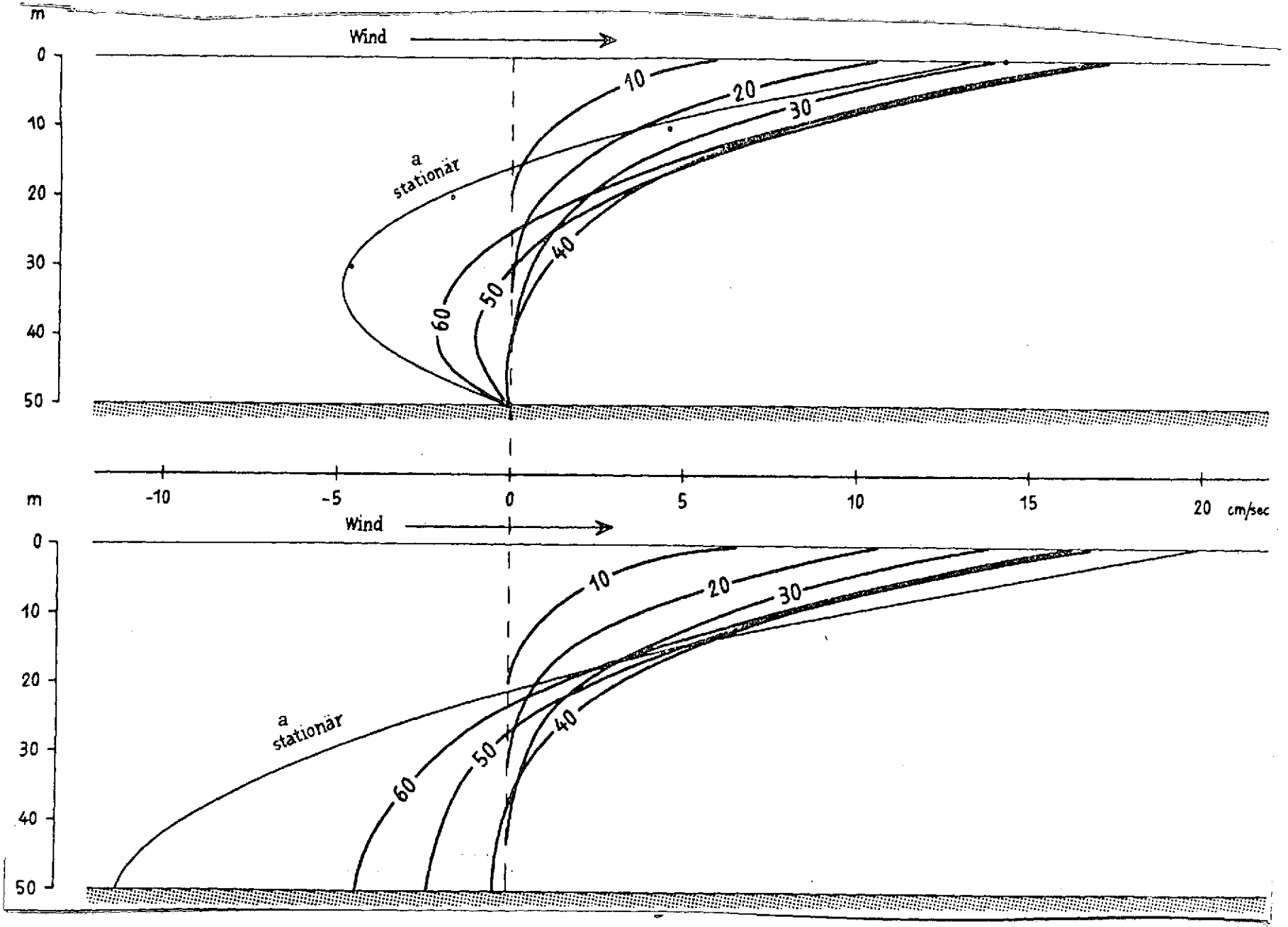


Fig. 38. [Caption on following page]

Fig. 38. Wind over a canal of constant depth with different boundary conditions at the bottom. Vertical profiles of flow velocity in interior of model canal depicted in Fig. 29. Various states between onset of wind and steady state. The numbers by the curves mean minutes after onset of wind.
Top: boundary condition $u_B = 0$ (cf. (22.3)).
Bottom: boundary condition $\tau_B = r|u_B|u_B$ (cf. (22.2)).
In the upper diagram, points mark the values derived analytically by Hansen's method.

Key: a. Steady state

---

TABLE 2. VERTICAL FLOW PROFILE u(z). COMPARISON BETWEEN ANALYTIC SOLUTION AND TWO NUMERIC SOLUTIONS

| Depth z (m) | $u_{analyt.}$ (cm/sec) | $u^{(1)}_{numer.}$ (cm/sec) | $u^{(2)}_{numer.}$ (cm/sec) |
|---|---|---|---|
| 0 | 14.3 | 13.5 | 14.0 |
| 10 | 4.6 | 4.0 | 4.5 |
| 20 | -1.7 | -2.0 | -1.7 |
| 30 | -4.6 | -4.7 | -4.5 |
| 40 | -4.0 | -4.0 | -3.9 |

Analyses have already been presented in Section II.5 to show how the vertical profile in Figs. 37 and 38 might be made to conform better to natural situations. The following examples deal with a relevant series of numerical tests. /92

First, Fig. 39 depicts three vertical profiles measured by different authors, all applying to tidal flows. The profiles on the left were obtained by Sverdrup [18] on the North Siberian Shelf, at different hours during a tidal period. They show that the maximum velocities in the tidal flow can also occur under the surface.

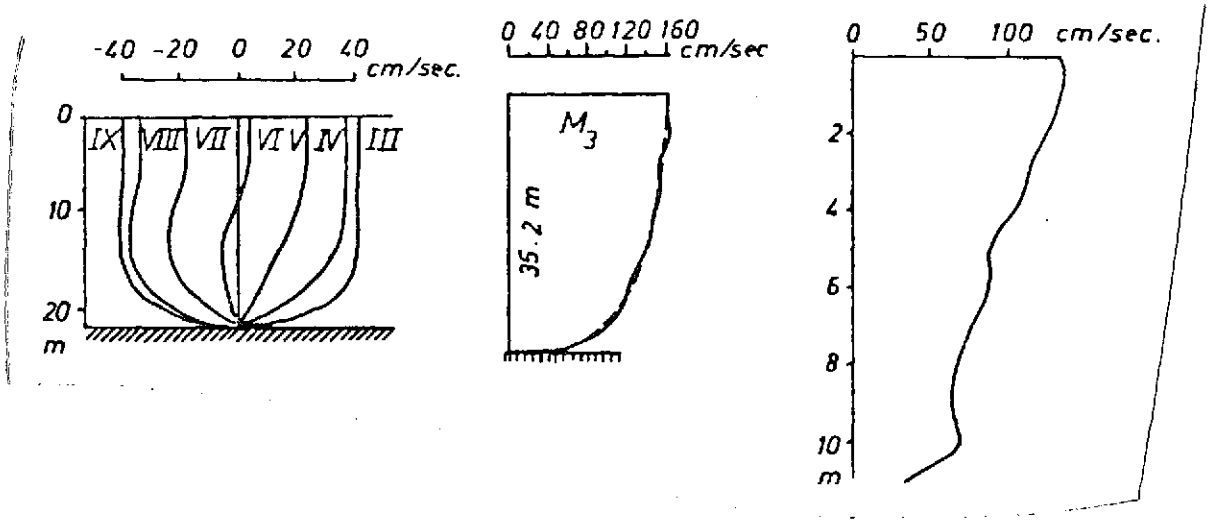


Fig. 39. Measured vertical profiles of tidal-flow velocity.
Left: according to Sverdrup [18]. The Roman numerals mean hours (after lunar transit at Greenwich).
Center: according to Van Veen [17]. The solid curve reproduces the measurement, and the dotted line is a profile obeying the power law.
Right: according to Siefert (provided personally). The curve was measured in the Bay of Germany.

The central curve was obtained by Van Veen [17] in measurements in the Straits of Dover and reflects the average situation during an interval of several hours in the vicinity of the greatest flood tide at a point near the French coast ($M_3$). The broken line drawn in along with it represents the curve /93

$$u(z) = \sqrt[5]{\frac{z + h}{h}}\, u_{0b}$$

which provides the best mean analytic approximation to the measured curve.

Lastly, the curve on the right was measured by Siefert (Neuwerk Research Group) in the mouth of the Elbe for the flood tide. It was kindly made available to the author.

A common feature of the different vertical profiles is that -- starting from the surface -- the velocity is virtually constant over a large distance, and begins to drop rapidly only in a zone near the bottom. In general, the curves can be approximated quite well by a parabolic profile.

On the other hand, the profiles calculated and presented so far (cf. Fig. 37) have very slight curvature. In defense, it must be pointed out that conditions in the ocean are very complex and that profiles of the form depicted in Fig. 37 have been observed in specific cases. For instance, Van Veen and Siefert also give some virtually linear profiles, and Curve V of Sverdrup likewise shows such a tendency. Nevertheless, the curves given in Fig. 39 can be considered typical, and the numerical model should be designed so that it is capable of reproducing this vertical behavior of the flow velocity profile.

That it is not enough to employ a vertical exchange term $A_V$ different from those employed in previous tide calculations but still independent of depth is demonstrated by Fig. 40.

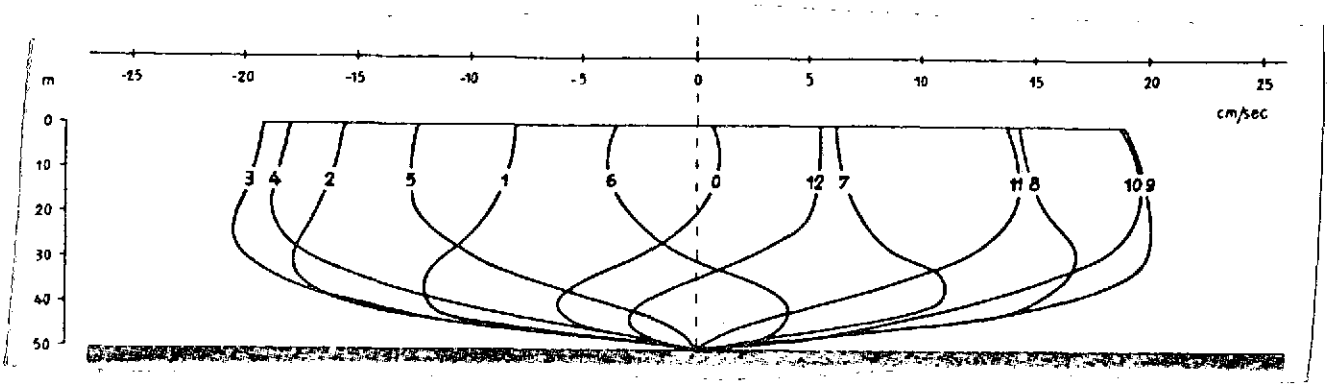


Fig. 40. $M_2$ tide in canal of constant depth for $A_V = 10^2$ cm$^2$/sec. Vertical profiles of flow velocity in interior of model canal depicted in Fig. 19 (point m = 7) for various tide phases. The numbers by the curves mean hours (after lunar transit at Greenwich).

Example 13:

Here the tidal study of Example 1 is repeated; however, in place of $A_V = 10^3$ cm$^2$/sec, the vertical exchange coefficient is now taken to be $A_V = 10^2$ cm$^2$/sec. As in Fig. 37, the resulting vertical profiles in Fig. 40 are depicted for point 7 of the canal. /94

It is evident that near the bottom, the profiles have not changed substantially relative to Fig. 37. However, the previous almost-linear drop of velocity from the surface downward is no longer present. The surface velocities are considerably smaller than in the previous case (Fig. 37); in general, the velocity increases with depth, reaches an intermediate maximum, and then

drops to zero. To this extent, a noteworthy approximation has been achieved with this HN model to the case observed by Sverdrup (Fig. 39). Hence, the low internal friction in the vertical direction results in more distinctive profiles; the smoothing effect brought about by the vertical exchange is naturally less pronounced well $A_V$ is smaller.

Example 14:

Substantial progress toward nature-like vertical profiles was achieved in a series of numerical tests in which the vertical exchange coefficient was made a function of depth. We return to /95
the schematic in Fig. 18, in which $A_V$ assumed a constant value $\bar{A}_V$ in a thin boundary layer at the bottom, and took on a likewise constant value $A_V^* > \bar{A}_V$ over the rest of the depth. By (54), this approach can be characterized numerically via a suitable choice of a dimensionless parameter $x$ proportional to the ratio of the vertical exchange coefficients above and within the boundary layer. Since relatively little has been revealed about this ratio by means of measurements, it should be legitimate to vary the parameter $x$ in a series of calculations and finally to consider representative that value which produces the most natural-looking flow profiles.

Relevant HN studies have been conducted for numerous values of $x$ in the tide model (Example 1) which has already been frequently employed. The results are summarized in Fig. 41 ($A_V^* = 10^3$ cm$^2$/sec). Once more, the vertical velocity profile at point 7 in the canal model is plotted for various exchange-coefficient expressions and models (cf. Fig. 37).

In addition to the boundary-layer graphs for $x$ = 210, 1.0, 0.5, and 0.3 (thin solid curves), two other curves were plotted for purposes of comparison: the profile computed in previous models for $A_V$ = const ($10^3$ cm$^2$/sec) (broken curve) and in a profile derived from the power law of Van Veen, which may serve as a standard of comparison for verisimilitude (thick solid curve).

Just how far away from natural conditions a model with constant vertical exchange coefficient really is can be seen clearly in the diagram. The curves also show that this discrepancy is immediately reduced by introducing a schematic boundary layer at the bottom with an exchange coefficient different from the rest of the depth interval. Through this series of numerical tests, it has been found that the agreement between the power-law profiles and the HN results is best for $x$ = 0.3. In fact, Fig. 41 shows that the two curves differ only slightly in this case.

The numerical simulation of this boundary layer presents no significant difficulties in programming or with respect to the stability of the method.

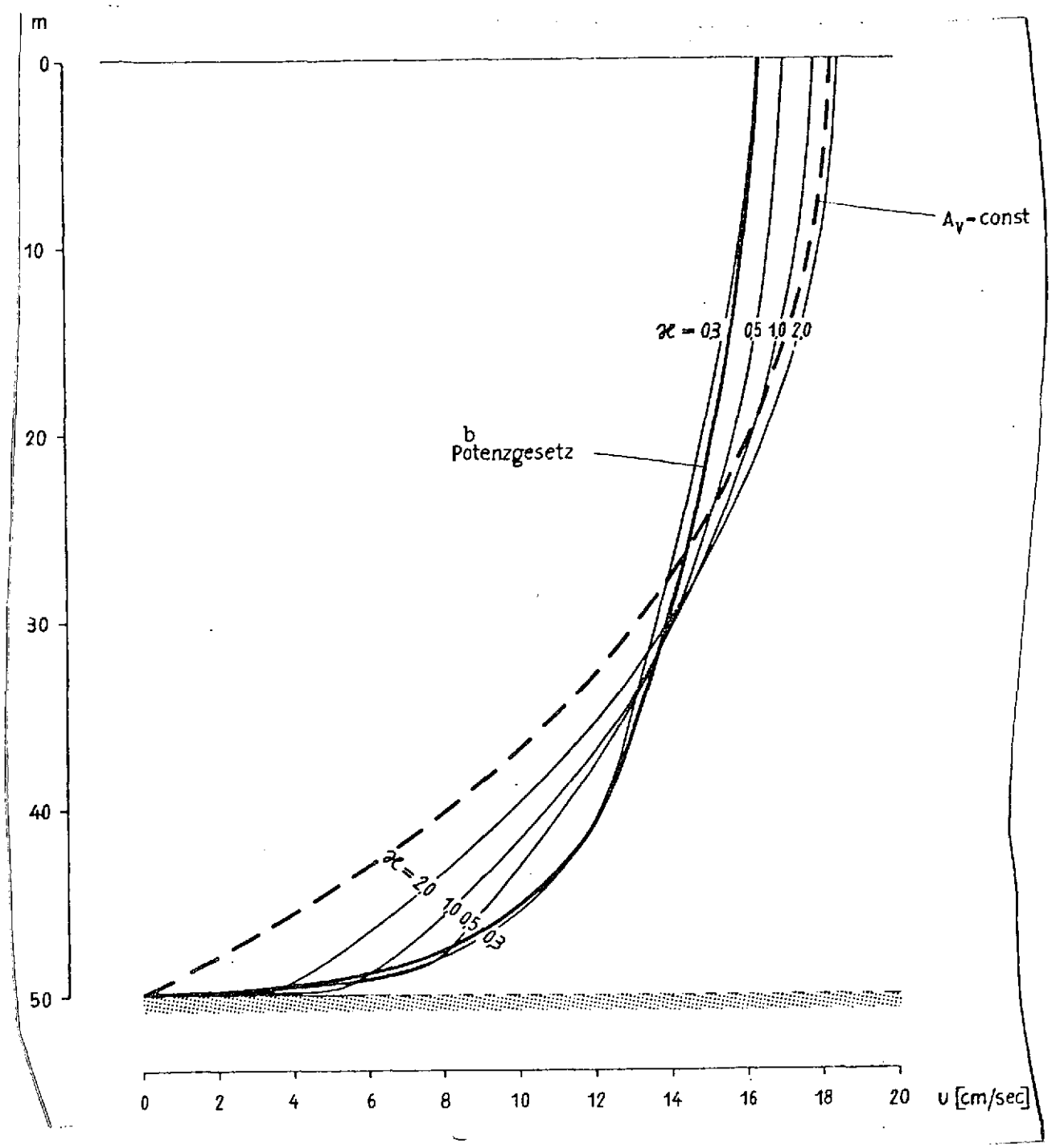


Fig. 41. $M_2$ tide in canal of constant depth. Vertical profiles of flow velocity in interior of model canal depicted in Fig. 19 (point m = 7) with different expressions for the vertical exchange coefficient $A_V(z)$.

[a] Scharparameter ist $\varkappa = \frac{\bar{A}_V \Delta_{K-1} z}{A_V^* d}$

[continued on following page]

Fig. 41 (continued)

$$A_V(z) = A_V^* = \text{const}$$

$$A_V(z) = \begin{cases} A_V^*, & \text{if} \quad 0 \geqq z \geqq -h+d \\ \bar{A}_V, & \text{if} \quad -h+d \geqq z \geqq -h \end{cases}$$

Empirical power law

$$u(z) = \sqrt[5]{\frac{z+h}{h}}\, u_{ch}$$

Key: a. Family parameter
b. Power law

---

## IV. Concluding Remark /97

These investigations have contributed to the three-dimensional treatment of hydrodynamic problems with the aid of HN methods. The HN models designed here can be used to derive statements on the vertical structure of motions as well as to calculate horizontal flows. This offers a chance of attacking physical processes in water which depend heavily on the vertical distribution of flow velocities, such as solid transport, with HN methods.

The examples cited here are restricted to wind-induced and tide-induced motions in schematic canals and basins, mostly of constant depth and with a constant vertical exchange coefficient; to this extent, they have little to do with conditions in natural seas. On the other hand, numerical questions associated with the three-dimensional extension of the HN method can be particularly clearly recognized and resolved in these simple models.

Moreover, two important steps have already been taken with regard to making the models conform better to natural conditions: the introduction of arbitrary depth profiles, and the incorporation of a boundary layer near the bottom.

Of course, many questions are yet to be resolved, and the models established here must be perfected and extended in various directions. This will be the object of more comprehensive analyses. One of the main projects will be to develop three-dimensional HN models for natural marine areas or rivers, in order to be able to study, for example, tidal processes in the North Sea or in the tidal estuaries of the Bay of Germany as functions of both horizontal and vertical distance. The results presented here for many examples, which usually agree well with available

information or existing theories, justify the hope that such studies will be possible in the near future.

## REFERENCES


1. Sündermann, J., "A comparison between analytic and numerical calculations of wind-induced flows and water levels in a model sea with applications to the North Sea," Mitt. Inst. Meereskd. Univ. Hmb. (4) (1966).

2. Courant, R. and Hilbert, D., Methoden der mathematischen Physik [Methods of Mathematical Physics], Vol. 2, Springer-Verlag, Berlin-Heidelberg, New York, 1968.

3. Brettschneider, G., "Application of a method developed at the Oceanographic Institute of the University of Hamburg for determining numerically the tides in peripheral seas to the $M_2$ co-oscillational tide in the North Sea," Mitt. Inst. Meereskd. Univ. Hmb. (7) (1967).

4. Hansen, W., "Theory and applications of computation of water level and flows in peripheral seas," Tellus 8 (1956).

5. Hansen, W., "Hydrodynamic models applied to oceanographic problems," Mitt. Inst. Meereskd. Univ. Hmb. (1) (1962).

6. Röber, K., "Analytical and numerical solutions for co-oscillational tides in a rectangular basin of constant depth allowing for bottom friction, Coriolis force, and horizontal exchange," Mitt. Inst. Meereskd. Univ. Hmb. (16) (1970).

7. Fischer, G., "A numerical method for calculating wind pressure and tides in peripheral seas," Tellus 11 (1959).

8. Rose, D., "Quantitative determination of tides and tidal flows in shallow water areas by means of the difference method," Mitt. Franzius-Int. TH Hann. 18 (1960).

9. Ramming, H.G., "Tides and tidal flows in the Eider," Mitt. Inst. Meereskd. Univ. Hmb. (1) (1962).

10. Schmitz, H.P., "A difference equation system to determine unsteady motions in a sea with minor turbulence friction," DHZ 18 (1965).

11. Schäfer, P., Anwendung des HN-Verfahrens zur Ermittlung des Einflusses von Gitternetzverfeinerungen auf die Berechnung der $M_2$-Gezeit in der Nordsee [Applications of the HN Method to Determining the Influence of Grid Refinements on the Calculation of the $M_2$ Tide in the North Sea], Thesis, University of Hamburg, 1970.

12. Courant, R., Friedrichs, K.O. and Lewy, H., "Partial differential equations in mathematical physics," Math. Ann. 100 (1928).

13. Lax, P.D. and Richtmyer, R.D., "Survey on the stability of linear finite difference equations," Comm. Pure and Appl. Math. 9 (1956).

14. Munk, W.H., Miller, G.R., Snodgrass, F.E., and Barber, N.F., "Directional recording of swell from distant storms," Phil. Trans. Roy. Soc. 255, 1062 (1963).

15. "Reproduction of motions in the sea with the aid of hydrodynamic-numerical methods," Mitt. Inst. Meereskd. Univ. Hmb. (5) (1966).

16. Vollmers, H., and Sündermann, J., "Tidal waves in schematic estuaries," Proc. 12th Conf. Coast. Eng., Washington, 1971.

17. Van Veen, J., "Water movements in the Straits of Dover," Journ. du Cons. 13 (1938).

18. Sverdrup, H.U., "Dynamic of tides on the North Siberian Shelf," Geof. Publ. No. 4, 1927.

19. Hanse, W., "Drift current and wind pressure, DHZ 3 (1950).

20. Richtmyer, R.D., Difference Methods for Initial-Value Problems, Interscience Publishers, New York, 1957.

21. Forsythe, G.E. and Wasow, W.R., Finite-Difference Methods for Partial Differential Equations, Wiley & Sons, New York-London-Sydney, 1967.

22. Crank, J. and Nicolson, P., "A practical method for numerical evaluation of solutions of partial differential equations of the heat-conduction type," Proc. Cambr. Phil. Soc. 43 (1947).

23. Gröbner, W., Matrizenrechnung [Matrix Arithmetic], Hochschultaschenbücher 103/103a, Bibliograph. Inst., Mannheim, 1966.

24. Sverdrup, H.U., Johnson, M.W., and Fleming, R.H., The Oceans, Prentice Hall, Englewood Cliffs, 1942.

25. Kagan, B.A., Gidrodinamicheskiye modeli prilivnykh dvizheniy v more [Hydrodynamic Models of Tidal Motions in the Sea], "Gidrometeorologicheskoye izdatel'stvo," Leningrad 1968.

26. Bowden, K.F., "Measurements of turbulence near the sea bed in a tidal current," J. Geoph. Res. 67 (1962).

27. Trepka, L. von, "Application of the hydrodynamic-numerical method to determining the influence of the shelf on tides in model canals and model oceans," Mitt. Inst. Meereskd. Univ. Hmb. (9) (1967).

28. Ekman, V.W., "On the influence of the earth's rotation on ocean currents," Ark. Mat., Astr. och Fys. 2 (1905).